BLOCK SEQUENCE DIRECTED MATERIALS: FUNCTIONAL AND ORDERED NANOCOMPOSITES DERIVED FROM BLOCK COPOLYMER COASSEMBLY

by Morgan Mertens Stefik

This thesis/dissertation document has been electronically approved by the following individuals:

Wiesner,Ulrich B. (Chairperson)

Ober,Christopher Kemper (Minor Member)

Disalvo,Francis J (Minor Member)

BLOCK SEQUENCE DIRECTED MATERIALS:

FUNCTIONAL AND ORDERED NANOCOMPOSITES

DERIVED FROM BLOCK COPOLYMER COASSEMBLY

A Dissertation

Presented to the Faculty of the Graduate School

of Cornell University

in Partial Fulfillment of the Requirements for the Degree of

Doctor of Philosophy

by

Morgan Mertens Stefik

August 2010

BLOCK SEQUENCE DIRECTED MATERIALS: FUNCTIONAL AND ORDERED NANOCOMPOSITES DERIVED FROM BLOCK COPOLYMER COASSEMBLY

Morgan Mertens Stefik, Ph.D.

Cornell University 2010

Nanocomposite materials with ordered structures are critical for the advancement of numerous fields ranging from microelectronics to energy conversion and storage. However, there are few techniques for controlling the necessary nanoscale morphologies and compositions which are compatible with affordable, large-scale manufacturing. The coassembly of block copolymers with inorganic materials provides such a route to achieve controlled nanomaterials, but such examples have generally resulted in mesoporous single-component materials. In this thesis it is shown that the general challenge to achieve multifunctional nanocomposites directly from block copolymer coassembly may be surmounted by designing novel block copolymers where each block has the design intent to result in a functional component of the resulting nanocomposites. Such a method would enable block sequence directed materials (BSDM), where a sequence of three or more chemically unique polymer blocks direct the spatial arrangement and interface definitions of multiple functional materials.

Towards this end, four examples are provided. First, a diblock copolymer poly(ethylene oxide-b-acrylonitrile) is demonstrated to enable direct synthesis of nanocomposites composed of crystalline titania and partially-graphitic carbon.

Second, this method is expanded by adding a third chemically unique block to form PAN-*b*-PEO-*b*-PPO-*b*-PEO-*b*-PAN where now the use of three chemically distinct polymer blocks enabled control over each of the three final components: partially-graphitic carbon, crystalline transition metal oxide, and porosity. Although these nanocomposites only possessed short-range order, tuning of the individual block lengths and block fractions resulted in control over the three components.

Third, it is shown that highly-ordered, multi-ply nanocomposites can result from the coassembly of poly(isoprene-*b*-styrene-*b*-ethylene oxide) (ISO) triblock terpolymers. Tuning the ratio of nanoparticles to ISO enabled access to four unique morphologies and the selection of quasi-1D, 2D, or 3D pathways. Fourth, it is shown that an ordered 3D network morphology which is chiral (non-centrosymmetric) can result from the coassembly of an ISO with a particular composition. Such non-centrosymmetric nanostructures are necessary to enable macroscopic polarization for piezoelectric, pyroelectric, and second-order nonlinear optical properties in amorphous materials. Thus through these four examples, it is demonstrated that the tuning of the polymer-oxide coassembled systems enables control over both nanocomposite composition and morphology.

BIOGRAPHICAL SKETCH

Morgan Mertens Stefik was the second child of his parents, Ellen and Mark. His older sister Paige always watched out for him and set high standards for him to aspire. As a boy, he spent much of his time climbing redwood trees, building zip-lines, and disassembling electronics. His parents went to great lengths to always live in districts which had good schools. As a young adult, Morgan attended Henry M. Gunn High School in Palo Alto, CA where he learned much under the supervision of skilled teachers. Beyond the chemistry, physics, and calculus courses, he became particularly engaged in the autoshop where he learned to apply scientific concepts towards the understanding and modification of automobiles. Beyond fostering Morgan's thirst for knowledge, autoshop also enabled him to pursue a common interest to many teenage boys: automobile racing. Morgan was coached by the autoshop teacher—a local racing legend—Mr. Camicia, and placed fourth in the 2001 Duel at De Anza. Autoshop may have been his favorite class, but he still studied for all of his classes, earning good marks and invitations to attend several universities.

Morgan's developing interest in engineering was further pursued by entering the bachelors degree program in the Materials Engineering Department (MATE) at California Polytechnical State University (Cal Poly) in San Luis Obispo, CA. Cal Poly was a perfect fit for Morgan as it could satisfy his education interests (at the time US News ranked it the #1 Primarily Undergraduate Engineering Uni-verisity) and outdoor interests with hiking trails on campus, mountain biking and rock climbing five minutes away, and an ocean twelve minutes away. In his second year, he met his wife to be, Julia, on a rock climbing trip to Santa Barbara. She showed him that you don't need fancy climbing shoes to scale cliffs and always

encouraged their seeking of adventures whenever possible. The rigorous course work prepared Morgan to start an engineering career, but there were several particular faculty which significantly influenced his path. The MATE department had a focus on sustainability, largely due to the inspiration of Prof. Linda Vanasupa. She informed all of the MATE students of their duty to society through the creed of the National Society of Professional Engineers and educated them as to the prevailing sustainability issues. This knowledge coupled with a presentation on sustainable energy by Prof. Nate Lewis inspired Morgan to contribute towards solving the energy challenge. Prof. Katherine C. Chen mentored Morgan through several research projects and initiated his interest in pursuing a doctorate degree. After graduating summa cum laude in 2005 he felt ready to move on to a graduate school.

Morgan matriculated into the doctorate program in Materials Science and Engineering at Cornell University in Ithaca, NY in 2005. Although the regional wine and weather were in great *contrast* with that of his opportunity in Santa Barbara, he had many common research interests with a few particular Cornell faculty. He accepted a research project to develop new materials for fuel cells under the guidance of Professor Ulrich Wiesner and Professor Francis J. DiSalvo. After yet more course work and examinations, Morgan finally had the opportunity to fully commit his working time towards research. He quickly found out that research was a challenging task which often had more obstacles than answers; but with time and experience an experimental intuition emerged which made science fun. There were certainly some difficult times while adapting to this new occupation at Cornell, but Morgan's family always provided loving support. Overtime the scope of his project broadened as the Cornell Fuel Cell Institute became part of the new

Energy Materials Center at Cornell in 2009. The approachable and intellectually dedicated Cornell community fostered many productive collaborations and created many friendships and fond memories for Morgan. The work presented in this thesis outlines many of his contributions to the scientific fields he has studied while at Cornell.

Dedicated to the ∼6,700,000,000 of us. May scientific advancements enable

sustainable lifestyles with clean energy, plentiful food, and good health for all.

ACKNOWLEDGEMENTS

TABLE OF CONTENTS

LIST OF TABLES

CHAPTER 1

INTRODUCTION

Ordered nanocomposite materials are crucial for numerous applications ranging the gamut from electronics to energy conversion. In particular, many of the energy conversion and storage devices under development—including photovoltaics, batteries, fuel cells, and supercapacitors—are electrochemical devices which rely upon reactions occuring at interfaces with the transportation of reactants and products occuring along pathways. The performance of such energy devices could be greatly enhanced by structuring the active components with control over the composition, interfaces, and pathways. In particular, this structural control should occur at the nanoscale to faciliate high interfacial areas for high power density as well as short transport distances to limit transport restrictions. Of the potential synthetic routes to make controlled nanoarchitectures, bottom-up procedures are the most promissing due to their simplicity, scalability, and low cost.

Block copolymers are a class of macromolecules which have been extensively applied towards the bottom-up synthesis of a diverse range of precisely controlled nanomaterials with controlled morphologies.[1] However, the resulting materials generally are purely organic and have very limited physical and chemical properties which prevents their direct use in many applications such as energy conversion and storage devices or as photonic metamaterials.[2,3] The combination of inorganic materials which have robust functionality with block copolymers which form ordered nanoscale morphologies has been extensively studied in the past decade. Generally amphiphilic block copolymers are utilized such that a selective interaction may drive inorganic nanoparticles or molecular prescursors to selectively swell the hydrophilic block of the polymer. In a typical procedure, the polymer and inorganic species are combined in a common solvent and then cast or coated onto

a substrate to allow evaporation to induce coassembly. During evaporation distinct, ordered domains form from the hydrophobic block phase-separating from a mixture of the hydrophilic block with an inorganic species; the balance of interface and chain stretching free energies lead the polymer to direct the coassembly into various ordered morphologies. Such routes have been extensively applied towards the synthesis of nanocomposites with ordered morphologies. While many different compositions have been explored—oxides,[4–6] metals,[7,8] and carbon[9–11] materials—published examples have generally been limited to single-component materials with mesopores.

Electrochemical devices often require several different components to provide the necessary functionality such as electron transport, ion transport, as well as reactant and product transport. In this thesis it was shown that the general challenge to achieve multifunctional nanocomposites directly from block copolymer coassembly may be surmounted by designing novel block copolymers where each block has the design intent to yield a functional component of the resulting nanocomposites. Please note that this approach is fundamentally different from combining an amphiphilic block copolymer with multiple hydrophilic precursors which was previously shown to result in a random dispersion of two materials with ordered pores.[12–14] Rather, the objective was to have the block sequence directly define the materials in the resulting nanocomposites. Such a method would enable block sequence directed materials (BSDM),[15] where a sequence of three or more chemically unique polymer blocks direct the spatial arrangement and interface definitions of multiple functional materials. The achievement of BSDMs would be a significant step towards mimicking the more complex assembly processes, e.g. protein coassembly, that result in biological nanocomposites. The nanocomposite design intent thus may be directly encoded into the molecular structure of the

block copolymer.

This thesis is organized into sections which each demonstrate significant steps towards the realization of BSDMs. It was shown that di-functional nanocomposites may be directly synthesized from the coassembly of an AB diblock copolymer in Section 2. Next, it was shown that this approach may be extended to enable the direct synthesis of tri-functional nanocomposites from the coassembly of ABCBA pentablock terpolymers in Section 3. While these two sections demonstrated compositional control of multifunctional nanocomposites, the short-range ordered worm-like morphologies did not facilitate much tunability of the morphology. It was then shown that different block terpolymers based on poly(isoprene-b-styrene-b-ethylene oxide) (ISO) enable the direct synthesis of highly-ordered, multi-ply nanocomposites in Section 4. Tuning the ratio of nanoparticles to ISO enabled access to four unique morphologies including core-shell hexagonal, core-shell double gyroid, three-domain lamellae, and core-shell inverse-hexagonal, all of which are centrosymmetric morphologies. In contrast, non-centrosymmetric morphologies are known to enable polarization properties which are key for certain applications. It was next shown such a non-centrosymmetric and networked morphology—the alternating gyroid G^A— may be obtained directly by coassembly with an ISO of a particular composition in Section 5. Through these examples it was demonstrated that careful tuning of coassembled oxide-block copolymer systems enables control over both the composition and morphology of nanocomposites. While the compositions and morphologies explored in these studies were particularly relevant to electrochemical energy conversion and storage devices, significant challenges still remain before functioning devices may be realized from BSDMs. These challenges and several potential synthetic routes to achieve BSDM devices were then discussed in Section 6.

REFERENCES

[1] F. S. Bates and G. H. Fredrickson. Block copolymers - designer soft materials. *Physics Today*, 52(2):32–38, 1999.

[2] J. Wen and G. L. Wilkes. Organic/inorganic hybrid network materials by the sol-gel approach. *Chemistry of Materials*, 8(8):1667–1681, 1996.

[3] P. Innocenzi and B. Lebeau. Organic-inorganic hybrid materials for non-linear optics. *Journal of Materials Chemistry*, 15(35-36):3821–3831, 2005.

[4] M. Templin, A. Franck, A. DuChesne, H. Leist, Y. M. Zhang, R. Ulrich, V. Schadler, and U. Wiesner. Organically modified aluminosilicate mesostructures from block copolymer phases. *Science*, 278(5344):1795–1798, 1997.

[5] D. Y. Zhao, J. L. Feng, Q. S. Huo, N. Melosh, G. H. Fredrickson, B. F. Chmelka, and G. D. Stucky. Triblock copolymer syntheses of mesoporous silica with periodic 50 to 300 angstrom pores. *Science*, 279(5350):548–552, 1998.

[6] P. D. Yang, D. Y. Zhao, D. I. Margolese, B. F. Chmelka, and G. D. Stucky. Generalized syntheses of large-pore mesoporous metal oxides with semicrystalline frameworks. *Nature*, 396(6707):152–155, 1998.

[7] S. C. Warren, L. C. Messina, L. S. Slaughter, M. Kamperman, Q. Zhou, S. M. Gruner, F. J. DiSalvo, and U. Wiesner. Ordered mesoporous materials from metal nanoparticle-block copolymer self-assembly. *Science*, 320(5884):1748–1752, 2008.

[8] Z. H. Li, H. Sai, S. C. Warren, M. Kamperman, H. Arora, S. M. Gruner, and U. Wiesner. Metal nanoparticle-block copolymer composite assembly and disassembly. *Chemistry of Materials*, 21(23):5578–5584, 2009.

[9] R. Ryoo, S. H. Joo, and S. Jun. Synthesis of highly ordered carbon molecular sieves via template-mediated structural transformation. *Journal of Physical Chemistry B*, 103(37):7743–7746, 1999.

[10] J. Lee, S. Yoon, T. Hyeon, S. M. Oh, and K. B. Kim. Synthesis of a new mesoporous carbon and its application to electrochemical double-layer capacitors. *Chemical Communications*, (21):2177–2178, 1999.

[11] C. D. Liang, K. L. Hong, G. A. Guiochon, J. W. Mays, and S. Dai. Synthesis of a large-scale highly ordered porous carbon film by self-assembly of block copolymers. *Angewandte Chemie-International Edition*, 43(43):5785–5789, 2004.

[12] J. Fan, S. W. Boettcher, and G. D. Stucky. Nanoparticle assembly of ordered multicomponent mesostructured metal oxides via a versatile sol-gel process. *Chemistry of Materials*, 18(26):6391–6396, 2006.

[13] R. L. Liu, Y. F. Shi, Y. Wan, Y. Meng, F. Q. Zhang, D. Gu, Z. X. Chen, B. Tu, and D. Y. Zhao. Triconstituent co-assembly to ordered mesostructured polymer-silica and carbon-silica nanocomposites and large-pore mesoporous carbons with high surface areas. *Journal of the American Chemical Society*, 128(35):11652–11662, 2006.

[14] R. Liu, Y. Ren, Y. Shi, F. Zhang, L. Zhang, B. Tu, and D. Zhao. Controlled synthesis of ordered mesoporous c-tio2 nanocomposites with crystalline titania frameworks from organic-inorganic-amphiphilic coassembly. *Chemistry of Materials*, 20(3):1140–1146, 2008.

[15] M. Stefik, H. Sai, K. Sauer, S. M. Gruner, F. J. DiSalvo, and U. Wiesner. Three-component porous-carbon-titania nanocomposites through self-assembly of abcba block terpolymers with titania sols. *Macromolecules*, 42(17):6682–6687, 2009.

CARBON-CRYSTALLINE TITANIA NANOCOMPOSITES FROM MICROPHASE SEPARATION OF POLY(ETHYLENE OXIDE-*b*-ACRYLONITRILE) WITH TITANIA SOLS[*]

2.1 Introduction

Recent literature contains multiple examples of efficient electrode materials composed of an electrochemically active metal or metal oxide dispersed on a carbon matrix.[1–5] The invention of silica-templated ordered mesoporous carbon triggered new electrode materials for Li-ion battery, supercapacitor, and fuel cell applications.[6–9] For example, mesostructured carbon-electrochemically active metal oxide (or metal) composites were fabricated by infiltration of metal precursors into an ordered mesoporous carbon.[10–12] Materials based on these silica-templated carbons require tedious techniques and the extension of known infiltration procedures to new materials is often challenging. Furthermore, in most cases the ordered mesoporous carbon was made from sources for amorphous carbon.[8] This is also true for our recently published CASH method which leads to amorphous carbon-highly crystalline transition metal oxide composites.[13] In contrast, the efficient electron transfer, high electrical conductivity, and thermodynamic stability necessary in electrode applications favours the use of graphitic carbon. Poly(acrylonitrile) is an established graphitic carbon source which is commonly used for the commercial production of graphite carbon nanofibers.[14] Despite much interest in block copolymer derived mesoporous carbons, to the best of our knowledge there is no report on the synthesis of nanostructured carbon-electrochemically active transition metal
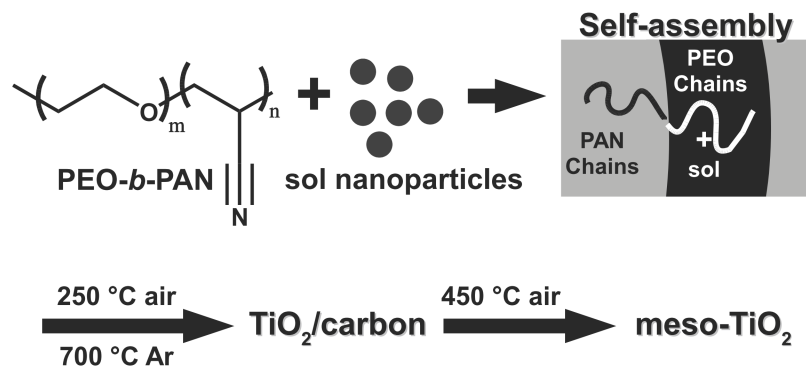
Figure 2.1: Schematic representation of "one-pot" synthesis of mesostructured crystalline TiO$_2$-carbon composites and mesoporous titania via self-assembly of PEO-b-PAN with TiO$_2$ sols followed by specific heat treatments.

oxide composites from poly(acrylonitrile) based block copolymers.[3, 15–22]

Here we show that a carbon-transition metal oxide nanocomposite can be synthesized from microphase separating diblock copolymer poly(ethylene oxide-b-acrylonitrile) (PEO-b-PAN) and a transition metal oxide sol. More specifically, nanostructured carbon-crystalline (anatase) TiO$_2$ was fabricated (Figure 2.1) using a non-hydrolytic sol-gel route.[23] The "one-pot" synthetic method presented herein is much simpler than the backfilling methods based on preformed mesoporous carbons.[10–12] PEO-b-PAN was synthesized by anionic polymerization of PEO and subsequent atomic transfer radical polymerization (ATRP) of PAN. The final polymer was characterized by gel permeation chromatography (GPC) for its polydispersity and by nuclear magnetic resonance spectroscopy (NMR) to determine its molecular weight (Figure 2.2). The NMR results show that the PEO macroinitiator (6,400 g/mol) was chain extended with 2,500 g/mol of PAN. The GPC elugram was monomodal with a moderate shoulder and had a polydispersity of 1.15. The shoulder was likely due to the termination of living PAN chain ends by Cu^I species and acidic protons of DMF as previously reported.[24] The
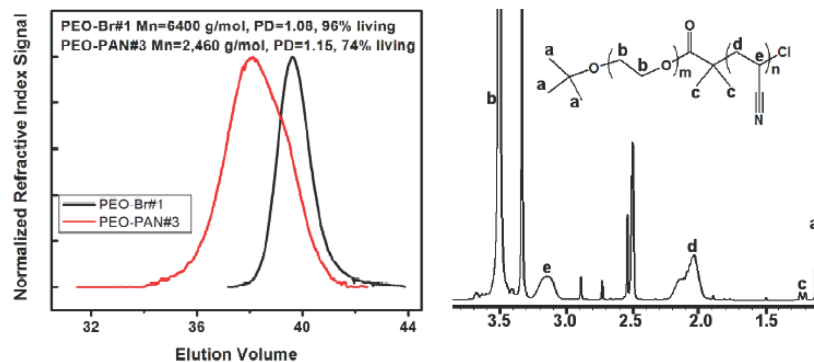
Figure 2.2: The gel permeation chromatography traces indicate controlled growth of PEO-*b*-PAN from the PEO macroinitiator (left). ¹H NMR spectra of PEO-*b*-PAN (right) were used to determine the block fractions.

low acrylonitrile conversion of 4.5% was also attributed to this side reaction. The PEO-*b*-PAN-TiO$_2$ hybrid materials were produced by selectively swelling the hydrophilic PEO block of the PEO-*b*-PAN block copolymer with the metal-oxide sol. In this procedure, the block copolymer was first dissolved in dimethylformamide (DMF). The sol was prepared in the polymer solution by reacting a metal chloride with the corresponding metal alkoxide to form the metal oxide sol and the accompanying alkyl halide. The sol-polymer solution was cast at 70 °C resulting in an amorphous hybrid material. The as-made film was heated to 250 °C in air to stabilize the PAN by cyclization[5] and then heat-treated under argon in a tube furnace to 700 °C to obtain a highly crystalline composite. During this process, the metal oxide crystals nucleate, grow and sinter into wall material while the PEO is thermally removed and the stabilized PAN is converted to a carbon material. This results in a nanostructured carbon-crystalline titanium dioxide composite denoted TiO$_2$-carbon.

2.2 Experimental Methods

2.2.1 Materials

Acrylonitrile (AN) (99% Aldrich) was stirred over calcium hydride for at least one hour before distillation under reduced pressure. CuCl (99.995% Aldrich), 2,2'-bipyridyl (BPY) (99% Aldrich), and HPLC grade N,N-dimethylformamide (DMF) (99.9% Aldrich) were used as recieved.

2.2.2 Synthesis of PEO-*b*-PAN

PEO Growth and Functionalization

PEO was grown and functionalized for ATRP chain extension with 2-bromoisobutyryl bromide as described elsewhere,[25] however potassium tert-butoxide was used as the initiator.

ATRP PAN Chain Extension

Polyacrylonitrile was grown from the bromine functionalized PEO. In a typical polymerization of AN, 1 g (1.56E-4 mol, 6,400 g/mol) PEO-Br and a stir bar were placed into a Schlenk flask equipped with a septum, a high vacuum valve, and a hose connector. The macroinitiator was then dissolved in 19.5 mL DMF and 10.27 mL (156 mmol) AN. The resulting solution was then subject to four freeze-pump-thaw cycles before being backfilled with nitrogen. In a separate Schlenk flask, a stock solution was prepared of 30 mg (0.3 mmol) CuCl, 142 mg (0.91 mmol) BPY, and 10 mL of degassed DMF was prepared in a nitrogen glove box. The stock solution was allowed to stir for at least 10 minutes before transferring a quantity containing 3.1 mg (0.031 mmol) CuCl and 14.5 mg (0.0937 mmol) BPY to the reaction flask using a degassed syringe. The reaction flask was then placed in an

oil bath at 55 °C for 27 hours. The polymerization was terminated by exposing the reaction contents to air. The copper catalyst was removed by diluting the reaction crude with DMF and passing the solution through basic alumina. The polymer was isolated by removing the DMF under high vacuum overnight. The resulting block copolymer had 6,400 g/mol PEO, 2,500 g/mol PAN, and had a polydispersity of 1.15.

2.2.3   Synthesis of TiO$_2$-carbon

After 0.1 g of PEO-b-PAN was dissolved in 2 ml N,N-dimethylformamide (DMF), 0.36 ml of titanium tetraisopropoxide (TTIP) and 0.14 ml titanium chloride (IV) were added into the solution. After stirring for 12 hours at room temperature, films were cast by evaporation of the solvent and byproducts in air on a hot plate at 70 °C and then at 130 °C in a vacuum oven for one hour. The as-made amorphous TiO$_2$-PEO-b-PAN material was heat treated at 1 °C/min to 250 °C in air to stabilize the PAN for subsequent carbonation. The stabilized film was then heated to 700 °C using 1 °C/min ramp under argon and held for 2 hours resulting in crystallization of the amorphous metal oxide walls and conversion of the crosslinked PAN to partially graphitic carbon.

2.3   Results and Discussion

The microphase separated structure of as-made TiO$_2$-PEO-b-PAN was characterized by transmission electron microscopy (TEM), thermal gravimetric analysis (TGA), powder x-ray diffraction (XRD), and Raman spectroscopy. The TEM image in Figure 2.3 a suggests that the hydrophilic titanium dioxide-PEO domains (dark) microphase separate from the hydrophobic PAN domains (bright). As evident from the TEM micrograph, the resulting structures had short range order
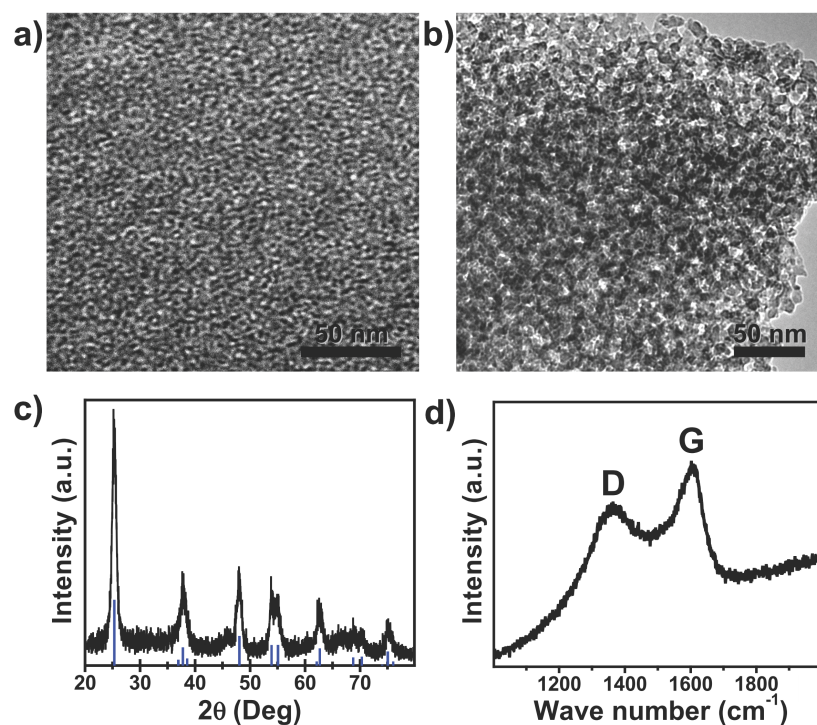
Figure 2.3: TEM images of as-made TiO_2-PEO-*b*-PAN (a) and calcined crystalline TiO_2-carbon composites (b) exhibited nanoscale features. The powder XRD pattern of TiO_2-carbon composites (c) was characteristic of anatase titania (markers indicate expected peaks for PDF #89-4921). The TiO_2-carbon Raman spectrum (d) had the characteristic D and G bands of partially graphitic carbon.
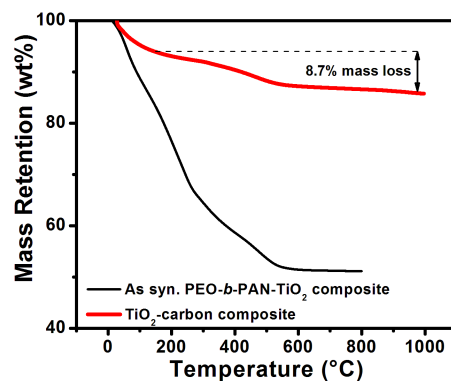
Figure 2.4: TGA data of as-made TiO_2-PEO-*b*-PAN (black) and TiO_2-carbon (bold red) in air exhibited characteristic mass losses from the cyclization process and carbon removal, respectively.

attributed to the high glass transition temperature ($\sim$85 °C) and high melting point of the semicrystalline PAN block ($\sim$326 °C). Thermogravimetric analysis (Figure 2.4) of the as-made composites under air showed two major decomposition steps. The first step below 250 °C corresponds to the cyclization of PAN while the second step above 250 °C corresponds to the decomposition of PEO and carbonization of PAN. Heat-treatment at 700 °C under inert atmosphere converted the amorphous TiO_2 to crystalline TiO_2 and the PAN to the final carbon material (Figure 2.3 b). The resulting wormhole-like porous structure as evidenced by TEM was reminiscent of the disordered crystalline alumina reported by the Pinnavaia group.[26, 27] A representative XRD spectrum, Figure 2.3 c, of a heat-treated sample reveals several well-resolved, sharp peaks on a flat baseline that were consistent with crystalline anatase (PDF #89-4921). The average crystallite size of 12 nm was calculated from the (101) XRD peak width using the Debye-Scherer equation. The similarity between this size and the structural feature sizes in the TEM of the heat treated composite (see Figure 2.3 b) suggests that the TiO_2 particles observed in TEM were primarily single crystalline. The TiO_2-carbon exhibited characteristics of partially graphitic carbon as evidenced by the presence of D and pronounced G bands in Raman spectroscopy (Figure 2.3 d). A subsequent TGA run on the heat treated TiO_2-carbon composite in air showed a significant weight loss of 8.7 % starting around 400 °C ascribed to the carbon oxidation to CO or CO_2.

Further evidence of carbon-titania phase separation was provided by nitrogen physisorption measurements. To this end the carbon was removed from TiO_2-carbon composites via heat-treatment under air at 450 °C, resulting in samples denoted as meso-TiO_2. The behaviour of meso-TiO_2 was then compared to that of the parent TiO_2-carbon. The nitrogen adsorption-desorption isotherm (Figure 2.5)
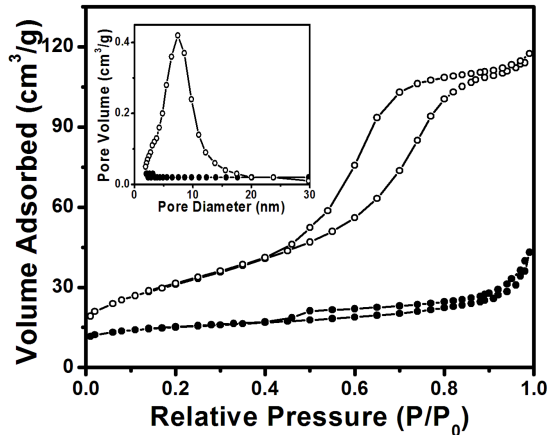
Figure 2.5: Nitrogen adsorption-desorption isotherms are shown for TiO$_2$-carbon (solid circles) and meso-TiO$_2$ (open circles) as well as the corresponding BJH pore size distributions (inset) of TiO$_2$-carbon composite (solid circles) and meso-TiO$_2$ (open circles).

and Barret-Joyner-Halenda (BJH) pore size estimate for TiO$_2$-carbon showed no significant mesoporosity (Figure 2.5 inset). In contrast, the same measurement on meso-TiO$_2$ exhibited a well-defined step at approximately 0.40-0.80 P/P_0, which was associated with the filling of mesopores due to capillary condensation. BJH pore size distribution analysis (Figure 2.5 inset) was used to determine the presence of relatively uniform 7.4 nm sized mesopores. The surface area increased from 52 m^2/g for TiO$_2$-carbon to 111 m^2/g for meso-TiO$_2$. These results suggest that the space occupied by carbon in TiO$_2$-carbon samples was converted to 7 nm sized mesopores in meso-TiO$_2$. XRD measurements on meso-TiO$_2$ show that the anatase crystal structure was preserved (Figure 2.6). These observations were consistent with the assumption that PAN as well as the resulting carbon phase are microphase separated from the rest of the composite.
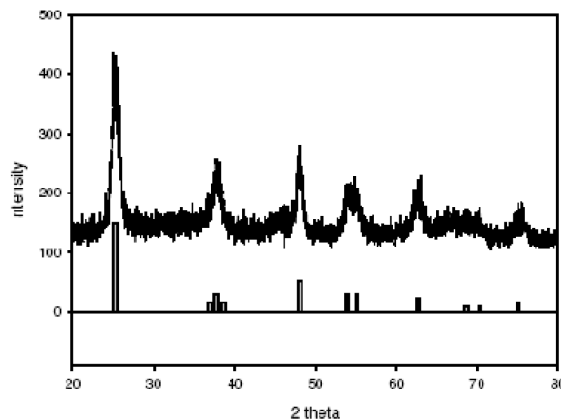
Figure 2.6: The powder XRD pattern of meso-TiO$_2$ was consistent with anatase titania (markers indicate expected peaks for PDF #89-4921).

2.4 Conclusions

In conclusion, carbon-crystalline titanium dioxide composites were fabricated through a simple "one-pot" method employing a graphitic carbon source (PAN) containing PEO-*b*-PAN diblock copolymer as a structure directing agent for titania precursors. Using this process, we were able to produce highly crystalline mesoporous titanium dioxide after removal of the carbon. This simple process may be extended to the preparation of other transition metal oxide-carbon systems and other highly crystalline mesoporous transition metal oxides.

2.5 Acknowledgements

REFERENCES

[1] V. Georgakilas, V. Tzitzios, D. Gournis, and D. Petridis. Attachment of magnetic nanoparticles on carbon nanotubes and their soluble derivatives. *Chemestry of Materials*, 17(7):1613–1617, 2005.

[2] L. Mohana and S. Ramaprabhu. Nanocrystalline metal oxides dispersed multiwalled carbon nanotubes as supercapacitor electrodes. *Journal of Physical Chemistry C*, 111(21):7727–7734, 2007.

[3] J. Li, S. Tang, L. Lu, and H. C. Zeng. Preparation of nanocomposites of metals, metal oxides, and carbon nanotubes via self-assembly. *Journal of the American Chemical Society*, 129(30):9401–9409, 2007.

[4] M. Egashira, H. Takatsuji, S. Okada, and J. Yamaki. Properties of containing Sn nanoparticles activated carbon fiber for a negative electrode in lithium batteries. *Journal of Power Sources*, 107(1):56–60, 2002.

[5] H. Li, Q. Wang, L.H. Shi, L.Q. Chen, and X.J. Huang. Nanosized SnSb alloy pinning on hard non-graphitic carbon spherules as anode materials for a Li ion battery. *Chemistry of Materials*, 14(1):103–108, 2002.

[6] J. Lee, J. Kim, and T. Hyeon. Recent progress in the synthesis of porous carbon materials. *Advanced Materials*, 18(16):2073–2094, 2006.

[7] R. Ryoo, S.H. Joo, and S. Jun. Synthesis of highly ordered carbon molecular sieves via template-mediated structural transformation. *Journal of Physical Chemistry B*, 103(37):7743–7746, SEP 16 1999.

[8] J. Lee, S. Yoon, T. Hyeon, S.M. Oh, and K.B. Kim. Synthesis of a new mesoporous carbon and its application to electrochemical double-layer capacitors. *Chemical Communications*, pages 2177–2178, 1999.

[9] J. Lee, S. Han, and T. Hyeon. Synthesis of new nanoporous carbon materials using nanostructured silica materials as templates. *Journal of Materials Chemistry*, 14(4):478–486, 2004.

[10] J. Fan, T. Wang, C.Z. Yu, B. Tu, Z.Y. Jiang, and D.Y. Zhao. Ordered, nanostructured tin-based oxides/carbon composite as the negative-electrode material for lithium-ion batteries. *Advanced Materials*, 16(16):1432+, 2004.

[11] S.M. Zhu, H.A. Zhou, M. Hibino, I. Honma, and M. Ichihara. Synthesis of MnO2 nanoparticles confined in ordered mesoporous carbon using a sonochemical method. *Advanced Functional Materials*, 15(3):381–386, 2005.

[12] I. Grigoriants, L. Sominski, H.L. Li, I. Ifargan, D. Aurbach, and A. Gedanken. The use of tin-decorated mesoporous carbon as an anode material for rechargeable lithium batteries. *Chemical Communications*, pages 921–923, 2005.

[13] J. Lee, M. C. Orilall, S. C. Warren, M. Kamperman, F. J. Disalvo, and U. Wiesner. Direct access to thermally stable and highly crystalline mesoporous transition-metal oxides with uniform pores. *Nature Materials*, 7(3):222–228, 2008.

[14] J.-B. Donnet and R. C. Bansal. *Carbon Fibers*. M. Dekker, New York, 2nd rev edition, 1990.

[15] T. Kowalewski, N.V. Tsarevsky, and K. Matyjaszewski. Nanostructured carbon arrays from block copolymers of polyacrylonitrile. *Journal of the American Chemical Society*, 124(36):10632–10633, 2002.

[16] C.B. Tang, K. Qi, K.L. Wooley, K. Matyjaszewski, and T. Kowalewski. Well-defined carbon nanoparticles prepared from water-soluble shell cross-linked micelles that contain polyacrylonitrile cores. *Angewandte Chemie-International Edition*, 43(21):2783–2787, 2004.

[17] C. Tang, B. Dufour, T. Kowalewski, and K. Matyjaszewski. Synthesis and morphology of molecular brushes with polyacrylonitrile block copolymer side chains and their conversion into nanostructured carbons. *Macromolecules*, 40(17):6199–6205, 2007.

[18] C.B. Tang, A. Tracz, M. Kruk, R. Zhang, D.M. Smilgies, K. Matyjaszewski, and T. Kowalewski. Long-range ordered thin films of block copolymers prepared by zone-casting and their thermal conversion into ordered nanostructured carbon. *Journal of the American Chemical Society*, 127(19):6918–6919, 2005.

[19] M. Kruk, B. Dufour, E.B. Celer, T. Kowalewski, M. Jaroniec, and K. Matyjaszewski. Synthesis of mesoporous carbons using ordered and disordered mesoporous silica templates and polyacrylonitrile as carbon precursor. *Journal of Physical Chemistry B*, 109(19):9216–9225, 2005.

[20] M. Kruk, B. Dufour, E. B. Celer, T. Kowalewski, M. Jaroniec, and K. Matyjaszewski. Well-defined poly(ethylene oxide)-polyacrylonitrile diblock copolymers as templates for mesoporous silicas and precursors for mesoporous carbons. *Chemestry of Materials*, 18(6):1417–1424, 2006.

[21] J.M. Leiston-Belanger, J. Penelle, and T.P. Russell. Synthesis and microphase separation of poly (styrene-b-acrylonitrile) prepared by sequential anionic and ATRP techniques. *Macromolecules*, 39(5):1766–1770, 2006.

[22] M. Lazzari, D. Scalarone, C. E. Hoppe, C. Vazquez-Vazquez, and M. A. Lopez-Quintela. Tunable polyacrylonitrile-based micellar aggregates as a potential tool for the fabrication of carbon nanofibers. *Chemistry of Materials*, 19(24):5818–5820, 2007.

[23] P. Arnal, R. J. P. Corriu, D. L., P. H. Mutin, and A. Vioux. A Solution Chemistry Study of Nonhydrolytic Sol-Gel Routes to Titania. *Chemistry of Materials*, 9(3):694–698, 1997.

[24] K. Matyjaszewski, S.M. Jo, H.J. Paik, and D.A. Shipp. An investigation into the CuX/2,2 '-bipyridine (X = Br or Cl) mediated atom transfer radical polymerization of acrylonitrile. *Macromolecules*, 32(20):6431–6438, 1999.

[25] S. Mahajan, S. Renker, P. F. W. Simon, J. S. Gutmann, A. Jain, S. M. Gruner, L. J. Fetters, G. W. Coates, and U. Wiesner. Synthesis and characterization of amphiphilic poly(ethylene oxide)-¡i¿block¡/i¿-poly(hexyl methacrylate) copolymers. *Macromolecular Chemistry and Physics*, (8):1047–1055, 2003.

[26] Z.R. Zhang, R.W. Hicks, T.R. Pauly, and T.J. Pinnavaia. Mesostructured forms of gamma-Al2O3. *Journal of the American Chemical Society*, 124(8):1592–1593, 2002.

[27] Z.R. Zhang and T.J. Pinnavaia. Mesostructured gamma-Al2O3 with a lath-like framework morphology. *Journal of the American Chemical Society*, 124(41):12294–12301, 2002.

CHAPTER 3

THREE-COMPONENT POROUS-CARBON-TITANIA NANOCOMPOSITES THROUGH COASSEMBLY OF ABCBA BLOCK TERPOLYMERS WITH TITANIA SOLS*

3.1 Abstract

We report the first use of a block terpolymer for the synthesis of three-component nanocomposites. Here, the use of three chemically distinct polymer blocks enabled control over each of the three final components: partially graphitic carbon, crystalline transition metal oxide, and porosity. Tuning of the individual block lengths and block fractions resulted in control over the three components. Specifically, two PAN-*b*-PEO-*b*-PPO-*b*-PEO-*b*-PAN pentablock terpolymers were synthesized starting with a functionalized P123 or F127 macroinitiator. The PEO blocks were selectively swelled with titania sols while the PPO primarily served as a mesoporosity source and the PAN served as a carbon source with high yield. Two subsequent heat treatments were used to form partially graphitic carbon which acted as an in situ hard template preserving the mesostructure through the crystallization of the titania sols. TEM and SAXS analysis revealed worm-like microphase separation. Nitrogen physisorption analysis revealed that the pore size distributions for all nanocomposites were narrow and the distribution centers were tuned from 6.0 to 16.5 nm. The carbon content of the nanocomposites was varied from 11.3 to 35.2 wt% by increasing the fraction of PAN in the nanocomposites.

3.2 Introduction

The self-assembly of amphiphilic block copolymers has been extensively applied towards the structure-directing of porous materials. Generally, the hydrophilic block is selectively swelled with hydrophilic nanoparticles or molecular precursors via van der Waals or ionic interactions while the hydrophobic block repels these precursors.[1] Subsequent pyrolysis of such composites generates porous materials by removal of the polymer. This or similar approaches have been broadly applied to generate mesoporous silicates,[2] aluminosilicates,[3] transition metal oxides,[4-7] platinum,[8] and carbon[9-13] materials. Most examples of block copolymer derived porous multi-material composites were synthesized by selectively swelling the hydrophilic block of a block copolymer with a mixture of multiple hydrophilic precursors which resulted in a random dispersion of the two materials with ordered pores.[14-16] In order to structure-direct multiple materials separately, other approaches have utilized block copolymers where the hydrophobic block served as a carbon source to form silica-carbon[17] or titania-carbon[18] nanocomposites. The recently published CASH method utilized hydrophobic poly(isoprene) as both a porosity source and a carbon source to enable the preservation of the mesostructure during the high temperature crystallization of the transition metal oxides.[19] While this approach resulted in porous transition metal oxides with a small amount of carbon, it did not demonstrate direct control over the amount of carbon. Many of these approaches may be combined conceptually by utilizing an amphiphilic block terpolymer (having three chemically different mer units) with, for example, two different hydrophobic blocks—one hydrophobic block generates porosity, the other hydrophobic block generates carbon in high yield, and the hydrophilic block selectively swells with sol particles. Such a method would enable block sequence directed materials (BSDM), where a sequence of three or more chemically different

19

polymer blocks direct the spatial arrangement and interface definitions of multiple functional materials. The achievement of BSDMs would be a significant step towards mimicking the more complex assembly processes that result in biological nanocomposites. While there have been a few papers on aluminosilicate structure-directing with block terpolymers,[20,21] there are no reports, to the best of our knowledge, that have utilized a block terpolymer to synthesize three-component nanocomposites.

Nanocomposite materials have attracted considerable attention due to their often novel properties. Such nanocomposites are not only more homogenous than their bulk analogs, but sometimes also enable new functionality.[22,23] For example, bulk titania has poor electrode performance in Li-ion battery applications due to its very low Li diffusivity and poor electrical conductivity (semiconductor). However, porous nanoscale composites of titania with good electrical conductors, such as carbon, enable the use of titania for Li-ion battery anodes. Furthermore, shrinking the Li diffusion length in titania enables utilization of titania's fast Li insertion/desertion kinetics.[24,25] Similarly, such porous-oxide-carbon nanocomposites could also function as fuel cell electrodes by utilizing the surface proton conductivity of oxides which is comparable to that of Nafion.[26,27] Three-component nanocomposites are of great general interest for electrochemical devices such as batteries and fuel cells which all require multiple continuous pathways for the reaction of (1) reducing/oxidizing species with (2) electrons, and (3) ions.[28]

Here we report on the one-pot synthesis of three-component nanocomposites directly from the self-assembly of block terpolymers with transition metal oxide sols. Specifically, the PEO blocks of PAN-b-PEO-b-PPO-b-PEO-b-PAN pentablock terpolymers were selectively swelled with titania sols. Subsequent heat treatments transformed the microphase separated materials into mesoporous-partially
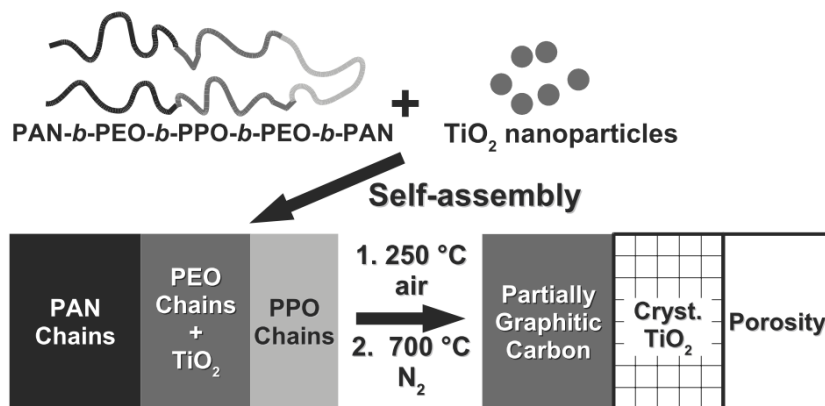
Figure 3.1: Schematic representation of one-pot synthesis of mesostructured porous-carbon-titania nanocomposites via self-assembly of a pentablock terpolymer with TiO_2 sols followed by specific heat treatments.

graphitic carbon-anatase titania nanocomposites (Figure 3.1). A nanocomposite was also made using as-received P123 for comparison. Tuning of the individual block lengths and block fractions resulted in control of all three components in three different samples: Cornell composition of materials with pores, carbon, and titania (CCM-PCT-1, CCM-PCT-2, and CCM-PCT-3).

3.3 Experimental Methods

3.3.1 Materials

For the macroinitiator synthesis, 2-bromo-2-methylpropionic acid (98%, BiB), N,N'-dicyclohexylcarbodiimide (99%, DCC), 4-(dimethylamino)pyridine (99%, DMAP), Poly(ethylene oxide)-*block*-poly(propylene oxide)-*block*-poly(ethylene oxide) triblock copolymers Pluronic P123 ($PEO_{20}PPO_{70}PEO_{20}$) and F127 ($PEO_{106}PPO_{70}PEO_{106}$), and anhydrous, methanol-free chloroform (99%) were purchased from Sigma Aldrich and used as received.

For the PAN chain extension, Acrylonitrile (99%, AN), CuBr (99.999%), $CuBr_2$
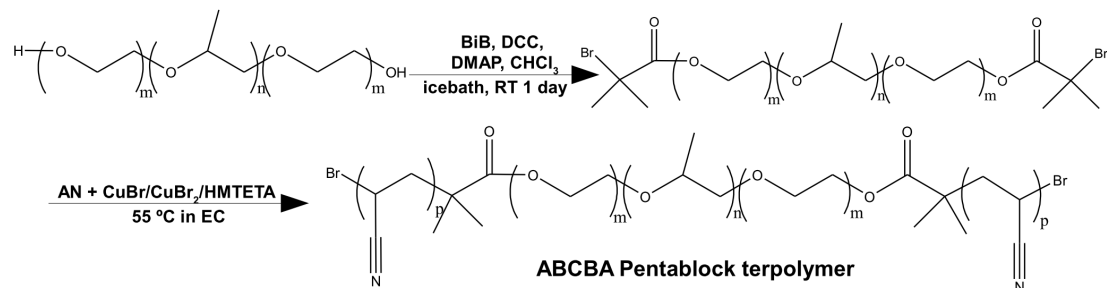
Figure 3.2: Schematic showing synthesis of block terpolymer by using an esterification to attach ATRP initiating sites to commercially available Pluronic triblock copolymers followed by ATRP chain extension of PAN.

(99.999%), basic-alumina (activity I, MP Biomedical), 1,1,4,7,10,10-hexamethyl-triethylenetetramine (97%, HMTETA), N,N-dimethylformamide (99.9%, DMF), ethylene carbonate (99%, EC) were purchased from Sigma Aldrich, and used as received. SnakeSkin dialysis tubing with a 3.5 kg/mol molecular weight cutoff was purchased from Pierce. Deionized water was prepared from a Barnstead NANOpure filtration system.

For the composite synthesis, titanium(IV) chloride (99%, Sigma Aldrich), titanium(IV) isopropoxide (97%, Sigma Aldrich), 37 wt% hydrochloric acid (ACS grade, BDH), NaBr (99%, Sigma Aldrich), and anhydrous ethanol (99%, Pharmco) were used as received. DMF and deionized water, were used for composite synthesis as detailed above.

3.3.2 Synthesis

Macroinitiator Synthesis

The P123 and F127 based macroinitiators were both prepared in a similar fashion to that reported previously (Figure 3.2).[29] The diol Pluronic triblock copolymer was dried at 40 °C under high vacuum to remove trace water. The Pluronic

polymer was then dissolved in dry, methanol-free chloroform to form a 30 wt% polymer solution under constant stirring. Then, BiB was added to the solution in a 2.35:1 molar ratio of BiB:polymer with an overflow of nitrogen. The solution was cooled in an ice bath before the next additions. Then, DCC was added to the stirred solution and quickly followed by DMAP in a 2.35:0.37:1 molar ratio of DCC:DMAP:polymer. The solution turned cloudy indicating transformation of the DCC to the corresponding urea. The reaction was stirred for 5 minutes in contact with the ice bath and then allowed to stir at room temperature for 1 day. The polymer solution was filtered through a glass frit to remove most of the urea and then syringe filtered. The chloroform was removed with rotary evaporation and the polymer was redissolved in THF and refiltered. The THF was then removed by rotary evaporation and the product was dried under high vacuum for at least 1 day. ^{1}H NMR spectroscopy was used to confirm the quantitative chain end transformation of the Pluronic polymer to form the macroinitiator (Pluronic-Br$_2$) with a bromine end group at each end.

PAN Chain Extension

Acrylonitrile was flowed over basic-alumina to remove the inhibitor. Each polymerization was carried out in a glass reactor equipped with a septum and attached to a Schlenk line via a rubber hose. The Pluronic-Br$_2$ macroinitiator was added to reactor along with a stir bar. Nitrogen was flowed through the reactor as molten EC and AN were added via the septum port. The reactor contents were stirred at 40 °C until a homogeneous solution was formed. The septum was replaced and the reactor was subjected to 3 freeze-pump-thaw cycles and then backfilled with positive nitrogen pressure. Two catalyst stock solutions were prepared separately in a glovebox. The CuBr stock solution contained equal moles of CuBr and degassed

HMTETA and was dissolved in degassed DMF to a concentration of 10 mg CuBr per mL. The $CuBr_2$ solution was prepared in the same fashion. The reactor was placed in an oil bath maintained at 55 °C by a stirring hot plate. The $CuBr_2$ stock solution was added to the reactor via the septum, followed by the CuBr stock solution. All polymerizations were carried out with molar ratios of 0.5:0.1:0.08:0.02:250 for Pluronic-Br_2:HMTETA:CuBr:$CuBr_2$:AN with EC added to make the initial AN concentration 5.25 M. A timer was started immediately and the polymerization was stopped at the desired conversion by exposing the reactor contents to air. The reaction contents were diluted to twice the volume with DMF and dialysed against deionized water 3 times for at least 12 hours. The contents of the dialysis bag were rotary evaporated to remove water and then dried for a day under high vacuum. The resulting product was white to yellow depending on the amount of PAN grown. The resulting PAN-b-PEO-b-PPO-b-PEO-b-PAN pentablock terpolymer (Pluronic-PAN) was characterized by ^{1}H NMR and GPC. The PAN molecular weight was calculated from the ^{1}H NMR data and the polydispersity was determined by GPC. Two different terpolymers were used to make nanocomposites: Pluronic-PAN1 and Pluronic-PAN2. Pentablock terpolymer Pluronic-PAN1 was synthesized from P123 and had a number average molecular weight of 6.35 kg/mol, a polydispersity of 1.52, and was composed of 8.25 wt% PAN and 27.7 wt% PEO. Pluronic-PAN2, was synthesized from F127 and had a number average molecular weight of 21.5 kg/mol, a polydispersity of 1.37, and was composed of 37.7 wt% PAN and 43.4 wt% PEO. The as-received P123 and F127 had reported number average molecular weights of 5.8 and 12.6 kg/mol, respectively. The polydispersities of P123 and F127 were determined with GPC to be 1.34 and 1.46, respectively. For nanocomposite comparison, a third sample was synthesized using as-received P123. All polymers used had a 4.1 kg/mol PPO center block.

Composite Synthesis

All composites were synthesized using hydrolytic sol-gel routes for titania. Each sample was synthesized from a different polymer. CCM-PCT-1 was synthesized by dissolving 0.109 g Pluronic-PAN1 in 3.7 mL of ethanol and 0.3 g of hydrochloric acid under rapid stirring at 85 °C for 3 hours. The solution was cooled to 40 °C and 0.313 mL of titanium isopropoxide was added while stirring. The solution was stirred at 40 °C for 20 hours. The solution was cast in a teflon dish inside a box oven set to 35 °C with 50-60%RH maintained by a stirred and fan blown saturated aqueous NaBr salt bath for 5 days. The film was then heated to 80 °C for 7 more days to crosslink the sol. The film was then heated in air at 1 °C/min to 250 °C and held for 2 hours to cyclize the PAN. Lastly, the film was heated at 1 °C/min to 700 °C under nitrogen flow and held for 2 hours to carbonize the PAN and crystallize the titania.

CCM-PCT-2 was synthesized by dissolving 0.250 g of Pluronic-PAN2 in 25 mL of DMF followed by the dropwise addition of 0.91 mL of ethanol. The polymer solution was brought into a glove bag where 0.171 mL of titanium chloride was added under rapid stirring. The solution was stirred for an hour before being cast in an open teflon dish maintained at 40 °C for 7 days. The film was dried under high vacuum for several hours and then subjected to the same 250 °C and 700 °C heat treatments under air and nitrogen, respectively.

For comparison, sample CCM-PCT-3 was synthesized from as-received P123. The same conditions were used as previously reported by the Zhao group for pure TiO_2,[30] except the calcination steps were performed using the same two step heat treatment used for samples CCM-PCT-1 and CCM-PCT-2.

3.3.3 Equipment

Gel Permeation Chromatography (GPC)

GPC measurements were performed in DMF with 10 μm Polymer Standards Service (PSS, Warmick, RI) GRAM columns (10^2, 10^3, $3 \cdot 10^3$ Å, 300 mm long each, and 8 mm in diameter) at a flow rate of 1.0 mL/min. An Agilent 1200 refractive index detector operated at 40 °C was used to detect the polymer. Raw data were processed using PSS-Win GPC V6.2 software. Molecular weight distributions (M_w/M_n) were calculated using a poly(styrene) calibration curve.

^{1}H Nuclear Magnetic Resonance (NMR)

^{1}H solution NMR spectra were recorded on a Varian INOVA 400 Mhz spectrometer using the deuterated chloroform signal (δ=7.27 ppm) or the deuterated dimethyl-sulfoxide signal (δ=2.50 ppm) as an internal standard.

Transmission Electron Microscopy (TEM)

Samples were ultrathin sectioned at -55 °C with a Leica Ultracut UCT microtome. Sample slices were collected on a water/DMSO eutectic solution and transferred to 300 mesh copper grids (no carbon film). A Technai T12 operating at 120 kV was used to image the sections.

Small-angle X-ray Scattering (SAXS)

SAXS data were collected on a Rigaku RU300 which used a copper rotating anode (λ=1.54 Å) operated at 40 kV and 50 mA. The X-rays were monochromated using a Ni filter and focused using orthogonal Franks mirrors. The SAXS patterns were collected with a homebuilt 1k x 1k pixel CCD detector similar to that described

elsewhere.[31] Data are presented as q $= 4\pi\sin(\theta)\lambda^{-1}$, where 2θ is the total scattering angle.

Raman Spectroscopy

Raman spectra were collected on a Renishaw InVia microRaman system using a 488 nm laser.

Powder X-ray diffraction (XRD)

XRD spectra were collected on a Scintag - diffractometer using Cu Kα radiation (λ=1.54 Å).

Thermal Gravimetric Analysis (TGA)

TGA analysis was performed with flowing air on a TG/DTA 320 at a heating rate of 20 °C/min to 550 °C and held for 2 hours. The sample mass in all TGA curves was normalized at 150 °C to eliminate mass loss due to water desorption.

Nitrogen Physisorption Analysis

Isotherms were measured at -196 °C using a Micromeritics ASAP 2020 system. The samples were degassed at 150 °C overnight under high vacuum. The Brunauer, Emmett, and Teller (BET) and Brunauer, Jonyer, and Halenda (BJH) analysis were performed using Micromeritics ASAP 2020 V1.05 software.
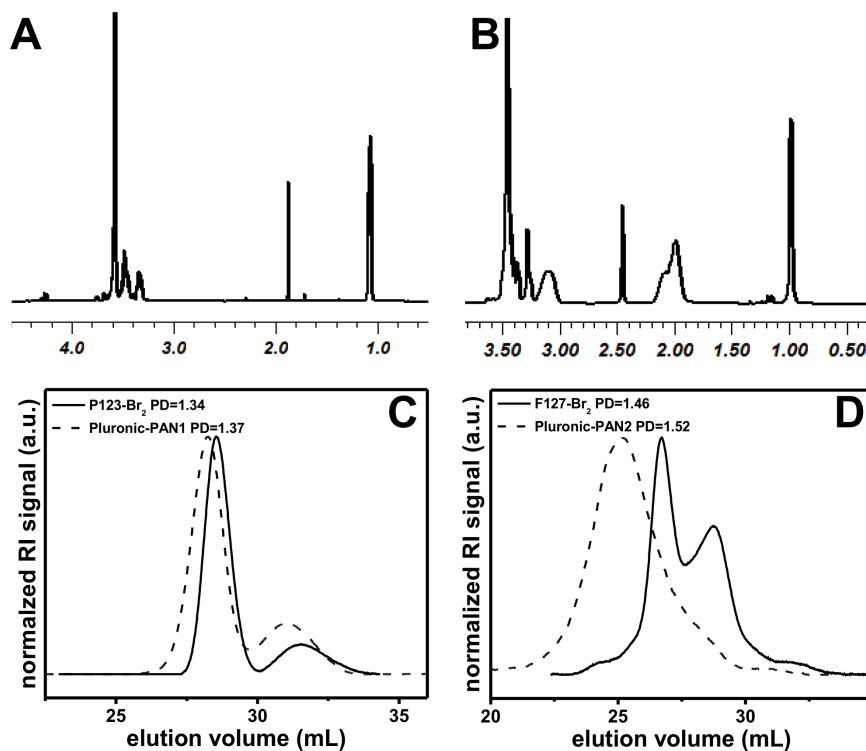
Figure 3.3: The end group transformation in the macroinitiator synthesis was determined to be quantitative by comparing the PPO ^{1}H NMR peak near 1.0 ppm to the peak corresponding to the methyl groups of the initiator near 1.9 ppm (A). Similarly, the PAN molecular weight after chain extension was determined by comparing the PAN backbone peaks at 2.0 and 3.2 ppm to the PPO peak near 1.0 ppm (B). The GPC elugrams for Pluronic-PAN1 (C) and Pluronic-PAN2 (D) shifted to lower elution volumes indicating that the Pluronic-PAN polymers (dashed lines) increase in molecular weight relative to their macroinitiators (solid lines).

3.4 Results and Discussion

3.4.1 Synthesis of Pluronic-PAN Pentablock Terpolymers

Pluronic block copolymers P123 and F127 have been extensively studied for structure-directing porous materials and thus serve as a suitable starting point for block terpolymer synthesis. We sought to add graphitic carbon to these nanocomposites to aim for the high electrical conductivity and thermodynamic stability desirable for electron conduction in electrochemical applications. Poly(acrylonitrile) is a well established source of graphitic carbon and is commercially used for the production of graphitic carbon fibers.[32] There are numerous examples of the controlled radical polymerization of PAN, especially using atom transfer radical polymerization (ATRP).[17,33–40] To this end an initiator of suitable kinetic activity[41] for PAN growth was attached to the alcohol end groups of Pluronic block copolymers via a Steglich esterification. The resulting Pluronic-Br$_2$ macroinitiator was then used for chain extension using ATRP. ATRP of PAN can be challenging due to a side reaction with the activator CuBr, often limiting achievable molecular weights to c.a. 10 kg/mol.[35] Although AGET ATRP was shown to greatly suppress this side reaction,[39] standard ATRP was instead used to keep the polydispersity as low as possible. To this end, all polymerizations were performed with a 10:0.8 ratio of chain ends to CuBr. This side reaction was further suppressed by utilizing a tetradentate ligand (HMTETA) to saturate the coordination sites of the Cu better than the commonly employed bipyridine ligands. HMTETA has a similar kinetic activity to bipyridine[42] and was found (unpublished work) to enable the synthesis of much larger PAN blocks with similarly low polydispersities. The purified product was characterized by NMR to determine the PAN molecular weight and GPC to determine the polydispersity. The GPC elugrams of the starting triblock

copolymers P123 and F127 had bimodal molecular weight distributions as previously reported.[43] Elugrams of Pluronic-PAN1 and Pluronic-PAN2 showed a shift to higher molecular weights while maintaining similar polydispersities to the parent Pluronic polymers (Figure 3.3 C and D).

3.4.2 Synthesis of Mesoporous-Carbon-Titania Nanocomposites

A simple one-pot approach was used to synthesize three-component nanocomposites. The structure-directing polymer was dissolved in a suitable solvent and a hydrolytic titania sol was synthesized in the same solution. Films were cast to remove volatile solvents, leading to micophase separation of polymer blocks with the titania sol particles selectively swelling the hydrophilic PEO block. The titania sol is highly protonated under the acidic conditions typically utilized and does not condense appreciable until sufficient HCl has volatilized.[15] The films were aged at a low temperature to provide time for titania gelation before further heat treatments. The subsequent heat treatment to 250 °C in air is well known to cyclize the PAN blocks to form a rigid ladder like polymer backbone which increases the carbon yield. The cyclized PAN chains further react thermally in inert atmosphere via dehydrogenation (400-600 °C) and denitrogenation (600-1300 °C) reactions to form carbon materials.[32] The second heat treatment to 700 °C under nitrogen carbonized the PAN, crystallized the amorphous titania sol, and generated mesoporosity from the PPO pyrolysis.

The microphase separation of Pluronic-PAN and as-cast nanocomposites was investigated with diffraction studies. The XRD spectrum of neat Pluronic-PAN2 has peaks at 17.0, 19.2, and 23.3° (Figure 3.4 D bottom). The peaks at 19.2 and 23.3° correspond to PEO crystallites[44] and the peak at 17.0° corresponds to

30
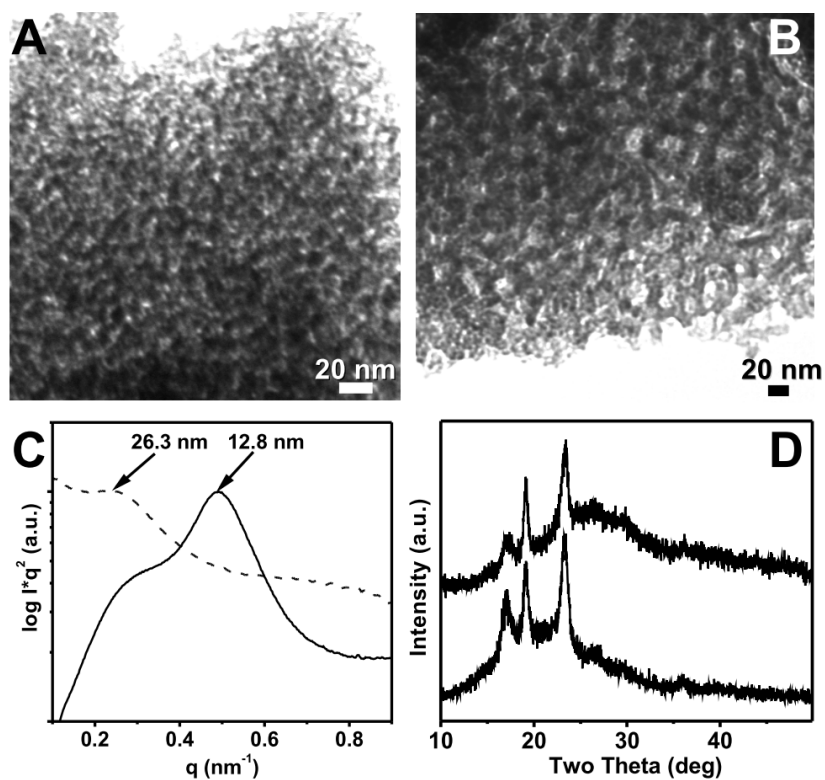
Figure 3.4: TEM images of three-component porous-carbon-titania nanocomposites CCM-PCT-1 (A) and CCM-PCT-2 (B) with worm-like structures resulted from microphase separation of Pluronic-PAN1 and Pluronic-PAN2 block terpolymers, respectively. SAXS (C) of CCM-PCT-1 (solid line) and CCM-PCT-2 (dashed line) nanocomposites exhibited a single peak corresponding to the length scale of the microphase separation. XRD (D) of neat Pluronic-PAN (bottom) and an as-cast film CCM-PCT-2 (top) show discrete crystallites of PAN and PEO indicating block terpolymer microphase separation before pyrolysis.

PAN crystallites.[45] The XRD observation of separate PEO and PAN crystallites is consistent with the expected microphase separation of the semi-crystalline PEO, semi-crystalline PAN, and amorphous PPO domains. Furthermore, the SAXS patterns of Pluronic-PAN1 and Pluronic-PAN2 each have a single broad peak at c.a. 11 and 15 nm, respectively, corresponding to the short-range order resulting from worm-like microphase separation of the neat polymers (Figure 3.4 C). These results were not unexpected considering that both PEO-b-PPO-b-PEO[43] and PEO-b-PAN[17] polymers are known to microphase separate. The composite materials resulting from Pluronic-PAN polymers had similar XRD peaks at 17.0, 19.2, and 23.3° in addition to a broad peak centered near 25° (Figure 3.4 D top). The presence of PAN and PEO crystallites in composite materials is again a strong indication for the microphase separation of PAN, PEO, and PPO. The broad peak centered near 25° is attributed to the amorphous titania sol. Although PEO crystallization is known to be suppressed by the fractal oxide networks resulting from silicate sol-gel processes,[3] the closo oxide particles[6] resulting from the hydrolytic titania sol-gel processes used here did not completely suppress the PEO crystallization. The complete mixing of PEO with oxide sol particles, and thus complete suppression of PEO crystallization, is not necessary for PEO based amphiphiles to structure-direct oxide materials.[46] We suspect that the titania sol is mixed selectively with the amorphous regions of the PEO[47] and excluded from the crystalline PEO regions. Although mechanistically interesting, the small regions of crystalline PEO did not prevent the synthesis of three-component nanocomposites.

We take the three-component nanocomposite CCM-PCT-1 as a representative example of composites synthesized from Pluronic-PAN block terpolymers. The bright field TEM image of the final calcined porous-carbon-titania nanocomposite (Figure 3.4 A) showed worm-like phase separation of the porosity (light) from the
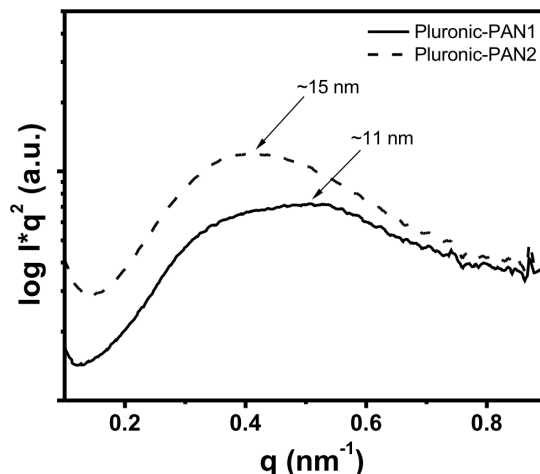
Figure 3.5: Integrated SAXS profiles of Pluronic-PAN1 (solid) and Pluronic-PAN2 (dashed) each have a single peak corresponding to the short-range ordering resulting from the block terpolymer microphase separation.

carbon and titania (both dark) with a period of c.a. 13 nm. Contrast was not observed between the carbon and titania components in bright field TEM. Such short-range ordered microphase separation is commonly found in mesostructures derived from PAN based block copolymers[38,48–52] due to the high glass transition temperature (85-110 °C) and high melting temperature (320 °C) for the partially crystalline PAN block.[53] The single SAXS peak at 12.8 nm was consistent with the observed length scale of the worm-like morphology in TEM (Figure 3.5).

The titania and carbon of CCM-PCT-1 were further characterized to determine their type and relative proportions. The XRD spectrum showed several well-resolved peaks on a flat baseline suggesting that the amorphous titania sol particles were successfully converted to crystalline material (Figure 3.6 A). All of the observed XRD peaks were consistent with the anatase phase of titania (PDF # 21-1272). The Debye-Scherrer formula was used to calculate the crystallite size from the peak widths. This equation was applied to the non-overlapping peaks near 25 and 48° two-theta to calculate an average crystallite size of 9.4 nm. The
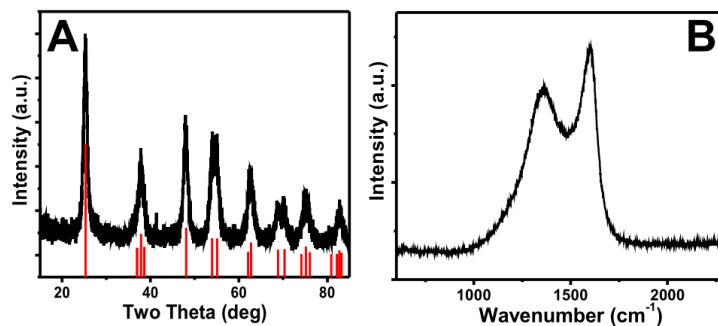
Figure 3.6: The powder XRD of CCM-PCT-1 (A) matches the indicated peaks for anatase titania (PDF #21-1272). The Raman spectrum of CCM-PCT-1 (B) was consistent with partially graphitic carbon.
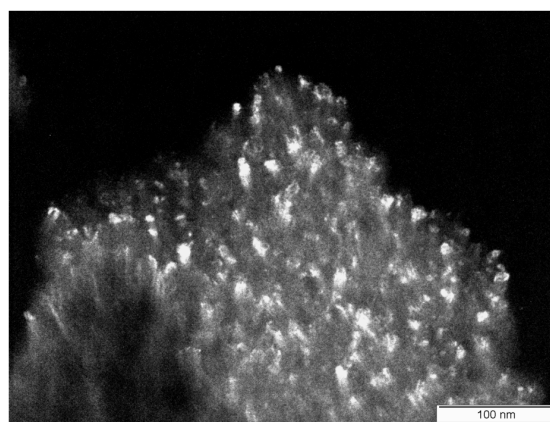
Figure 3.7: Dark field TEM image of CCM-PCT-1 showing c.a. 10 nm titania nanocrystallites (white) embedded in porous carbon (gray).
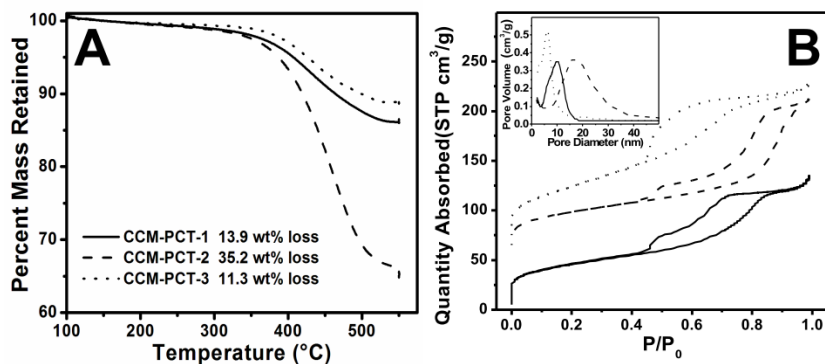
Figure 3.8: Oxidative TGA (A) was used to determine the carbon content of each nanocomposite. Nitrogen physisorption isotherms (B) were used to calculate the mesoporous surface area, microporous surface area, pore volume, and pore size distribution (inset) for each nanocomposite. Isotherms were offset to aid viewing. Tuning of the terpolymer block lengths enabled control over the porosity and carbon content of the nanocomposites.

titania crystallite size was consistent with length scale of the microphase separation determined by TEM (13 nm) and SAXS (12.8 nm). Furthermore, dark field TEM was used to directly view the 9-14 nm diameter titania nanoparticles (Figure 3.7). Raman spectroscopy was used to determine the type of carbon in the nanocomposite. The Raman spectrum had two pronounced peaks centered at 1,600 and 1,358 cm^{-1}, respectively (Figure 3.6 B). Often, Raman spectra of carbon materials are convolutions of several peaks, possibly including those for ideal graphite (G 1,580 cm^{-1}), a disordered graphitic lattice (D1 1,350 cm^{-1}, D2 1,620 cm^{-1}, and D4 1,200 cm^{-1}), or amorphous carbon (D3 1,500 cm^{-1}).[54] The significant G, D1, and D2 character in the Raman spectrum of CCM-PCT-1 was consistent with partially graphitic carbon composed of turbostatic graphite crystallites less than 7 nm in extent and with very little amorphous content (D3).[55,56] Partially graphitic carbon is expected to result from such a low carbonization temperature. The fraction of carbon in the nanocomposite was determined by oxidative TGA (Figure 3.8 A solid line). The sample had a single mass loss step

starting at c.a. 400 °C corresponding to oxidative removal of the carbon from the nanocomposite. CCM-PCT-1 lost 13.9% of the normalized mass, suggesting that the composite was composed of 13.9 wt% carbon. The change in sample color from black initially to white after TGA further supports that the mass loss is due to the loss of carbon. The amount of carbon in the nanocomposite is consistent with the typical 50 wt% carbon yield for PAN[54] combined with a c.a. 10 wt% carbon yield for the Pluronic (discussed further for CCM-PCT-3). The XRD, Raman, and TGA data suggest that CCM-PCT-1 was composed of crystalline anatase titania and 13.9 wt% partially graphitic carbon.

A nitrogen physisorption experiment was performed to characterize the porosity in CCM-PCT-1. The nanocomposite had a type IV isotherm (Figure 3.8 B solid line) indicating that it had open and accessible mesoporosity. Our previously published work utilizing PEO-b-PAN structure-directing agents[18] were not mesoporous, indicating the need for an additional hydrophobic block as a mesoporosity source. A narrow pore size distribution centered at 10.0 nm was calculated from the adsorption branch of the isotherm using the BJH model (Figure 3.8 B inset solid line). The average mesopore size of CCM-PCT-1 was considerably larger than the 5-9 nm pore sizes normally resulting from the microphase separation of P123 based hybrids.[2] We suspect that the crystallization of the PAN stretches the PEO and PPO blocks, an effect thoroughly investigated in a recent study.[57] Such a stretched conformation of the PPO is consistent with the increased pore size. Sample CCM-PCT-1 had 0.21 cm^3/g of pore volume and the BET model was used to determine that the nanocomposite had a total surface area of 163 m^2/g. The sample had 36 m^2/g of microporous surface area primarily due to the presence of carbon. Subtraction of the microporous surface area from the total surface area revealed that CCM-PCT-1 had 127 m^2/g of mesoporous surface area.

The physisorption analysis revealed that nanocomposite CCM-PCT-1 had both mesoporosity and microporosity consistent with the microphase separation and carbon yield of the block terpolymer used. Sample CCM-PCT-1, to the best of our knowledge, is the first three-component nanocomposite synthesized directly from the microphase separation of a block terpolymer. The use of a simple one-pot approach enabled the synthesis of a mesoporous nanocomposite composed of partially graphitic carbon and crystalline anatase titania.

3.4.3 Composition and Porosity Control with Polymer Variation

A different nanocomposite, CCM-PCT-2, was synthesized from Pluronic-PAN2 for comparison. The polymer used in this case was based instead on F127 which has the same PPO center, but longer PEO blocks. Furthermore, in this case much longer PAN blocks were grown from the ends of the macroinitiator. Bright field TEM of the final calcined three-component nanocomposite again showed worm-like phase separation of the block terpolymer (Figure 3.4 B). The 29 nm worm spacing was larger than in CCM-PCT-1 (13 nm), which was consistent with the longer block terpolymer used for CCM-PCT-2. The increased length scale of the microphase separation was further supported by the shift of the SAXS peak to a lower q value, corresponding to 26.3 nm (Figure 3.4 C). The XRD and Raman spectroscopy were again consistent with crystalline anatase titania (average domain size 9.4 nm) and partially graphitic carbon. The TEM, SAXS, XRD, and Raman spectroscopy of CCM-PCT-2 were qualitatively similar to CCM-PCT-1, except the phase separation occurred on a longer length scale consistent with the longer block terpolymer used.

The differences in carbon content and porosity were characterized by TGA and

nitrogen physisorption analysis. The oxidative TGA of CCM-PCT-2 exhibited a single weight loss step starting around 400 °C, suggesting that this nanocomposite contained 35.2 wt% carbon (Figure 3.8 A dashed line). The carbon content was again consistent with the expected 50 wt% carbon yield from PAN combined with c.a. 10 wt% carbon yield from the Pluronic. Sample CCM-PCT-2 had more than twice the carbon content of CCM-PCT-1 due to the much larger PAN fraction of the block terpolymer coupled with a similar Titania:EO molar ratio (c.a. 1.55). Thus the PAN fraction of a Pluronic-PAN block terpolymer can tune the carbon content of the final three-component nanocomposite when all other conditions are held constant.

The increased PAN fraction in the Pluronic-PAN2 used for CCM-PCT-2 also effected the resulting porosity. The nitrogen physisorption analysis of CCM-PCT-2 exhibited a type IV isotherm (Figure 3.8 B dashed line). Analysis of this isotherm showed a much larger total surface area of 238 m^2/g and pore volume of 0.27 cm^3/g. The mesoporous surface area of 131 m^2/g was nearly identical to that of CCM-PCT-1. The much larger microporous surface area of 107 m^2/g in CCM-PCT-2 is attributed to its larger carbon fraction. The BJH analysis on the adsorption isotherm indicated that the mesopores had a narrow distribution of pore diameters centered at 16.5 nm (Figure 3.8 B inset dashed line). The larger PAN fraction and PAN molecular weight of the polymer used in CCM-PCT-2 is expected to result in higher PAN crystallinity and thus cause more PEO and PPO chain stretching. The expected additional PPO chain stretching is consistent with the observed increase in mesopore diameter. The use of a block terpolymer with a larger weight fraction of PAN resulted in a nanocomposite that had more wt% carbon, larger diameter mesopores, and increased microporous surface area.

A control sample, CCM-PCT-3, was synthesized from P123 to further under-
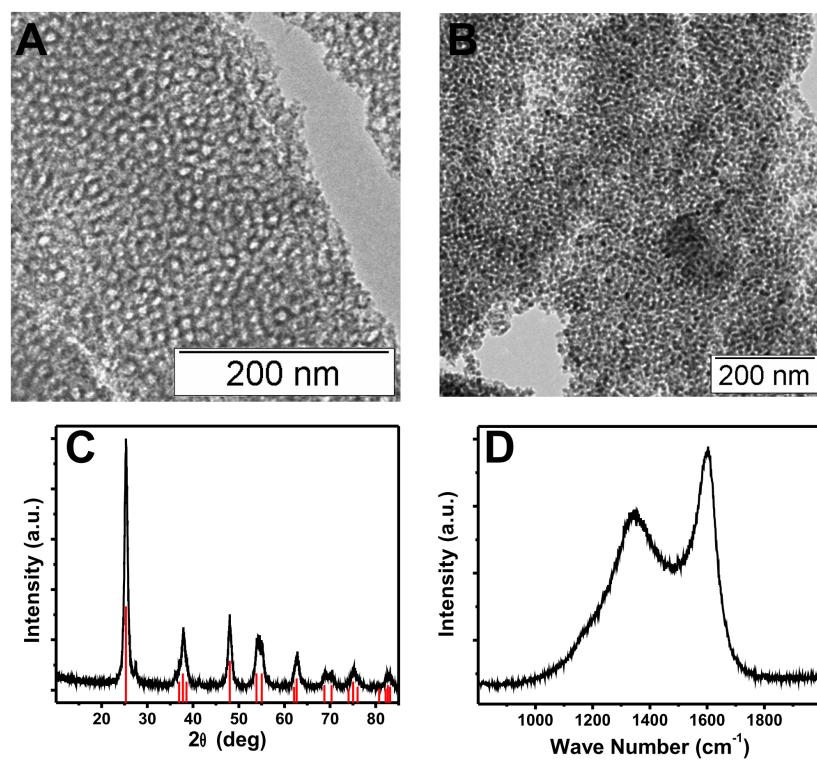
Figure 3.9: The mesostructure of the nanocomposite made from as-received P123 was preserved through the 250 °C heat treatment in air (A), but collapsed upon subsequent calcination to 700 °C in N$_2$ forming CCM-PCT-3 (B). Although the original mesostructure was not preserved, the resulting nanocomposite had a powder XRD spectrum (C) consistent with anatase titania (PDF #21-1272) and a Raman spectrum (D) consistent with partially graphitic carbon.

stand the role of PAN in the previous nanocomposites. Although others have reported nearly complete removal of Pluronic polymers under either oxidative[2] or inert[15] atmospheres, we found that the two step heat treatment utilized here resulted in an appreciable carbon residue. Subsequent oxidative TGA of CCM-PCT-3 showed a single step weight loss starting at 400 °C corresponding to the loss of 11.3 wt% carbon (Figure 3.8 A dotted line). This amount of carbon residue corresponds to a 10.7 wt% carbon yield from P123. The heat treatment to 250 °C in air likely converts the Pluronic to some partially pyrolized products which were then more stable under the subsequent heat treatment to 700 °C under N_2. TEM of CCM-PCT-3 showed that the inverse hexagonal structure present after the 250 °C heat treatment collapsed during the subsequent 700 °C calcination (Figure 3.9 A and B). Thus, the carbon resulting from P123 alone was insufficient to preserve the mesostructure during crystallization of the titania. In contrast, the in-situ hard template resulting from PAN carbonization in CCM-PCT-1 and CCM-PCT-2 acted as a scaffold to preserve the mesostructure during the high temperature titania crystallization. Nitrogen physisorption analysis showed that CCM-PCT-3 had a type IV isotherm with a H2 type hysteresis loop[58] (Figure 3.8 B dotted line). This hysteresis loop is indicative of ink-bottle type pores and is due to the connected interstitial spaces of the collapsed mesostructure. BJH analysis of the adsorption branch showed a narrow mesopore diameter distribution with a maximum at 6.0 nm (Figure 3.8 B inset dotted line). Although the originally ordered mesostructure collapsed during calcination to form CCM-PCT-3, the final material had a powder XRD spectrum consistent with crystalline anatase titania (average domain size 10.8 nm) and a Raman spectrum consistent with partially graphitic carbon (Figure 3.9C and D). Thus nanocomposite CCM-PCT-3 may still be of interest for electrochemical applications. The addition of PAN to Pluronic

polymers was necessary to preserve the microphase separated structure through calcination.

3.5 Conclusions

We report the first use of a block terpolymer for the synthesis of three-component nanocomposites towards the goal of block sequence directed materials (BSDM). Pluronic-PAN block terpolymers were synthesized from P123 and F127 macroinitiators. The resulting pentablock terpolymers were used in a simple one-pot process to produce porous nanocomposites containing tunable amounts of partially graphitic carbon and anatase titania. A sample was also made with P123 for comparison. The average mesopore diameter increased with the PAN content of the polymers. The tuning of the mesopore size is attributed to the induced PPO chain stretching due to PAN crystallization. The porosity, carbon, and titania in these nanocomposites were all controlled by varying the block ratios and molecular weights of the polymers used during self-assembly. We expect that such nanocomposites will play an increasing role in applications for energy conversion, generation, and storage.

3.6 Acknowledgements

REFERENCES

[1] S. C. Warren, F. J. Disalvo, and U. Wiesner. Nanoparticle-tuned assembly and disassembly of mesostructured silica hybrids (vol 6, pg 156, 2007). *Nature Materials*, 6(3):248–248, 2007.

[2] D. Y. Zhao, J. L. Feng, Q. S. Huo, N. Melosh, G. H. Fredrickson, B. F. Chmelka, and G. D. Stucky. Triblock copolymer syntheses of mesoporous silica with periodic 50 to 300 angstrom pores. *Science*, 279(5350):548–552, 1998.

[3] M. Templin, A. Franck, A. DuChesne, H. Leist, Y. M. Zhang, R. Ulrich, V. Schadler, and U. Wiesner. Organically modified aluminosilicate mesostructures from block copolymer phases. *Science*, 278(5344):1795–1798, 1997.

[4] P. D. Yang, D. Y. Zhao, D. I. Margolese, B. F. Chmelka, and G. D. Stucky. Generalized syntheses of large-pore mesoporous metal oxides with semicrystalline frameworks. *Nature*, 396(6707):152–155, 1998.

[5] P. D. Yang, D. Y. Zhao, D. I. Margolese, B. F. Chmelka, and G. D. Stucky. Block copolymer templating syntheses of mesoporous metal oxides with large ordering lengths and semicrystalline framework. *Chemistry of Materials*, 11(10):2813–2826, 1999.

[6] E. L. Crepaldi, Gjda Soler-Illia, D. Grosso, F. Cagnol, F. Ribot, and C. Sanchez. Controlled formation of highly organized mesoporous titania thin films: From mesostructured hybrids to mesoporous nanoanatase tio2. *Journal of the American Chemical Society*, 125(32):9770–9786, 2003.

[7] S. Y. Choi, M. Mamak, N. Coombs, N. Chopra, and G. A. Ozin. Thermally stable two-dimensional hexagonal mesoporous nanocrystalline anatase, meso-tio2: Bulk and crack-free thin film morphologies. *Advanced Functional Materials*, 14(4):335–344, 2004.

[8] S. C. Warren, L. C. Messina, L. S. Slaughter, M. Kamperman, Q. Zhou, S. M. Gruner, F. J. DiSalvo, and U. Wiesner. Ordered mesoporous materials from metal nanoparticle-block copolymer self-assembly. *Science*, 320(5884):1748–1752, 2008.

[9] R. Ryoo, S. H. Joo, and S. Jun. Synthesis of highly ordered carbon molecular sieves via template-mediated structural transformation. *Journal of Physical Chemistry B*, 103(37):7743–7746, 1999.

[10] J. Lee, S. Yoon, T. Hyeon, S. M. Oh, and K. B. Kim. Synthesis of a new mesoporous carbon and its application to electrochemical double-layer capacitors. *Chemical Communications*, (21):2177–2178, 1999.

[11] J. Kim, J. Lee, and T. Hyeon. Direct synthesis of uniform mesoporous carbons from the carbonization of as-synthesized silica/triblock copolymer nanocomposites. *Carbon*, 42(12-13):2711–2719, 2004.

[12] C. D. Liang, K. L. Hong, G. A. Guiochon, J. W. Mays, and S. Dai. Synthesis of a large-scale highly ordered porous carbon film by self-assembly of block copolymers. *Angewandte Chemie-International Edition*, 43(43):5785–5789, 2004.

[13] Y. H. Deng, T. Yu, Y. Wan, Y. F. Shi, Y. Meng, D. Gu, L. J. Zhang, Y. Huang, C. Liu, X. J. Wu, and D. Y. Zhao. Ordered mesoporous silicas and carbons with large accessible pores templated from amphiphilic diblock copolymer poly(ethylene oxide)-b-polystyrene. *Journal of the American Chemical Society*, 129(6):1690–1697, 2007.

[14] J. Fan, S. W. Boettcher, and G. D. Stucky. Nanoparticle assembly of ordered multicomponent mesostructured metal oxides via a versatile sol-gel process. *Chemistry of Materials*, 18(26):6391–6396, 2006.

[15] R. L. Liu, Y. F. Shi, Y. Wan, Y. Meng, F. Q. Zhang, D. Gu, Z. X. Chen, B. Tu, and D. Y. Zhao. Triconstituent co-assembly to ordered mesostructured polymer-silica and carbon-silica nanocomposites and large-pore mesoporous carbons with high surface areas. *Journal of the American Chemical Society*, 128(35):11652–11662, 2006.

[16] R. Liu, Y. Ren, Y. Shi, F. Zhang, L. Zhang, B. Tu, and D. Zhao. Controlled synthesis of ordered mesoporous c-tio2 nanocomposites with crystalline titania frameworks from organic-inorganic-amphiphilic coassembly. *Chemistry of Materials*, 20(3):1140–1146, 2008.

[17] M. Kruk, B. Dufour, E. B. Celer, T. Kowalewski, M. Jaroniec, and K. Matyjaszewski. Well-defined poly(ethylene oxide)-polyacrylonitrile diblock copolymers as templates for mesoporous silicas and precursors for mesoporous carbons. *Chemistry of Materials*, 18(6):1417–1424, 2006.

[18] M. Stefik, J. Lee, and U. Wiesner. Nanostructured carbon-crystalline titania composites from microphase separation of poly(ethylene oxide-b-acrylonitrile) and titania sols. *Chemical Communications*, pages 2532–2534, 2009.

[19] J. Lee, M. C. Orilall, S. C. Warren, M. Kamperman, F. J. Disalvo, and U. Wiesner. Direct access to thermally stable and highly crystalline mesoporous transition-metal oxides with uniform pores. *Nature Materials*, 7(3):222–228, 2008.

[20] G. E. S. Toombes, S. Mahajan, M. Weyland, A. Jain, P. Du, M. Kamperman, S. M. Gruner, D. A. Muller, and U. Wiesner. Self-assembly of four-layer

woodpile structure from zigzag abc copolymer/aluminosilicate concertinas. *Macromolecules*, 41(3):852–859, 2008.

[21] G. E. S. Toombes, S. Mahajan, M. Thomas, P. Du, M. W. Tate, S. M. Gruner, and U. Wiesner. Hexagonally patterned lamellar morphology in abc triblock copolymer/aluminosilicate nanocomposites. *Chemistry of Materials*, 20(10):3278–3287, 2008.

[22] J. Y. Ying, C. P. Mehnert, and M. S. Wong. Synthesis and applications of supramolecular-templated mesoporous materials. *Angewandte Chemie-International Edition*, 38(1-2):56–77, 1999.

[23] F. Schuth and W. Schmidt. Microporous and mesoporous materials. *Advanced Materials*, 14(9):629–638, 2002.

[24] Y. G. Guo, J. S. Hu, and L. J. Wan. Nanostructured materials for electrochemical energy conversion and storage devices. *Advanced Materials*, 20(23):4384–4384, 2008.

[25] P. G. Bruce, B. Scrosati, and J. M. Tarascon. Nanomaterials for rechargeable lithium batteries. *Angewandte Chemie-International Edition*, 47(16):2930–2946, 2008.

[26] F. M. Vichi, M. I. Tejedor-Tejedor, and M. A. Anderson. Effect of pore-wall chemistry on proton conductivity in mesoporous titanium dioxide. *Chemistry of Materials*, 12(6):1762–1770, 2000.

[27] M. T. Colomer. Proton conductivity of nanoporous anatase xerogels prepared by a particulate sol-gel method. *Journal of Solid State Electrochemistry*, 10(1):54–59, 2006.

[28] R. O'Hayre and F. B. Prinz. The air/platinum/nafion triple-phase boundary: Characteristics, scaling, and implications for fuel cells. *Journal of the Electrochemical Society*, 151(5):A756–A762, 2004.

[29] N. V. Tsarevsky, T. Sarbu, B. Gobelt, and K. Matyjaszewski. Synthesis of styrene-acrylonitrile copolymers and related block copolymers by atom transfer radical polymerization. *Macromolecules*, 35(16):6142–6148, 2002.

[30] W. Y. Dong, Y. J. Sun, C. W. Lee, W. M. Hua, X. C. Lu, Y. F. Shi, S. C. Zhang, J. M. Chen, and D. Y. Zhao. Controllable and repeatable synthesis of thermally stable anatase nanocrystal-silica composites with highly ordered hexagonal mesostructures. *Journal of the American Chemical Society*, 129:13894–13904, 2007.

[31] M. W. Tate, E. F. Eikenberry, S. L. Barna, M. E. Wall, J. L. Lowrance, and S. M. Gruner. A large-format high-resolution area x-ray-detector based

on a fiberoptically bonded charge-coupled-device (ccd). *Journal of Applied Crystallography*, 28:196–205, 1995.

[32] Jean-Baptiste Donnet and Roop Chand Bansal. *Carbon Fibers.* M. Dekker, 2nd rev edition, 1990.

[33] S. M. Jo, H. J. Paik, and K. Matyjaszewski. Polyacrylonitrile with low poly-dispersities by atom transfer radical polymerization. *Abstracts of Papers of the American Chemical Society*, 213:325, 1997.

[34] K. Matyjaszewski, S. M. Jo, H. J. Paik, and S. G. Gaynor. Synthesis of well-defined polyacrylonitrile by atom transfer radical polymerization. *Macromolecules*, 30(20):6398–6400, 1997.

[35] K. Matyjaszewski, S. M. Jo, H. J. Paik, and D. A. Shipp. An investigation into the CuX/2,2 '-bipyridine (X = Br or Cl) mediated atom transfer radical polymerization of acrylonitrile. *Macromolecules*, 32(20):6431–6438, 1999.

[36] M. Lazzari, O. Chiantore, R. Mendichi, and M. A. Lopez-Quintela. Synthesis of polyacrylonitrile-block-polystyrene copolymers by atom transfer radical polymerization. *Macromolecular Chemistry and Physics*, 206(14):1382–1388, 2005.

[37] O. B. Ilhanli, T. Erdogan, U. Tunca, and G. Hizal. Acrylonitrile-containing polymers via a combination of metal-catalyzed living radical and nitroxide-mediated free-radical polymerization routes. *Journal of Polymer Science Part a-Polymer Chemistry*, 44(10):3374–3381, 2006.

[38] J. M. Leiston-Belanger, J. Penelle, and T. P. Russell. Synthesis and microphase separation of poly (styrene-b-acrylonitrile) prepared by sequential anionic and atrp techniques. *Macromolecules*, 39(5):1766–1770, 2006.

[39] H. C. Dong, W. Tang, and K. Matyjaszewski. Well-defined high-molecular-weight polyacrylonitrile via activators regenerated by electron transfer atrp. *Macromolecules*, 40(9):2974–2977, 2007.

[40] B. Dufour, C. B. Tang, K. Koynov, Y. Zhang, T. Pakula, and K. Matyjaszewski. Polar three-arm star block copolymer thermoplastic elastomers based on polyacrylonitrile. *Macromolecules*, 41(7):2451–2458, 2008.

[41] W. Tang and K. Matyjaszewski. Effects of initiator structure on activation rate constants in atrp. *Macromolecules*, 40(6):1858–1863, 2007.

[42] W. Tang and K. Matyjaszewski. Effect of ligand structure on activation rate constants in atrp. *Macromolecules*, 39(15):4953–4959, 2006.

[43] G. Wanka, H. Hoffmann, and W. Ulbricht. Phase-diagrams and aggregation behavior of poly(oxyethylene)-poly(oxypropylene)-poly(oxyethylene) triblock copolymers in aqueous-solutions. *Macromolecules*, 27(15):4145–4159, 1994.

[44] S. Peleshanko, J. Jeong, V. V. Shevchenko, K. L. Genson, Yu Pikus, M. Ornatska, S. Petrash, and V. V. Tsukruk. Synthesis and properties of asymmetric heteroarm peon-b-psm star polymers with end functionalities. *Macromolecules*, 37(20):7497, 2004.

[45] R. J. Hobson and A. H. Windle. Crystallization and shape emulation in atactic poly(vinyl chloride) and polyacrylonitrile. *Polymer*, 34(17):3582–3596, 1993.

[46] Bozhi Tian, Xiaoying Liu, Leonid A. Solovyov, Zheng Liu, Haifeng Yang, Zhendong Zhang, Songhai Xie, Fuqiang Zhang, Bo Tu, Chengzhong Yu, Osamu Terasaki, and Dongyuan Zhao. Facile synthesis and characterization of novel mesoporous and mesorelief oxides with gyroidal structures. *Journal of the American Chemical Society*, 126(3):865–875, 2003.

[47] G. J. Soler-Illia and C. Sanchez. Interactions between poly(ethylene oxide)-based surfactants and transition metal alkoxides: their role in the templated construction of mesostructured hybrid organic-inorganic composites. *New Journal of Chemistry*, 24(7):493–499, 2000.

[48] T. Kowalewski, N. V. Tsarevsky, and K. Matyjaszewski. Nanostructured carbon arrays from block copolymers of polyacrylonitrile. *Journal of the American Chemical Society*, 124(36):10632–10633, 2002.

[49] C. B. Tang, K. Qi, K. L. Wooley, K. Matyjaszewski, and T. Kowalewski. Well-defined carbon nanoparticles prepared from water-soluble shell cross-linked micelles that contain polyacrylonitrile cores. *Angewandte Chemie-International Edition*, 43(21):2783–2787, 2004.

[50] R. M. Ho, T. C. Wang, C. C. Lin, and T. L. Yu. Mesoporous carbons from poly(acrylonitrile)-b-poly(epsilon-caprolactone) block copolymers. *Macromolecules*, 40(8):2814–2821, 2007.

[51] M. Lazzari, D. Scalarone, C. E. Hoppe, C. Vazquez-Vazquez, and M. A. Lopez-Quintela. Tunable polyacrylonitrile-based micellar aggregates as a potential tool for the fabrication of carbon nanofibers. *Chemistry of Materials*, 19:5818–5820, 2007.

[52] C. Tang, B. Dufour, T. Kowalewski, and K. Matyjaszewski. Synthesis and morphology of molecular brushes with polyacrylonitrile block copolymer side chains and their conversion into nanostructured carbons. *Macromolecules*, 40(17):6199–6205, 2007.

[53] J. Brandup, E. H. Immergut, and E. A. Grulke. *Polymer Handbook.* John Wiley and Sons, 4th edition, 1999.

[54] A. Sadezky, H. Muckenhuber, H. Grothe, R. Niessner, and U. Poschl. Raman micro spectroscopy of soot and related carbonaceous materials: Spectral analysis and structural information. *Carbon*, 43(8):1731–1742, 2005.

[55] F. Tuinstra and J. L. Koenig. Raman spectrum of graphite. *Journal of Chemical Physics*, 53(3):1126, 1970.

[56] P. Lespade, R. Aljishi, and M. S. Dresselhaus. Model for raman-scattering from incompletely graphitized carbons. *Carbon*, 20(5):427–431, 1982.

[57] M. Kamperman, M. A. Fierke, C. B. W. Garcia, and U. Wiesner. Morphology control in block copolymer/polymer derived ceramic precursor nanocomposites. *Macromolecules*, 41(22):8745–8752, 2008.

[58] K. S. W. Sing, D. H. Everett, R. A. W. Haul, L. Moscou, R. A. Pierotti, J. Rouquerol, and T. Siemieniewska. Reporting physisorption data for gas solid systems with special reference to the determination of surface-area and porosity. *Pure and Applied Chemistry*, 57(4):603–619, 1985.

CHAPTER 4

ORDERED THREE- AND FIVE-PLY NANOCOMPOSITES FROM ABC BLOCK TERPOLYMER MICROPHASE SEPARATION WITH NIOBIA AND ALUMINOSILICATE SOLS[*]

4.1 Abstract

We report the first use of a non-frustrated block terpolymer for the synthesis of highly ordered oxide nanocomposites containing multiple plies. The morphological behavior of 15 ISO-oxide nanocomposites was investigated spanning a large range of compositions along the $f_I = f_S$ isopleth using aluminosilicate and niobia sols. Morphologies were determined by TEM and SAXS measurements. Four morphologies were identified, including core-shell hexagonal, core-shell double gyroid, three-domain lamellae, and core-shell inverse-hexagonal, in order of increasing O+oxide vol fraction. All of the resulting nanocomposites had three- or five-ply morphologies containing domains that were continuous in one, two, or three dimensions. The five-ply core-shell double gyroid phase was only found to be stable when the O+oxide domain was a minority. Removal of the polymer enabled simple and direct synthesis of mesoporous oxide materials while retaining the ordered network structure. We believe that advances in the synthesis of multi-ply nanocomposites will lead to advanced materials and devices containing multiple plies of functional materials.

4.2 Introduction

The microphase separation of amphiphilic block copolymers has been broadly applied toward structure-direction in numerous materials. Typically, the hydrophilic block is selectively swelled with hydrophilic particles via attractive intermolecular forces while the hydrophobic block is repelled. The balance of interface and chain stretching free energies lead the polymer to direct the co-assembly into various ordered morphologies. While such techniques have been extensively studied with diblock (AB)[1] and triblock (ABA) copolymers,[2,3] there are very few examples of triblock terpolymers (ABC) used as structure-directing agents.[4–6]

The application of triblock terpolymers as structure-directing agents is particularly interesting due to the dozens of known ordered morphologies of the neat polymers.[7–17] The plethora of network morphologies[18] is particularly interesting for use in devices, such as fuel cell, battery, or supercapacitor electrodes, which require multiple transport materials arranged in continuous pathways for fuel/electrolyte, ion conduction/storage, and electron transport. The network phases formed by triblock terpolymers are not only trifunctional, but also form over much wider phase composition window (4 to 14.1 vol%[14,19]) than the bifunctional double gyroid structure found in diblock copolymer systems (2 to 6 vol%[20,20]). Such a method of fabrication, where a sequence of three or more unique polymer blocks direct the spatial arrangement of multiple materials, thus defining the interfaces and pathways, is termed block sequence directed materials (BSDM).[21] The achievement of BSDMs would be a significant advance towards mimicking the complex assembly processes apparent in nature. In particular, ordered transition metal oxide materials are interesting in energy generation, storage, and conversion applications due to their ability to catalyze reactions, conduct ions, and intercalate ions.[22,23] Indeed it has already been shown that the three blocks of a terpolymer can be

designed to lead to trifunctional materials with control over each of the three final components.[21]

Morphology prediction of triblock terpolymer coassemblies is particularly complex due to the number of parameters. The phase behavior of ideal diblock copolymers may be predicted solely based on two parameters: the volume fraction f_a of the A block and the product χN of Flory-Huggins χ parameter with the overall degree of polymerization N. In contrast, the phase behavior of ideal triblock terpolymers is governed by five parameters: two independent volume fractions, f_a and f_b, and the products of three Flory-Huggins parameters, $\chi_{AB}N$, $\chi_{BC}N$, and $\chi_{AC}N$. The relative magnitude of each of the parameters further determines the types of morphologies formed. When χ_{AC} is the largest, the system is considered non-frustrated[24] and the large energetic penalty of A-C contacts leads to only core-shell and alternating versions of the morphologies found in diblock copolymers.[19] In contrast, frustrated block terpolymers are known to form decorated morphologies in which A-C interfaces are made to minimize A-B or B-C interfaces.[25] This morphological tendency was preserved when aluminosilicate structures were directed with such frustrated triblock terpolymers.[5,6]

The symmetry of the polymer blocks, or lack thereof, influences interfacial curvature. Symmetric and near symmetric diblock copolymers $(f_a \approx f_b)$ form lamellar morphologies whereas asymmetric diblock copolymers lead to morphologies with curved interfaces, including gyroid, hexagonal cylinders, and cubic micellar phases. Similarly, triblock terpolymer morphologies are influenced by both the A-B and B-C symmetries. Symmetric-symmetric ideal triblock terpolymers $(f_a = f_b =_c)$ form a 3-domain lamellar phase with flat interfaces whereas asymmetric-asymmetric triblock terpolymers $(f_a \neq f_b \neq_c)$ form numerous morphologies with curved interfaces. Combining both of these tendencies with a symmetric-asymmetric triblock
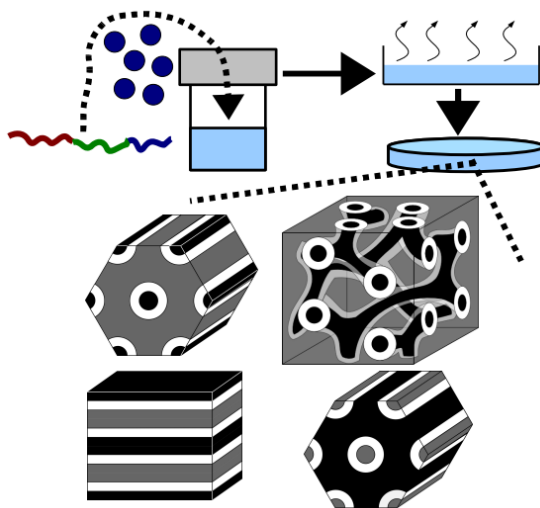
Figure 4.1: Schematic representation of "one-pot" synthesis of ordered multi-ply nanocomposites via evaporation induced coassembly of poly(isoprene-b-styrene-b-ethylene oxide) with oxide sols.

terpolymer ($f_a = f_b \neq_c$) can cause the competing interfacial forces to buckle the interface into periodic networks of saddle surfaces.[26]

Herein we present the results from the use of a non-frustrated, symmetric-asymmetric triblock terpolymer as a structure directing agent for oxide materials(Figure 4.1). To the best of our knowledge, this is the first report of ordered oxide materials structure-directed by a non-frustrated block terpolymer.

4.3 Experimental Methods

4.3.1 Materials

The poly(isoprene-b-styrene-b-ethylene oxide) (ISO) triblock terpolymers used here were prepared by sequential anionic polymerization and were thoroughly characterized previously.[14] ISO3 had a molecular weight of 15.24 kg/mol and a polydispersity of 1.05. ISO4 had a molecular weight of 15.78 kg/mol and a polydispersity of 1.05. The volume fractions of I, S, and O were calculated based on reported

homopolymer densities at 140 °C.[27] The volume fractions of I, S, and O in ISO3 were determined to be 0.448, 0.454, and 0.098, respectively. Similarly, ISO4 had volume fractions of 0.440, 0.435, and 0.125 for I, S, and O, respectively. The equilibrium morphologies of ISO3 and ISO4 were previously determined to be 2-domain lamellar and O^{70}, respectively.[14] The O^{70} is a tricontinuous orthorhombic network structure which was first identified in 2002 and has been detailed elsewhere.[14,18,26,28] ISO polymers are amphiphilic, having a hydrophilic O block and two hydrophobic blocks, I and S. The hydrophilic oxide sol particles are expected to selectively swell the O block.

4.3.2   Synthesis

Each aluminosilicate hybrid film was prepared from a 2.0-2.5 wt% polymer solution in THF-CHCl$_3$ (1:1 by volume) by adding a predetermined amount of aluminosilicate sol solution and casting the homogeneous mixture covered at 60 °C. The sol solution was prepared using a two step acid catalyzed hydrolysis procedure as described in detail elsewhere.[1,29] This sol is an organically modified ceramic (ORMOCER) which has much lower density than bulk silica.[1,30] The volume fraction of the combined O and aluminosilicate phase was calculated using a combined density of 1.4 g/cm^3 as thoroughly established previously.[5,6,31–34]

Each niobia hybrid film was prepared from a 0.3-0.8 wt% polymer solution in CHCl$_3$ by forming a non-hydrolytic sol in-situ, in a similar fashion to that previously described.[35] Specifically, niobium(V) ethoxide was added to the stirring polymer solution in a nitrogen glovebox. After 10 minutes of stirring, niobium(V) chloride was added in a 1.0:1.61 chloride:ethoxide molar ratio. The polymer-sol solution was stirred overnight at room temperature and cast in a teflon dish at 50 °C covered with a glass hemisphere. All films were subsequently placed in a

vacuum oven at 130 °C for at least one hour. The volume fraction of the O and niobia containing domain was calculated using densities of 1.064 and 2.0 g/cm^3, respectively. We believe that this is a reasonable estimate for the density of the amorphous niobia sol since metal oxide sol-gel densities are often less than half that of the bulk density.[36]

4.3.3   Equipment

Transmission Electron Microscopy (TEM)

Ultrathin sections were cut at -55 °C using a Leica Ultracut UCT microtome. The sections were transferred to copper grids and stained with aqueous 2 wt% OsO_4 solution or anhydrous OsO_4 vapor. Staining made the poly(isoprene) darker than poly(styrene). Bright field TEM was performed on a Tecnai T12 operating at 120 kV. The ISO polymer was removed from a sectioned sample by using a Fischione model 1020 Ar-O plasma cleaner. The 10 minute etching time combined with a ~1 nm/sec carbon etch rate was sufficient to remove all of the ISO from the c.a. 70 nm thick sections.

Small Angle X-ray Scattering (SAXS)

A Rigaku RU300 with a copper rotating anode (λ=1.54 Å) operated at 40 kV and 50 mA was used to gather SAXS data of the niobia containing samples. The X-rays were monochromated with a Ni filter and focused with orthogonal Franks mirrors. The 2D scattering patterns were collected with a homebuilt 1k x 1k pixel CCD detector similar to that described elsewhere.[37] SAXS data of the aluminosilicate containing samples were collected at the Cornell High Energy Synchrotron Source (CHESS), with a setup consisting of a multilayer monochromator (λ=1.457 Å) with a 2D area detector and a sample-to-detector distance of 1.61 m. Data are

presented as 1D plots of radially integrated intensity versus scattering vector q where $q=4\pi\sin(\theta)\lambda^{-1}$, where 2θ is the total scattering angle.

4.4 Results

4.4.1 Aluminosilicate Nanocomposites

Table 4.1: Compositions, Morphologies, and d-Spacing of ISO-Oxide Nanocomposites

film name	v % I	v % S	v % O + oxide	morphology	d $(nm)^a$	d $(nm)^b$
ISO3-S1	41.9%	42.4%	15.7%	worm	21.2	18
ISO3-S2	40.5%	41.0%	18.5%	CS-H	22.2	17
ISO3-S3	38.6%	39.1%	22.3%	CS-H	21.9	19
ISO3-S4	33.6%	34.1%	32.3%	CS-G^D(Lam$_3$)	54.6	62
ISO4-S1	42.7%	42.3%	15.0%	CS-H (worm)	19.9	19
ISO4-S2	41.6%	41.1%	17.3%	CS-H	21.7	19
ISO4-S3	38.7%	38.3%	23.0%	CS-G^D	52.9	63
ISO4-S4	35.2%	34.8%	30.0%	CS-G^D	56.2	53
ISO3-N1	18.6%	18.9%	62.5%	^{c}CS-iH	23.1	23
ISO3-N2	14.9%	15.1%	70.0%	^{c}CS-iH	21.6	20
ISO4-N1	28.3%	27.9%	43.8%	Lam$_3$	26.3	29
ISO4-N2	26.0%	25.7%	48.2%	Lam$_3$	24.0	22
ISO4-N3	24.6%	24.3%	51.1%	CS-iH	22.0	23
ISO4-N4	23.1%	22.9%	54.0%	CS-iH	24.8	23
ISO4-N5	21.1%	20.9%	58.0%	^{c}Lam$_3$	21.7	20

^{a} Lattice dimensions (d) are based on the lamellar (1), hexagonal (10), and gyroid (100) planes calculated from $d = 2\pi/q^*$. ^{b} Lattice dimension determined by TEM imaging. ^{c} Precipitation of inorganic species leads to a morphology with a lower effective volume fraction of PEO + oxide.

Our initial experiments targeted the orthorhombic O^{70} network phase. A previous study showed that neat ISO polymers along the $f_I = f_S$ isopleth form the O^{70} phase over a wide composition window spanning from 9.8 to 23.9 vol% of O.[14] We synthesized six nanocomposites within this window spanning from 15 to 23 vol% O+oxide. The stained TEM images of five of these nanocomposites ranging from 15.0 to 22.3 vol% O+oxide were characteristic of a core-shell hexagonal
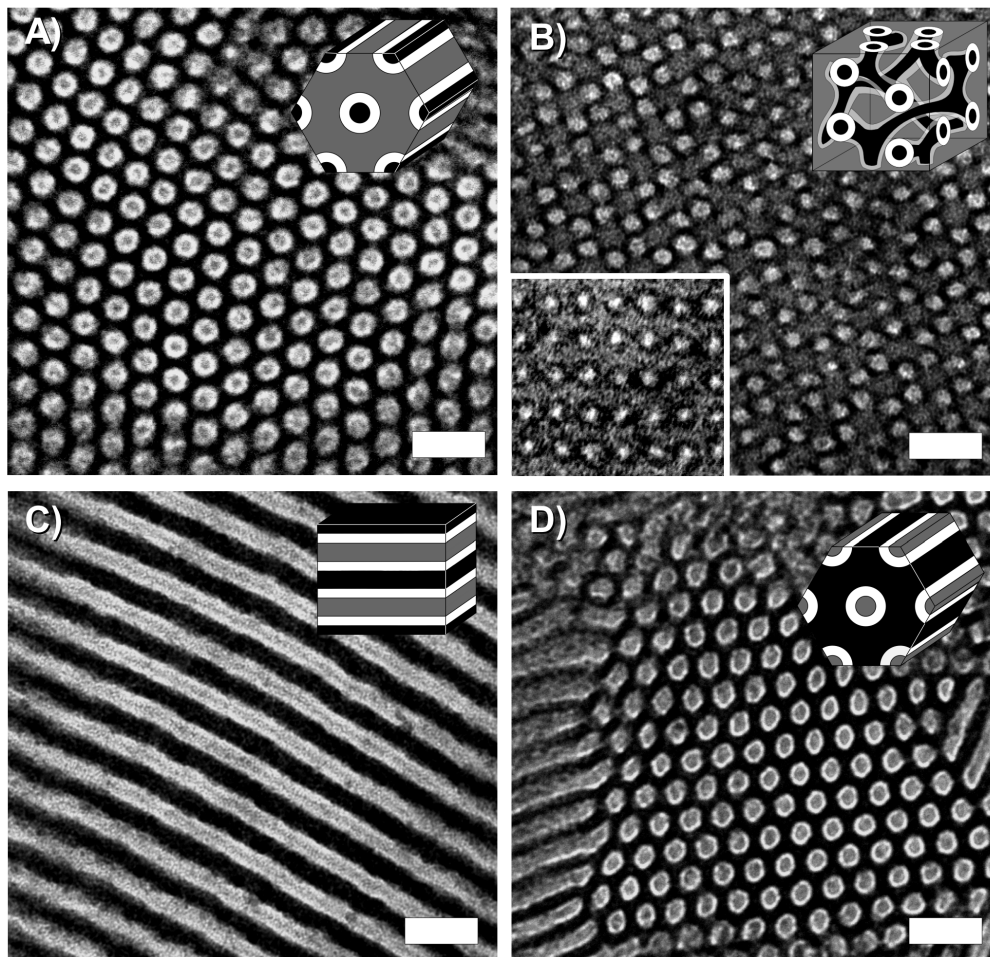
Figure 4.2: Representative TEM images of aluminosilicate nanocomposites with core-shell hexagonal (A) and core-shell double gyroid (B) morphologies (image and inset in B show a (111) and (100) projections, respectively). Also, representative TEM images of niobia nanocomposites with 3-domain lamellae (C) and core-shell inverse-hexagonal (D) morphologies. Light regions of these images correspond to poly(styrene) and dark regions correspond to either OsO_4 stained poly(isoprene) or oxide swelled poly(ethylene oxide). Polymer schematic (top) defines the colors used in the inset morphology schematics: gray, white, and black corresponding to I, S, and O+oxide domains respectively. Images shown at same scale with 50 nm scale bars inset. The representative TEM images above correspond to samples ISO3-S2, ISO4-S4, ISO4-N1, and ISO4-N3, respectively.
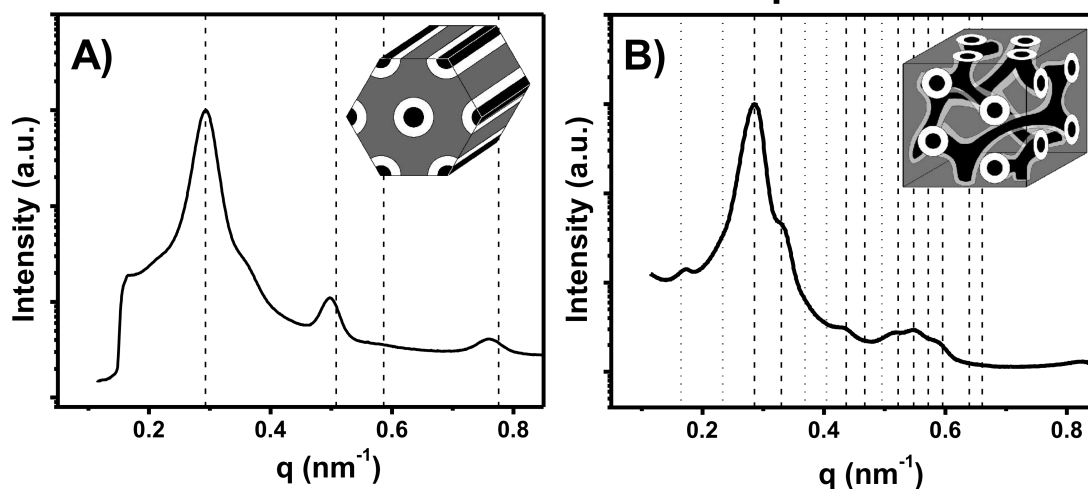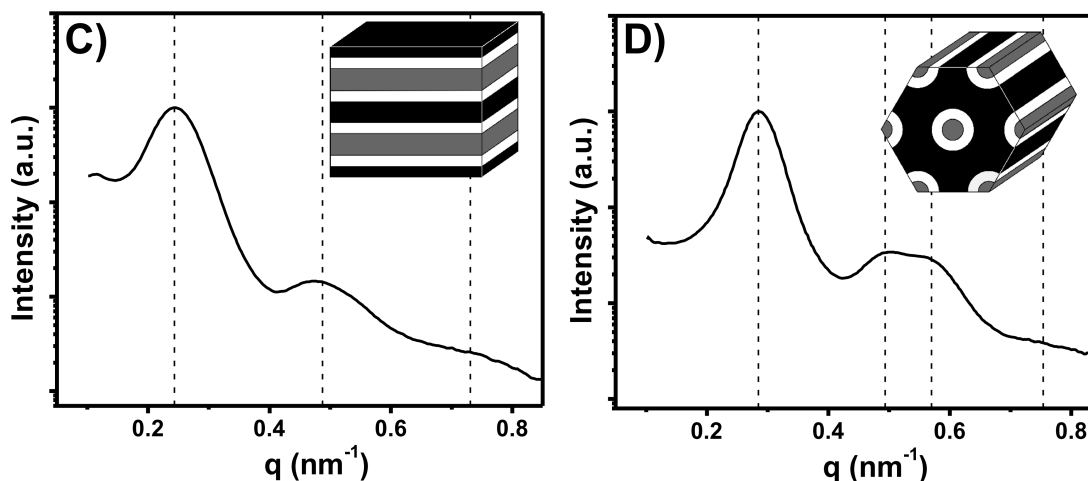
Figure 4.3: Representative SAXS patterns of aluminosilicate nanocomposites with core-shell hexagonal (A) and core-shell double gyroid (B) morphologies as well as niobia nanocomposites with 3-domain lamellae (C) and core-shell inverse-hexagonal (D) morphologies. The sequence of expected peaks was indicated in each spectrum (dashed lines). Normally forbidden-reflections which become allowed with unit cell compression (B) are additionally indicated (dotted lines). The patterns correspond to samples ISO4-S2, ISO4-S3, ISO4-N1, and ISO4-N3, respectively.

morphology (CS-H) containing O+oxide cores (gray) covered by a S shell (light) within an I matrix (dark) (Figure 4.2 A). The two samples with the least amount of oxide, ISO3-S1 and ISO4-S1, were primarily composed of short-range ordered worm-like structures, but ISO4-S1 also had some well-ordered CS-H regions. The SAXS patterns of these CS-H nanocomposites were also consistent with hexagonal symmetry, exhibiting characteristic peaks in the ratios defined as $(q/q^*)^2=1$, 3, and 7 (Figure 4.3 A). The d_{10} spacing for these series of samples varied from 19.9 to 22.2 nm and were consistent with the molecular weight of the ISO polymers as well as the observed c.a. 20 nm cylinder spacings in TEM (Table 4.1).

The three aluminosilicate samples with the highest O+oxide compositions all had similar phase behavior. TEM images of all three of these samples, ISO3-S4, ISO4-S3, and ISO4-S4, ranging from 23.0 to 32.3 vol% O+oxide exhibited core-shell wagon-wheel patterns with silicate cores (gray) surrounded by a S shell (light) within an I matrix (dark) which were characteristic of the (111) plane of the core-shell double gyroid (CS-G^D) morphology (Figure 4.2 B). The CS-G^D phase is a pentacontinuous structure with two separate core-shell gyroid networks of the same composition. Other TEM images of these samples were consistent with the (100) (Figure 4.2B inset) and (125) projections of the CS-G^D. The SAXS patterns of these samples were also consistent with the CS-G^D morphology exhibiting the strongest scattering at $(q/q^*)^2=6$ and 8. The scattering pattern closely matched the expected peaks which were indicated with dashed lines at $(q/q^*)^2=6$, 8, 14, 16, 20, 22, 24, 26, 30, and 32 (Figure 4.3 B). Samples ISO4-S3 and ISO4-S4 also exhibited a small peak corresponding to a forbidden reflection at $\sqrt{2}q^*$. Such forbidden reflections were also observed in previous cocontinuous cubic silica-type structures which were compressed in the z-direction leading to a breaking of the symmetry of the cubic phases.[22,31,38–40] The CS-G^D nanocomposites in this study

were all made by solvent casting which is well-known to compress films in the direction of evaporation. Detailed calculations by Toombes et al.[39] predicted the appearance of normally forbidden peaks at $(q/q^*)^2$=2, 4, 10, 12, and 18, depending on the nature of the G^D distortion (Figure 4.3 B, indicated with dotted lines). A 2D SAXS pattern of ISO4-S4 perpendicular to the evaporation direction showed 3.6-14.2% compression (varies from grain to grain) of the $\sqrt{6}q^*$ ring and is attributed to the appearance of the forbidden reflection at $\sqrt{2}q^*$. The d_{100} spacing determined by SAXS ranged from 52.9 to 56.2 nm and was consistent with the observed 53-63 nm spacings observed in TEM. The roughly twice as large lattice dimension, d, for CS-G^D relative to the CS-iH was due to the pentacontinuous nature of the CS-G^D morphology which has twice as many interfaces per unit cell: O-S-I-I-S-O-O-S-I-I-S-O compared to O-S-I-I-S-O. Thus the much larger lattice dimension d was still consistent with the molecular weight of the ISO polymers used. Sample ISO4-S4 with the largest amount of O+oxide fraction of 32.3 vol% had c.a. 20% three-domain lamellae (Lam$_3$) phase and is thus very close to Lam$_3$ phase space.

A free-standing mesoporous aluminosilicate double gyroid structure was synthesized by removing the ISO from sample ISO4-S4 using a reactive oxygen plasma. After ten minutes of etching the ISO was removed and the structure was preserved as evidenced by ordered network structures viewed on TEM (Figure 4.4). TEM observation of this sample revealed 5 to 11 nm diameter tubes of aluminosilicate with 3-fold nodes and 29 to 37 nm mesopores. The free-standing aluminosilicate structure was much more sensitive to the intensity of the incident electron bream than the nanocomposites and had to be imaged with a low intensity beam with very long CCD exposure times to limit the distortion of the structure. Furthermore, the lower contrast relative to (Figure 4.2 B) is due to the much lower atomic number of silicon as compared to osmium as well as the plasma treatment leading
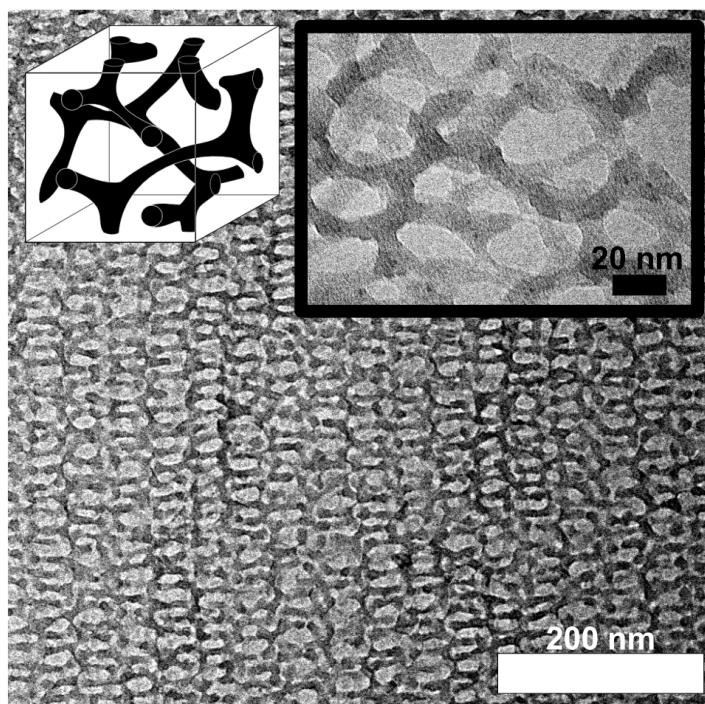
Figure 4.4: TEM image of free-standing mesoporous oxide double gyroid re-
sulting from oxygen plasma removal of ISO structure directing
agent from ISO4-S4. Schematic of the morphology (left inset) is
next to the high magnification TEM image (right inset).

to a much lower density than bulk aluminosilicates.

4.4.2   Niobia Nanocomposites

Seven additional samples were synthesized with a niobia sol in order to further explore the ISO-oxide phase diagram with the sol of a transition metal oxide. Samples spanned the $f_I = f_S$ isopleth from 43.8 to 70.0 vol% O+oxide.

Five of these niobia nanocomposites had volume fractions within the 27 to 62 vol% O range of the three-domain lamellae phase of neat ISO polymers along the $f_I = f_S$ isopleth.[28] Only two of the five samples with the lowest O+oxide volume fraction, ISO4-N1 and ISO4-N2, with O+oxide fractions ranging from 43.8 to 48.2 vol%, were identified to have the Lam_3 morphology by TEM and SAXS. The TEM images of these stained Lam_3 nanocomposites had layers of O+oxide (dark), S (light), and I (gray) arranged in patterns of ISO-OSI- which is characteristic of this morphology (Figure 4.2 C). The switching of O+oxide and stained I contrast in the niobia samples is due to the much higher atomic number of Nb (41) compared to Si (14) and Al (13). This resulted in the niobia providing more electron scattering contrast than the OsO_4 stained I. The SAXS patterns of these two samples have peaks consistent with lamellar symmetry, with peaks at $(q/q^*)^2$=1, 4, and 9 (Figure 4.3 C). The d_1 lattice spacing measured by SAXS varied from 24.0 to 26.3 nm and was consistent with both the observed c.a. 25 nm spacings observed in TEM and the molecular weight of the ISO polymer.

Niobia nanocomposites with O+oxide fractions beyond 50.0 vol% were found to form a different morphology. Neat ISO polymers are known to form core-shell double gyroid ($I a \bar{3} d$) and core-shell hexagonal phases in narrow composition windows on the O-rich side of the ISO phase diagram.[28] Samples ISO4-N3 and ISO4-N4 had O+oxide fractions of 51.1 and 54.0 vol%, respectively, and both
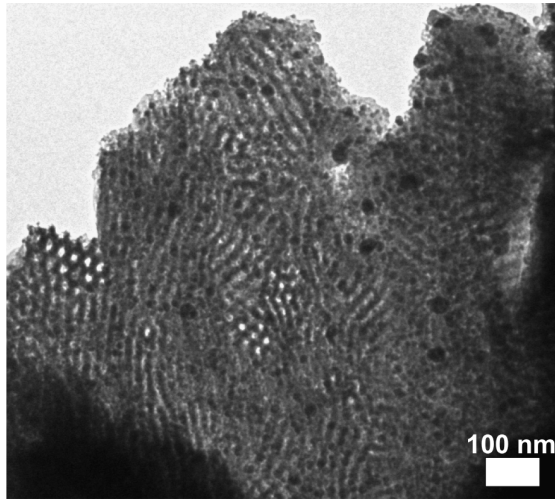
Figure 4.5: Representative TEM image of sample ISO3-N2 showing macrophase separation of niobia precipitates at high oxide loadings (>58 vol% O+oxide).

formed the same morphology. TEM images of these samples showed a hexagonal arrangement of continuous tubes of I (gray) covered with shells of S (white) within a matrix of O+oxide (dark) (Figure 4.2 D). Although this image is similar to the aluminosilicate core-shell hexagonal image (compare Figure 4.2 A and 4.2 D), the I and O+oxide domains have switched places. Accordingly, this morphology is named core-shell inverse-hexagonal (CS-iH) since the O+oxide domain forms the matrix. The SAXS patterns of these two samples were also consistent with the observed hexagonal symmetry, showing scattering peaks at $(q/q^*)^2 = 1$, 3, and 4 (Figure 4.3 D). The d_{10} spacing varied from 22.0 and 24.8 nm and was consistent with c.a. 23 nm spacings observed in TEM as well as the molecular weight of the ISO polymer used.

The niobia nanocomposites synthesized with 58 vol% O+oxide or more had macrophase separated regions of niobia. Samples ISO4-N5, ISO3-N1, and ISO3-N2 all had clear formation of precipitates throughout the films when viewed on the TEM (Figure 4.5). The precipitation of some of the niobia sol from solution
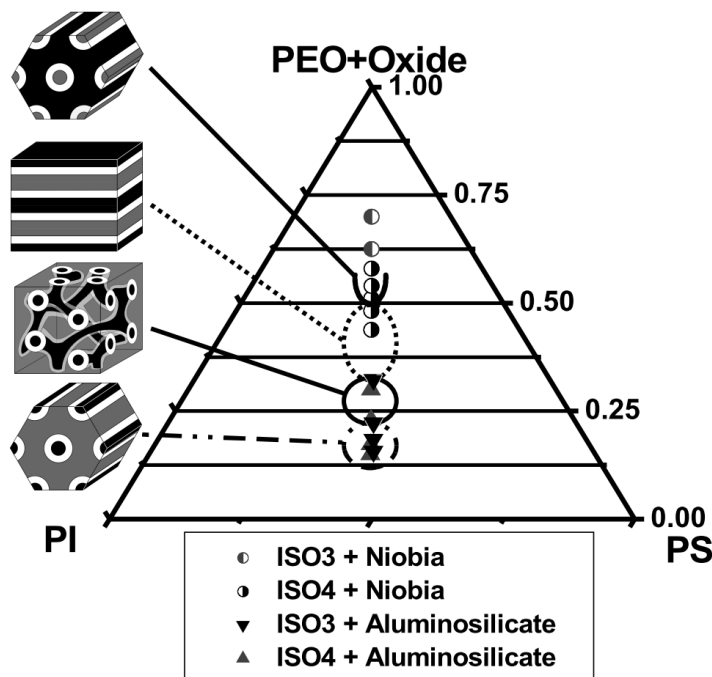
Figure 4.6: Morphology map for poly(isoprene-*b*-styrene-*b*-ethylene oxide) nanocomposites with axes indicating the volume fractions of I, S, and O+oxide. Symbols identify the polymer and oxide used. Four ordered morphologies were identified, including core-shell hexagonal, core-shell double gyroid, 3-domain lamellae, and core-shell inverse-hexagonal. The three samples with the highest O+oxide fractions had oxide precipitation from the polymer which lead to lower effective O+oxide volume fractions.

leads to a lower effective volume fraction of niobia mixed with O block of the polymer. This is likely why ISO4-N5 with 58 vol% O+oxide exhibited a Lam_3 morphology predominantly in TEM and SAXS. Samples ISO3-N1 and ISO3-N2 also had clear macrophase separation, but still had the expected CS-iH morphology. The macrophase separation correlated to a decrease in d_{10} in the ordered regions relative to samples of similar composition (Table 4.1).

4.5 Discussion

The morphology results of 15 oxide nanocomposites structure-directed with 2 different ISO triblock terpolymers along the $f_I = f_S$ isopleth are displayed in Figure 4.6. Due to the many parameters of this phase space, the two-dimensional ternary phase diagram represents a small slice of the complete phase space along this isopleth. In particular, the molecular weight (N), and volume fraction of O (f_O) were only varied within a narrow range. Furthermore, this morphology map is a composite containing results from both aluminosilicate and niobia nanocomposites. Each morphology is discussed separately before the overall phase behavior of this isopleth is discussed.

4.5.1 Core-Shell Hexagonal Phase

The core-shell hexagonal phase was found to form in the composition window from 15.0 to 22.3 vol% O+oxide. This contrasts sharply from neat ISO which forms the O^{70} phase from 9.8 to 23.9 vol% O along the same isopleth. This CS-H phase was even observed when ISO4 (forms O^{70} when neat) was mixed with just 2.9 vol% aluminosilicate (ISO4-S1). Clearly, the system thermodynamics were strongly affected by the selective mixing of sol particles with the O domain. A similar suppression of the O^{70} phase was observed when relatively small amounts of lithium perchlorate were mixed with similar ISO polymers.[4] The marked change in phase behavior was attributed to the 17-fold increase in segregation strength induced by the selective dissolution of lithium perchlorate into the O blocks. An analagous effect is likely at play in the ISO-oxide system. The effect of the addition of oxide nanoparticles on the segregation strength of ISO was crudely estimated[41] by comparing the $d^*(\equiv 2\pi/q^*)$ spacing of hexagonal ISO3 to that of ISO3-S2 using $d^* \propto \chi^{1/6}$. This approximation lead to an estimated increase in χ by a factor

of 1.8 upon addition of oxide sol. While addition of oxide sol to ISO does not increase nearly as much as lithium perchlorate, it is still sufficient to explain the similar change in phase behavior. The CS-H phase was not only found at very low oxide loadings, but also into the dense nanoparticle regime.[42] Sample ISO3-S3 formed the CS-H phase with an aluminosilicate volume fraction larger than the O vol fraction. The CS-H phase was stabilized by the increased segregation strength induced by very small amounts of oxide and was preserved into the dense nanoparticle regime.

4.5.2   Core-Shell Double Gyroid Phase

The core-shell double gyroid morphology was found with O+oxide volume fractions ranging from 23.0 to 32.3 vol%. This large 9.3 vol% O+oxide window is comparable to the 14.1 vol% O window for the O^{70} phase in neat ISO polymers along the same isopleth. From a synthetic standpoint, this wide phase window with ISO structure-directing agents makes the fabrication of materials with tri-functional network structures far easier than with diblock copolymers.[31] The existence of this network structure in the ISO-oxide system was quite unexpected considering the suppression of all network phases when similar ISO polymers were selectively swelled with lithium salts.[4] In this case, the less drastic increase in segregation strength for the ISO-oxide system likely leads to the replacement of O^{70} with CS-G^D rather than the complete suppression of network phases.

4.5.3   Three-domain Lamellae Phase

The Lam_3 phase was found with O+oxide fractions ranging from about 32.3 to 48.2 vol%. The Lam_3 phase window for ISO-oxide is more narrow than that of neat ISO polymers (27 to 62 vol% O), but occurs over a similar region of the

$f_I = f_S$ isopleth. The considerable asymmetry of the phase boundaries about the $f_I = f_S = f_O = 1/3$ symmetric point is due to the asymmetry of the I, S, and O mer units as well as the asymmetry of the χ parameters[19,43] which was exaggerated by the addition of oxide sols.

4.5.4   Core-Shell Inverse-Hexagonal Phase

The core-shell inverse-hexagonal morphology was found when the O+oxide composition was between 51 and 54 vol%. Larger O+oxide fractions could be explored by starting with ISO polymers with larger O fractions or perhaps by modifying the niobia sol-gel process. However, such searches towards the O+oxide rich corner of the phase diagram are likely to result in isolated micellar phases or disordered mixing. The onset of the CS-iH at 51 vol% O+oxide is considerably lower than that predicted for neat ISO polymers (c.a. 70 to 80 vol% O)[19] and is likely due to the increased segregation strength of the O+oxide domain. It is impressive to note how well the ISO-oxide system behaves deep into the dense nanoparticle regime. For example, ISO4-N4 with 54 vol% O+oxide contained 7.2 times more volume of oxide than O yet still formed a highly ordered morphology. All samples targeting O+oxide fractions higher than 54 vol% resulted in macrophase separation of niobia precipitates (ISO3-N1, ISO3-N2, and ISO4-N5). The isolated precipitates of niobia resulted in a lower effective O+oxide volume fraction. This lower effective O+oxide fraction led ISO4-N5 to form a Lam$_3$ phase even though the recipe targeted an O+oxide region of phase space near CS-iH. This lower effective O+oxide fraction was further evidenced in SAXS by a shift to smaller d* spacings (compare ISO4-N4 to ISO4-N5 and ISO3-N1 to ISO3-N2).

4.5.5 Phases Encountered

The phase behavior observed in the ISO-oxide system was characteristic of the non-frustrated ISO polymers used. All of the observed phases CS-H, CS-G^D, Lam$_3$, and CS-iH exhibited only A-B and B-C type interfaces without any A-C type contacts. The four observed phases were all core-shell analogs of the lamellar, double gyroid, and hexagonal phases common to diblock copolymers and appeared in same sequence. The very different phase space of the ISO-oxide system relative to neat ISO is attributed to the change in system thermodynamics which was evidenced even at very low oxide loadings.

The network morphology observed in the ISO-oxide system differed substantially from neat ISO. Along the $f_I = f_S$ isopleth neat ISO polymers form the orthorhombic O^{70} phase on the O minority side of the isopleth from 9.8 to 23.9 vol% O and the cubic core-shell double gyroid on the O majority side of the isopleth from 61 to 67 vol% O.[28] In contrast, the ISO-oxide system differed in two regards: 1) the cubic core-shell double gyroid structure formed on the O+oxide minority side of the isopleth and 2) no network phases were found on the O+oxide majority side of the isopleth. The appearance of the CS-G^D phase on the O+oxide minority side of the isopleth, 1), can be rationalized by a slight distortion of neat ISO phase boundries[19] by extending the CS-G^D phase space slightly towards the I corner of the ternary phase diagram. The change in ISO thermodynamics with the addition of oxide sol could be attributed to such a shift. As predicted for neat ISO, the symmetric-asymmetric ISO structure-directing agents lead to an ISO-oxide network structure with saddle surfaces.[26] In contrast the lack of any observed network structures on the O+oxide majority side of the isopleth, 2), requires further discussion. Although the existence of an ISO-oxide network phase on the O+oxide majority side of the isopleth cannot be disproved, it is not expected

for the polymers used in this study since no such phases were observed as minority phases in samples ISO4-N2 or ISO4-N3 near the transition from Lam_3 to CS-iH. We suspect that O+oxide majority network phases are suppressed by the entropic penalty associated with the O chain stretching necessary to reach the center of each node. This effect was likely exacerbated by the relatively small O fraction of the ISO polymers used in this study as well as the increased unit cell size at high oxide loadings. For comparison, such O+oxide majority network phases for IO diblock copolymers are know to form under a narrow set of conditions including a larger 32 vol% O.[31,39] Furthermore, the stability of ISO-oxide network phases may be rationalized in terms of the increased polydispersity of the combined O+oxide domain. Copolymers with blocks of different polydispersity are known to favor structures with surfaces curving towards the block of higher dispersity.[44–47] Thus the stability of O+oxide minority network phases is expected to be higher than that of O+oxide majority network phases. There is likely a narrow set of conditions under which the ISO-oxide system forms network phases on the O+oxide majority side of the $f_I = f_S$ isopleth, however, we don't expect these conditions to be as experimentally tractable as when O+oxide is a minority.

4.5.6 Outlook for Applications

The reported CS-H, CS-G^D, Lam_3, and CS-iH morphologies could be useful for applications requiring continuous paths of multiple functional materials. The core-shell hexagonal morphologies contain a continuous matrix with two minority components that are continuous in one dimension whereas the Lam_3 phase has all three components continuous in two dimensions. In contrast, the CS-G^D morphology has a pentacontinuous structure with all five-plies continuous in all directions. A series of selective domain transformations[48–50] could be used to convert the ma-

terials reported here into nanocomposites containing multiple function materials with either anisotropic or isotropic continuity. Such materials could be useful for advanced applications including photonic materials as well as energy generation, conversion, and storage devices.

Furthermore, ordered materials with continuous porosity are of interest for filtration, electronic, and optical applications. Towards this end we demonstrated a free-standing mesoporous aluminosilicate double gyroid (Figure 4.4). Such materials could be directly used as orientation independent filters. Alternatively, these free-standing oxide networks could be used as sacrificial hard templates for the synthesis of mesoporous, crystalline transition metal oxides.[51] Similarly, these oxide networks could also be used as substrates for the deposition of layers of functional materials for 3-dimensionally continuous electronic and optical devices.

4.6 Conclusions

The results of 15 ISO-oxide nanocomposites were detailed along the $f_I = f_S$ isopleth using aluminosilicate and niobia sols. Four morphologies were identified, including core-shell hexagonal, core-shell double gyroid, three-domain lamellae, and core-shell inverse-hexagonal. These three- and five-ply nanocomposites contained continuous domains spanning in either one, two, or three dimensions. We believe that this approach will lead to advanced materials and devices containing several plies of functional materials.

4.7 Acknowledgements

REFERENCES

[1] M. Templin, A. Franck, A. DuChesne, H. Leist, Y. M. Zhang, R. Ulrich, V. Schadler, and U. Wiesner. Organically modified aluminosilicate mesostructures from block copolymer phases. *Science*, 278(5344):1795–1798, 1997.

[2] P. D. Yang, D. Y. Zhao, D. I. Margolese, B. F. Chmelka, and G. D. Stucky. Generalized syntheses of large-pore mesoporous metal oxides with semicrystalline frameworks. *Nature*, 396(6707):152–155, 1998.

[3] D. Y. Zhao, J. L. Feng, Q. S. Huo, N. Melosh, G. H. Fredrickson, B. F. Chmelka, and G. D. Stucky. Triblock copolymer syntheses of mesoporous silica with periodic 50 to 300 angstrom pores. *Science*, 279(5350):548–552, 1998.

[4] T. H. Epps, T. S. Bailey, R. Waletzko, and F. S. Bates. Phase behavior and block sequence effects in lithium perchlorate-doped poly(isoprene-b-styrene-b-ethylene oxide) and poly(styrene-b-isoprene-b-ethylene oxide) triblock copolymers. *Macromolecules*, 36(8):2873–2881, 2003.

[5] G. E. S. Toombes, S. Mahajan, M. Thomas, P. Du, M. W. Tate, S. M. Gruner, and U. Wiesner. Hexagonally patterned lamellar morphology in abc triblock copolymer/aluminosilicate nanocomposites. *Chemistry of Materials*, 20(10):3278–3287, 2008.

[6] G. E. S. Toombes, S. Mahajan, M. Weyland, A. Jain, P. Du, M. Kamperman, S. M. Gruner, D. A. Muller, and U. Wiesner. Self-assembly of four-layer woodpile structure from zigzag abc copolymer/aluminosilicate concertinas. *Macromolecules*, 41(3):852–859, 2008.

[7] Y. Mogi, H. Kotsuji, Y. Kaneko, K. Mori, Y. Matsushita, and I. Noda. Preparation and morphology of triblock copolymers of the abc type. *Macromolecules*, 25(20):5408–5411, 1992.

[8] C. Auschra and R. Stadler. New ordered morphologies in abc triblock copolymers. *Macromolecules*, 26(9):2171–2174, 1993.

[9] U. Krappe, R. Stadler, and I. Voigtmartin. Chiral assembly in amorphous abc triblock copolymers - formation of a helical morphology in polystyrene-block-polybutadiene-block-poly(methyl methacrylate) block-copolymers. *Macromolecules*, 28(13):4558–4561, 1995.

[10] W. Zheng and Z.-G. Wang. Morphology of abc triblock copolymers. *Macromolecules*, 28(21):7215–7223, 1995.

[11] Y. Matsushita, J. Suzuki, and M. Seki. Surfaces of tricontinuous structure formed by an abc triblock copolymer in bulk, 1998.

[12] T. A. Shefelbine, M. E. Vigild, M. W. Matsen, D. A. Hajduk, M. A. Hillmyer, E. L. Cussler, and F. S. Bates. Core-shell gyroid morphology in a poly(isoprene-block-styrene-block-dimethylsiloxane) triblock copolymer. *Journal of the American Chemical Society*, 121(37):8457–8465, 1999.

[13] F. S. Bates and G. H. Fredrickson. Block copolymers - designer soft materials. *Physics Today*, 52(2):32–38, 1999.

[14] T. S. Bailey, C. M. Hardy, T. H. Epps, and F. S. Bates. A noncubic triply periodic network morphology in poly(isoprene-b-styrene-b-ethylene oxide) triblock copolymers. *Macromolecules*, 35(18):7007–7017, 2002.

[15] S. Ludwigs, A. Boker, V. Abetz, A. H. E. Muller, and G. Krausch. Phase behavior of linear poly styrene-block-poly (2-vinylpyridine)-block-poly(tert-butyl methacrylate) triblock terpolymers. *Polymer*, 44(22):6815–6823, 2003.

[16] A. Walther, A. Goldel, and A. H. E. Muller. Controlled crosslinking of polybutadiene containing block terpolymer bulk structures: A facile way towards complex and functional nanostructures. *Polymer*, 49(15):3217–3227, 2008.

[17] H. Jinnai, T. Kaneko, K. Matsunaga, C. Abetz, and V. Abetz. A double helical structure formed from an amorphous, achiral abc triblock terpolymer. *Soft Matter*, 5(10):2042–2046, 2009.

[18] F. S. Bates. Network phases in block copolymer melts. *Mrs Bulletin*, 30(7):525–532, 2005.

[19] C. A. Tyler, J. Qin, F. S. Bates, and D. C. Morse. SCFT study of nonfrustrated abc triblock copolymer melts. *Macromolecules*, 40(13):4654–4668, 2007.

[20] G. Floudas, R. Ulrich, and U. Wiesner. Microphase separation in poly(isoprene-b-ethylene oxide) diblock copolymer melts. *Journal of Chemical Physics*, 110(1):652–663, 1999.

[21] M. Stefik, H. Sai, K. Sauer, S. M. Gruner, F. J. DiSalvo, and U. Wiesner. Three-component porous-carbon-titania nanocomposites through self-assembly of abcba block terpolymers with titania sols. *Macromolecules*, 42(17):6682–6687, 2009.

[22] E. J. W. Crossland, M. Kamperman, M. Nedelcu, C. Ducati, U. Wiesner, D. M. Smilgies, G. E. S. Toombes, M. A. Hillmyer, S. Ludwigs, U. Steiner, and H. J. Snaith. A bicontinuous double gyroid hybrid solar cell. *Nano Letters*, 2008.

[23] M. Stefik, J. Lee, and U. Wiesner. Nanostructured carbon-crystalline titania composites from microphase separation of poly(ethylene oxide-b-acrylonitrile) and titania sols. *Chemical Communications*, (18):2532–2534, 2009.

[24] T. S. Bailey. *Morphological behavior spanning the symmetric ab and abc block copolymer states*. PhD thesis, University of Minnesota, 2001.

[25] T. S. Bailey, H. D. Pham, and F. S. Bates. Morphological behavior bridging the symmetric ab and abc states in the poly(styrene-b-isoprene-b-ethylene oxide) triblock copolymer system. *Macromolecules*, 34(20):6994–7008, 2001.

[26] T. H. Epps, E. W. Cochran, T. S. Bailey, R. S. Waletzko, C. M. Hardy, and F. S. Bates. Ordered network phases in linear poly(isoprene-b-styrene-b-ethylene oxide) triblock copolymers. *Macromolecules*, 37(22):8325–8341, 2004.

[27] L. J. Fetters, D. J. Lohse, D. Richter, T. A. Witten, and A. Zirkel. Connection between polymer molecular-weight, density, chain dimensions, and melt viscoelastoc properties. *Macromolecules*, 27(17):4639–4647, 1994.

[28] J. Chatterjee, S. Jain, and F. S. Bates. Comprehensive phase behavior of poly(isoprene-b-styrene-b-ethylene oxide) triblock copolymers. *Macromolecules*, 40(8):2882–2896, 2007.

[29] S. C. Warren, F. J. Disalvo, and U. Wiesner. Nanoparticle-tuned assembly and disassembly of mesostructured silica hybrids. *Nature Materials*, 6(3):248–248, 2007.

[30] P. F. W. Simon, R. Ulrich, H. W. Spiess, and U. Wiesner. Block copolymer-ceramic hybrid materials from organically modified ceramic precursors. *Chemistry of Materials*, 13(10):3464–3486, 2001.

[31] A. C. Finnefrock, R. Ulrich, G. E. S. Toombes, S. M. Gruner, and U. Wiesner. The plumber's nightmare: A new morphology in block copolymer-ceramic nanocomposites and mesoporous aluminosilicates. *Journal of the American Chemical Society*, 125(43):13084–13093, 2003.

[32] A. Jain, G. E. S. Toombes, L. M. Hall, S. Mahajan, C. B. W. Garcia, W. Probst, S. M. Gruner, and U. Wiesner. Direct access to bicontinuous skeletal inorganic plumber's nightmare networks from block copolymers. *Angewandte Chemie-International Edition*, 44(8):1226–1229, 2005.

[33] A. Jain, L. M. Hall, C. B. W. Garcia, S. M. Gruner, and U. Wiesner. Flow-induced alignment of block copolymer-sol nanoparticle coassemblies toward oriented bulk polymer-silica hybrids. *Macromolecules*, 38(24):10095–10100, 2005.

[34] B. K. Cho, A. Jain, S. M. Gruner, and U. Wiesner. Nanoparticle-induced packing transition in mesostructured block dendron-silica hybrids. *Chemistry of Materials*, 19(15):3611–3614, 2007.

[35] J. Lee, M. C. Orilall, S. C. Warren, M. Kamperman, F. J. Disalvo, and U. Wiesner. Direct access to thermally stable and highly crystalline mesoporous transition-metal oxides with uniform pores. *Nature Materials*, 7(3):222–228, 2008.

[36] P. C. A. Alberius, K. L. Frindell, R. C. Hayward, E. J. Kramer, G. D. Stucky, and B. F. Chmelka. General predictive syntheses of cubic, hexagonal, and lamellar silica and titania mesostructured thin films. *Chemistry of Materials*, 14(8):3284–3294, 2002.

[37] M. W. Tate, E. F. Eikenberry, S. L. Barna, M. E. Wall, J. L. Lowrance, and S. M. Gruner. A large-format high-resolution area x-ray-detector based on a fiberoptically bonded charge-coupled-device (ccd). *Journal of Applied Crystallography*, 28:196–205, 1995.

[38] M. Klotz, P. A. Albouy, A. Ayral, C. Menager, D. Grosso, A. Van der Lee, V. Cabuil, F. Babonneau, and C. Guizard. The true structure of hexagonal mesophase-templated silica films as revealed by x-ray scattering: Effects of thermal treatments and of nanoparticle seeding. *Chemistry of Materials*, 12(6):1721–1728, 2000.

[39] G. E. S. Toombes, A. C. Finnefrock, M. W. Tate, R. Ulrich, U. Wiesner, and S. M. Gruner. A re-evaluation of the morphology of a bicontinuous block copolymer-ceramic material. *Macromolecules*, 40(25):8974–8982, 2007.

[40] V. N. Urade, T.-C. Wei, M. P. Tate, J. D. Kowalski, and H. W. Hillhouse. Nanofabrication of double-gyroid thin films. *Chemistry of Materials*, 19(4):768–777, 2007.

[41] A. N. Semenov. Microphase separation in diblock-copolymer melts: Ordering of micelles. *Macromolecules*, 22(6):2849–2851, 2002.

[42] A. Jain and U. Wiesner. Silica-type mesostructures from block copolymer phases: Formation mechanism and generalization to the dense nanoparticle regime. *Macromolecules*, 37(15):5665–5670, 2004.

[43] G. Floudas, B. Vazaiou, F. Schipper, R. Ulrich, U. Wiesner, H. Iatrou, and N. Hadjichristidis. Poly(ethylene oxide-b-isoprene) diblock copolymer phase diagram. *Macromolecules*, 34(9):2947–2957, 2001.

[44] N. A. Lynd and M. A. Hillmyer. Influence of polydispersity on the self-assembly of diblock copolymers. *Macromolecules*, 38(21):8803–8810, 2005.

[45] D. M. Cooke and A. C. Shi. Effects of polydispersity on phase behavior of diblock copolymers. *Macromolecules*, 39(19):6661–6671, 2006.

[46] A. V. Ruzette, S. Tence-Girault, L. Leibler, F. Chauvin, D. Bertin, O. Guerret, and P. Gerard. Molecular disorder and mesoscopic order in polydisperse acrylic block copolymers prepared by controlled radical polymerization. *Macromolecules*, 39(17):5804–5814, 2006.

[47] A. J. Meuler, C. J. Ellison, J. Qin, C. M. Evans, M. A. Hillmyer, and F. S. Bates. Polydispersity effects in poly(isoprene-b-styrene-b-ethylene oxide) triblock terpolymers. *Journal of Chemical Physics*, 130(23), 2009.

[48] M. A. Hillmyer. *Nanoporous materials from block copolymer precursors*, volume 190. Springer, 2005.

[49] R. Ryoo, S. H. Joo, and S. Jun. Synthesis of highly ordered carbon molecular sieves via template-mediated structural transformation. *Journal of Physical Chemistry B*, 103(37):7743–7746, 1999.

[50] J. Lee, S. Yoon, T. Hyeon, S. M. Oh, and K. B. Kim. Synthesis of a new mesoporous carbon and its application to electrochemical double-layer capacitors. *Chemical Communications*, (21):2177–2178, 1999.

[51] B. Tian, X. Liu, L. A. Solovyov, Z. Liu, H. Yang, Z. Zhang, S. Xie, F. Zhang, B. Tu, C. Yu, O. Terasaki, and D. Zhao. Facile synthesis and characterization of novel mesoporous and mesorelief oxides with gyroidal structures. *Journal of the American Chemical Society*, 126(3):865–875, 2003.

CHAPTER 5

CHIRAL AND NETWORKED NANOCOMPOSITES FROM ABC TRIBLOCK TERPOLYMER COASSEMBLY WITH TRANSITION METAL OXIDE NANOPARTICLES[*]

5.1 Abstract

Multicomponent materials with ordered nanoscale structures are critical for applications ranging from microelectronics to energy conversion and storage. Nanoscale network morphologies are ideal for many such applications requiring charge transport along multiple 3D continuous pathways. Similarly, non-centrosymmetric morphologies facilitate macroscopic polarization for piezoelectricic, pyroelectric, and second-order nonlinear optical properties in amorphous materials. Although the alternating gyroid (G^A, $I4_132$ space group) morphology poseses all of these characteristics, the coassembly of such nanomaterials has eluded researchers. Here we report the coassembly of niobia nanoparticles with a poly(isoprene-b-styrene-b-ethylene oxide) (ISO) which resulted in chiral and networked nanocomposites. Detailed SAXS and TEM measurements of both pure ISO and the nanocomposites were most consistent with the G^A. Electron tomographic reconstructions of the nanocomposites enabled observation of the chiral spirals as well as the oxide nanoparticle spatial distribution. Removal of the ISO polymer from these nanocomposites resulted in a mesoporous single gyroid strut network. These are the first reports of nanocomposites and mesoporous oxides with $I4_132$ symmetry derived directly from block copolymer coassembly. This general approach was further demonstrated with amorphous and anatase titania. Such procedures are compatible with large-scale manufacturing of networked nanoscale devices and

photonic metamaterials utilizing the G^A helical axes.

5.2 Introduction

Although there is considerable interest in both networked[1] and non-centrosymmetric[2] nanomaterials, there are few approaches which are compatible with the large-scale, affordable fabrication necessary to have a significant impact. Bottom-up fabrication techniques, such as block copolymer self-assembly enable large-scale processing via casting or roll-to-roll processes, for example. The demixing of covalently linked polymer blocks into ordered nanoscale morphologies is well understood.[3,4] The double gyroid (G^D) is a particularly appealing morphology which is cubic and networked with all of the blocks forming 3D continuous pathways. The most studied polymer architecture is the AB diblock copolymer, however this class of polymers is generally limited to spherical, cylindrical, double gyroid, or lamellar morphologies, all of which are achiral and centrosymmetric.

Use of ABC triblock terpolymers rather than AB diblocks significantly increases the number of accessible ordered nanostructures and at the same time provides a natural path to three-component nanocomposites. Furthermore the network phases formed by triblock terpolymers are not only trifunctional, but also form over much wider composition windows (4 to 14 vol%[5,6]) than the double gyroid structure found in diblock copolymers (2 to 6 vol%[7,8]). For example an ABC triblock terpolymer (containing three chemically unique mer units) was shown to form the alternating gyroid morphology where each of the two minority end blocks formed a 3D continuous strut network which were separated by a continuous matrix of the middle block.[9] The G^A not only has three networked compartments, but also has chiral spirals along six axes within each strut network and is non-centrosymmetric, unlike the double gyroid which is achiral due to the inversion

center ($I\bar{a}\bar{3}d$ space group). Non-centrosymmetric morphologies have been made by self-assembly of triblock terpolymers in selective solvents[10] or in the presence of a diblock copolymer,[2] however the resulting non-networked morphologies were uniaxial and would suffer from pronounced direction dependent properties.[11] Chiral nanostructures have also recently been obtained from diblock copolymers in confinement[12] or with a chiral block.[13]

The addition of inorganic species to polymers often enhances the physical and chemical properties.[14,15] Coassembly processes utilizing the selective interactions of amphiphilic block copolymers with inorganic particles have been broadly applied toward structure directing of numerous materials resulting in e.g. highly ordered silicate,[16,17] transition metal oxide,[18] and metal[19,20] nanostructures. Successful coassembly relies upon careful tuning of key enthalpic,[20,21] entropic,[22] and kinetic[23] considerations. While such techniques have been extensively studied with AB diblock and ABA triblock copolymers, there are only a few examples of ABC triblock terpolymers used as structure directing agents for inorganic materials.[24–26] None of these studies describes the formation of chiral and networked structures such as the alternating gyroid.

Here we report the synthesis of nanocomposites from the coassembly of poly(isoprene-b-styrene-b-ethylene oxide) with transition metal oxide nanoparticles resulting in the G^A morphology. Note that this approach is different from templating/backfilling approaches since coassembly provides direct access to inorganic nanocomposites without the need for multiple and tedious processing steps. For a series of nanocomposites with niobia nanoparticles we demonstrate that the chiral and networked nature of the resulting inorganic networks was most consistent with the G^A morphology by using in-depth x-ray and electron microscopy measurements. After discussing several potential pathways to transform these nanocomposites into func-

77

tional multicomponent nanoscale devices we demonstrate the first step of such approaches by creating mesoporous niobia of the same symmetry. The generalizability of this approach was evidenced by demonstrating mesoporous single gyroid strut networks of both amorphous titania and anatase titania.

5.3   Experimental Methods

5.3.1   Block Copolymer Synthesis and Characterization

The ISO triblock terpolymer utilized in this study was synthesized by anionic polymerization using established procedures.[22, 27] Briefly, the polymerization of isoprene and styrene were conducted sequentially in benzene at room termperature. The living chains were end capped with ethylene oxide and terminated. After purification, the alcohol terminated poly(isoprene-*b*-styrene) was reactivated in tetrahydrofuran using potassium napthalide and chain extended with ethylene oxide monomer, then terminated and further purified. The resulting ISO polymer was amphiphilic, having one hydrophilic O block and two hydrophobic blocks, I and S. The polyisoprene molecular weight was determined by gel permeation chromatography (GPC) using twelve poly(isoprene) standards for calibration and tetrahydrofuran as the eluent. The polydispersity of the final ISO polymer was determined by GPC. The molecular weight ratios of the styrene and ethylene oxide blocks were determined by nuclear magnetic resonance spectroscopy in deuterated chloroform. Quantitative spectra were collected using a Varian INOVA 400 MHz spectrometer with a 12 second delay between transients. The reported homopolymer densities[28] at 140 °C were used to calculate block volume fractions.

5.3.2 Nanocomposite Synthesis

The nanocomposites were synthesized in a one-pot fashion by casting a solution containing niobia nanoparticles and ISO1. The niobia nanoparticles were prepared in a chloroform solution containing 50-100 mg of polymer as previously reported in detail.[26] The hydrophilic oxide particles are expected to selectively swell the O block, thus increasing its effective volume fraction. The combined O + niobia volume fraction was controlled with the polymer to particle ratio. The volume contribution of the amorphous sol-gel derived niobia was approximated using a density of 2.0 g/cm^3. For comparison, a pure polymer film was prepared with the same casting procedure. The titania nanocomposite ISO1-T1 was synthesized using a 1.4 wt% solution of ISO1 in tetrahydrofuran. First, concentrated hydrochloric acid (37 wt%) was added to the polymer solution, followed by titanium isopropoxide. The molar ratios were 1:2.17:7.47 for Ti:HCl:H$_2$O for the sol-gel reagents. This solution was then stirred overnight and cast on a covered hot plate set to 50 °C. After the film was completely dry, it was aged at 100 °C for 3 days followed by 130 °C for 2 days to enhance the condensation reaction. A portion of the film was heated at 1 °C/min to 400 °C, held for 1 hr in air and cooled at 1 °C/min in order to convert the amorphous titania sol to anatase.

5.3.3 Equipment

Transmission Electron Microscopy (TEM)

Polymer and nanocomposite films were cut into ultrathin ∼50-70 nm sections at -55 °C with a Leica Ultracut UCT microtome. The slices were collected on a 40:60 solution of water and dimethylsulfoxide and then transferred onto 300 mesh copper grids. The sections were imaged using a Technai T12 operating at 120 kV.

The polyisoprene of some samples was stained with the sublimed vapor of pure OsO_4 for 1-24 hours at room temperature. The ISO polymer was subsequently removed from microtomed samples of ISO1-N3 and ISO1-T1 using a Fischione model 1020 Ar-O plasma cleaner for 10 minutes. The expected $\sim$1 nm/sec etch rate was sufficient to remove all of the ISO from the $\sim$70 nm thick sections.

A three-dimensional reconstruction of nanocomposite ISO1-N3 was generated using high angle annular dark field scanning transmission electron microscopy (HAADF-STEM). A tilt series was collected from -70 to 60° at 1° intervals and the images were aligned to a common tilt axis using a combination of cross-correlation and manual refinement. A simultaneous iterative reconstruction technique (SIRT) was used to reconstruct the niobia lattice. All tomographic data was processed using custom software described elsewhere.[29] A combination of blue isosurfaces with a blue translucent density profile was used to render the reconstructed niobia mesostructure.

Small-Angle X-ray Scattering (SAXS)

Two instruments were used to collect SAXS data. Most of the SAXS data were collected at the Cornell High Energy Synchrotron Source (CHESS) G1 station, with a setup consisting of a multilayer monochromator (λ=1.457 Å) with a 2D area detector and a sample-to-detector distance of 1.61 m and a photon flux of $\sim$5x10^{13} photons/sec/mm^2. Typical CHESS measurements were made using a beam size of 200 by 200 μm with an exposure of $\sim$1 second. The measurements for Figure 5.3 E were made using a 100 by 80 μm beam with 5 second exposures. When CHESS was unavailable an alternative system was used consisting of a Rigaku RU300 with a copper rotating anode (λ=1.54 Å) operated at 40 kV and 50 mA. The X-rays were monochromated using a Ni filter and focused using orthogonal

Franks mirrors. The SAXS patterns were collected with a homebuilt 1k x 1k pixel CCD detector similar to that described elsewhere.[30] Data are presented as 2D images as well as 1D plots of radially integrated intensity versus scattering vector q where q = $4\pi\sin(\theta)\lambda^{-1}$, where 2θ is the total scattering angle.

The simulated 2D SAXS pattern in Figure 5.3 B was calculated by combining the allowed diffraction peaks for all possible in-plane orientations of G^A grains with 1° increments. All grains were oriented with [110] zone axes aligned with the film normal which was 60° from the simulated scattering pattern.

5.3.4 Modelling

All models were produced using Matlab and a level set model[31] which was modified to have more constant strut thickness.[32] The unit cell models were rendered using isosurfaces of the level set model. The simulated TEM projections were created using the vol3d v2 package[33] to render voxels contained within the isosurfaces. All TEM simulations were calculated using a thickness of ~1 d^*_{100} which corresponds to ~50-60 nm. The niobia was rendered three times as dark as the OsO_4 stained I to be consistent with TEM observations.

5.4   Results and Discussion

5.4.1   Design of an ISO Polymer for Achieving G^A Nanocomposites

The triblock terpolymer ISO was selected for this study for multiple reasons. Firstly, ISO is one of the most studied triblock terpolymers providing a morphology map as determined by both experiments[34, 35] and simulations.[6] Secondly, the block sequence of ISO is in order of increasing hydrophilicity making it non-
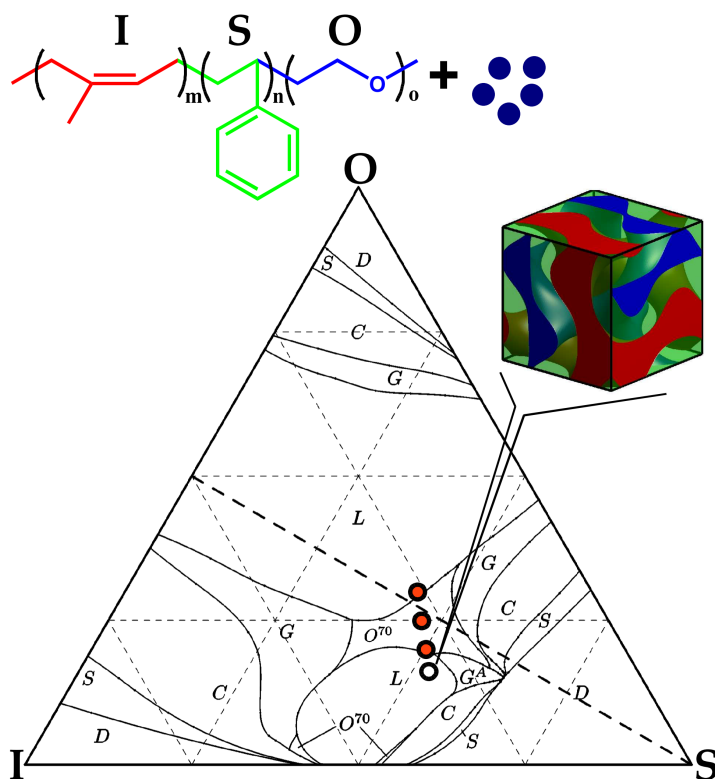
Figure 5.1: The compositions of ISO1 (white) and the resulting nanocomposites (orange) are shown above a morphology diagram calculated for pure ISO polymers.[6] The axes correspond to the volume fractions of I, S, and O. The oxide nanoparticles (blue circles) selectively incorporate into the O block of ISO. Thus the combined O + oxide volume fraction was used for the O axis of the nanocomposites. The shaded region corresponds to the volume fractions explored in this study.

frustrated[36] and preventing the formation of decorated phases with A-C interfaces.[3,37,38] Thirdly, ISO is amphiphilic, having two hydrophobic blocks, I and S, and one hydrophilic block, O, which may be used for the selective incorporation of hydrophilic nanoparticles. Lastly, ISO is quite similar to poly(isoprene-*b*-ethylene oxide) which has been studied extensively as a structure directing agent.[39] The polymer ISO1 was synthesized with the minimum O volume fraction necessary for the G^A morphology since the addition of oxide nanoparticles increases the combined O + oxide volume fraction. ISO1 was composed of 14.63, 29.04, and 9.77 kg/mol of I, S, and O, respectively, and had a polydispersity of 1.05. The volume fractions of ISO1 were 31.0 vol% I, 52.8 vol% S, and 16.2 vol% O (Figure 5.1). Furthermore, the 37:63 I:S isopleth which has a large O composition range for forming the G^A was targeted with the hope that this would also result in a large O + oxide composition range for G^A nanocomposites; please note that there is shift of the G^A region between experimental observations[35] and theory.

5.4.2   Morphology of Pure ISO1

The morphological behavior of the parent ISO structure directing agent was characterized by TEM and SAXS. A film of neat ISO1 was prepared using the same method detailed for the nanocomposites. Microtomed sections were stained with OsO_4 which selectively makes the I domain appear dark in bright field imaging whereas the unstained S and O domains remain light. TEM images of the stained film exhibited 4-fold and 3-fold symmetry projections (Figure 5.2 a and b) which were consistent with the simulated (100) and (111) planes of the I domain in the G^A. Quantitative analysis of these images provided a unit cell dimension $d^*_{100} \approx 41$-44 nm, (see Figure 5.1 d). An oriented circular 2D SAXS pattern was measured with the beam path along the film normal (Figure 5.2 c inset). The scattering
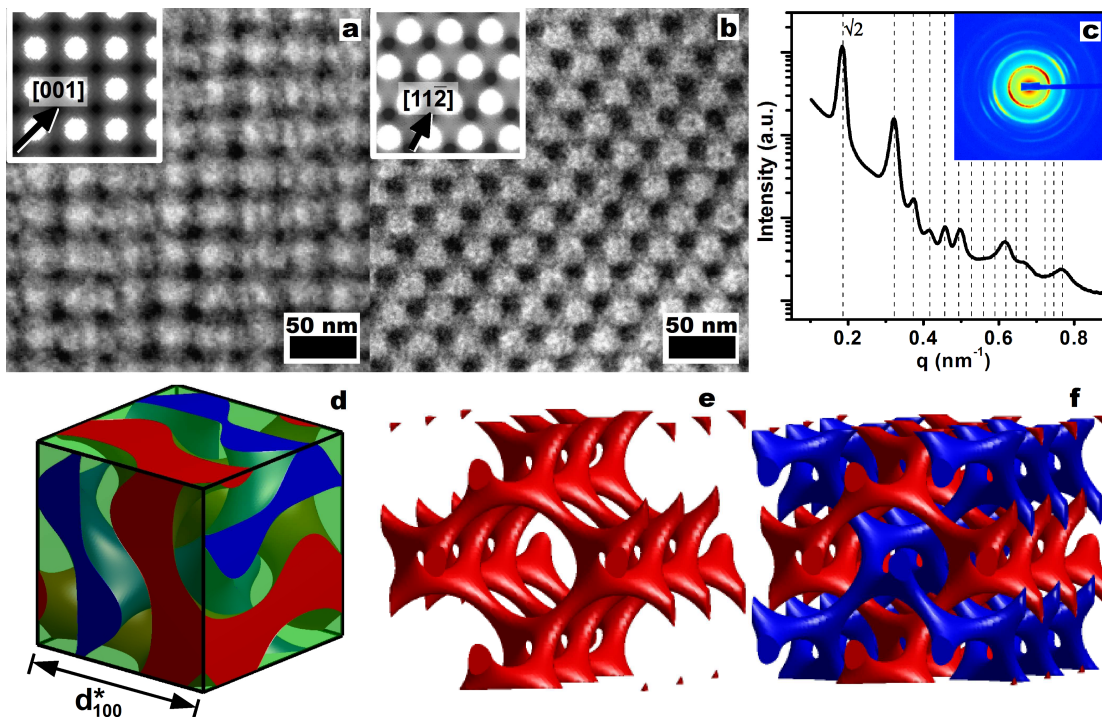
Figure 5.2: Bright field TEM images of neat ISO1 were consistent with the (100) (a) and (111) (b) planes of the alternating gyroid morphology (simulated TEM projections inset). Samples were stained with OsO_4 to enable contrast between the I strut (dark), S matrix (light), and O strut (light). The radially integrated 1D SAXS pattern (c) (2D pattern inset) was consistent with $I4_132$ symmetry and the allowed peaks were indicated with dashed lines. A model unit cell (d) was rendered depicting the I (red), S (green), and O (blue) domains using the measured volume fractions. The unit cell dimension d_{100}^* was indicated on the model unit cell. The chiral spirals down the <100> (e) and <111> directions are easiest to visualize with a low strut volume fraction. The I and O struts of this morphology have spirals with opposite chiralities and interweave through each other without contact (f).

pattern was radially integrated (Figure 5.2 c) and the expected peaks of the $I4_{1}32$ space group were indicated with dashed lines at $(q/q^{*})^{2}$=2, 6, 8, 10, 12, 14, 16, 18, 20, 22, 24, 26, 30, 32, 34. Occasionally a $(q/q^{*})^{2}$=4 peak was observed in some regions of the film which may have been due to film compression.[40] As expected from the known ISO morphology map[35] and the volume fractions of ISO1, the scattering pattern was consistent with the symmetry of the G^{A}. Furthermore, the G^{A} is the only one of the six known morphologies for ISO polymers[6,35] which was consistent with this SAXS data. The d_{100}^{*} spacing was calculated to be 47.8 nm from the q_{110} scattering vector which was close to the value obtained by TEM. The cast films of ISO1 formed remarkably well-ordered structures considering the equilibration challenges of network forming ABC triblock terpolymers[41] and that the film was prepared below the T_{g} of S. A model unit cell was rendered using the volume fraction of each component displayed with red, green, and blue for I, S, and O, respectively (Figure 5.2 d). The G^{A} contains small and large spirals along both the <100> and <111> family of directions. For a given direction, the smaller diameter helices share edges with larger diameter helices of opposite handedness (Figure 5.2 e). However, at realistic strut volume fractions the volume down the axes of the small diameter spirals is obstructed by the increased strut diameter, whereas the larger diameter spirals remain open (only these larger spirals will be discussed further). The spirals down the <100> and <111> directions have opposite handedness. This chirality is preserved throughout a grain. From the unit cell model, the diameter of the <100> spirals is slightly less than the pitch, p_{100}=d_{100}^{*}. Similarly, the diameter of the <111> spirals is slightly less than the pitch, $p_{111} = \sqrt{3} \cdot d_{100}^{*}/2$. The inversion of the I strut through the unit cell center produces another network with opposite spiral chiralities and is otherwise topologically identical to the O strut (Figure 5.2 f). All measurements on neat

ISO1 films were consistent with the G^A morphology.

5.4.3 2D SAXS Analysis of Nanocomposites

Nanocomposite materials were fabricated by the coassembly of niobia nanoparticles with ISO1. The three prepared niobia nanocomposites were named in order of increasing niobia content: ISO1-N1, ISO1-N2, and ISO1-N3 had oxide:polymer weight ratios of 0.103, 0.250, and 0.419, respectively. These ratios were calculated using the final mass of oxide assuming complete formation of Nb_2O_5. The combined O + oxide domain for these three nanocomposites was approximately 20, 25, and 30 vol%, respectively (Figure 5.1). The mesostructures of these nanocomposites were determined by a combination of SAXS and TEM characterizations. SAXS patterns were collected for all nanocomposites as a function of ϕ, the angle between the incident beam and the film normal. From this series of characterizations, sample ISO1-N1 had the largest number of well-resolved SAXS peaks. The best-defined pattern from ISO1-N1 at $\phi=60°$ was utilized first for identification of the structural symmetry. The 2D SAXS pattern was eccentric due to casting induced mesostructure compression along the film normal, vide infra. The scattering pattern was distortion corrected (Figure 5.3 a) so that the peaks could be indexed using a combination of manual fitting with algorithmic refinement.[40,42] It is usually difficult to determine the lattice symmetry of classic powder diffraction patterns consisting of a limited number of concentric rings. The inclusion of azimuthal information such as in Figure 5.3 a places strong constraints on the possible symmetry groups and unit cell lengths of the sample. The observed scattering peaks had cubic symmetry and the first three peak intensity ratios enabled the elimination of all cubic space groups except those within aspects 6, 8 and 9.[43] While we cannot eliminate space groups within aspects 6 and 8 based on SAXS
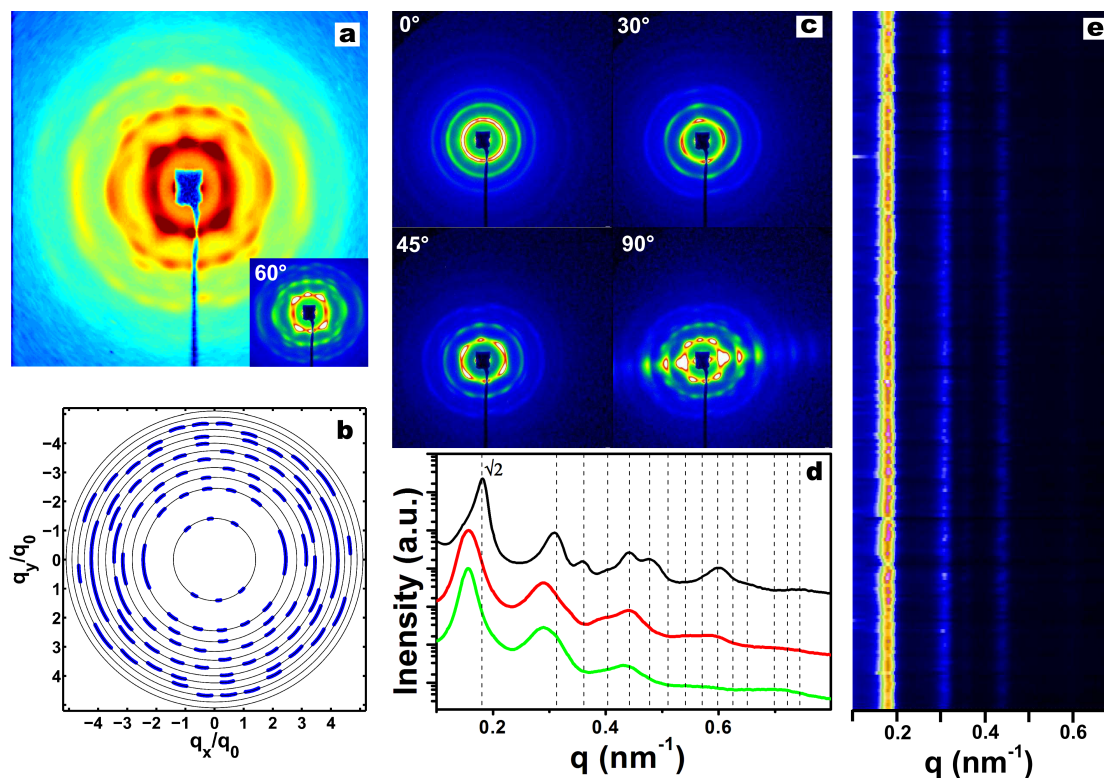
Figure 5.3: The SAXS pattern of sample ISO1-N1 had the most well-resolved peaks when the incident beam angle relative to the film normal was $\phi=60°$ (a inset). This eccentric pattern was distortion corrected to remove the effect of casting induced mesostructural compression (a). The $\sim$70 observed diffraction peaks and lobes were consistent with a homogeneous distribution of G^A grain orientations having a common [110] zone axis aligned with the film normal. Circles are drawn for all even integer values of $(q_x/q_0)^2$ with $q_0 = 0.147 \mathrm{nm}^{-1}$ from 2 to 26, inclusive. SAXS patterns of ISO1-N1 taken at different incident angles were consistent with lamellae aligned with the sample surface which were hypothesized to give rise to the observed [110] zone axis alignment with the film normal (c). The 2D SAXS patterns for all nanocomposites were radially integrated (d) and are shown in black, red, and green, respectively, for ISO1-N1, ISO1-N2, and ISO1-N3. The allowed peak positions for the $I4_132$ space group were indicated with dashed lines for sample ISO1-N1. A composite of 200 integrated SAXS scans evenly spaced along a 5 mm by 5 mm area of ISO1-N1 were displayed as a stack of horizontal lines with the color indicating the scattering intensity. The relatively uniform scattering profile of ISO1-N1 indicated that the mesostructure was macroscopically homogeneous (e). All color scales correspond to the log of the x-ray intensity.

alone, the combination of SAXS with TEM (vide infra) provides compelling evidence for the $I4_132$ space group of the G^A. The ~70 diffraction spots and lobes were consistent with a textured film of G^A gains having a homogeneous distribution of grain orientations with all of the [110] zone axis aligned with the film normal.[44]

Additional characteristics of ISO1-N1 were determined from this SAXS dataset. At $\phi=0°$ the resulting pattern exhibited a circular powder pattern indicating that there was no preferred azimuthal orientation of grains around the film normal (Figure 5.3 c). The scattering pattern monotonically became more elliptical as ϕ increased until the eccentricity was maximized at $\phi=90°$. Such evaporation induced unit cell compression along the film normal has been observed many times before and is characteristic of similar casting processes.[23, 26, 40, 42, 45, 46] The unit cell compression along the film normal was determined from the eccentricity to be between 16.7 and 18% for all of the nanocomposites. Such compression does not remove the chiral nor the network characteristics of the G^A morphology. An additional feature that was not observed at lower angles of ϕ was two peaks near q=0.159 nm^{-1} which were oriented along the film normal. The appearance of a (100) G^A peak could perhaps be caused by symmetry breaking due to film compression, however, the d-spacing of this feature was 3.1 nm smaller than the compressed G^A $d^*_{100}=42.6$ nm dimension. At $\phi=90°$ these additional peaks were most clearly resolved in addition to numerous higher ordered peaks corresponding to (q/0.159 nm^{-1})^2=1, 4, 9, 16, 25, and 36, consistent with a lamellar morphology parallel to the film surface. Considering the orientation of the lamellae, we suspect that lamellar layers were formed at the teflon-film interface during casting to lower the interaction free energy. A similar formation of lamellae at the substrate interface was observed before for thin films of ISO which also formed the G^A in bulk.[47] Furthermore, oriented lamellae were previously shown to transform into [110] oriented

G^A due to an epitaxial relationship (5% strain) between the lamellar d_1 spacing and the G^A d_{110} spacing.[44] In contrast, the lamellar d_1=39.5 nm spacing and the compressed G^A d_{110}=30.1 nm spacing in the same direction differed significantly by 27%. It may be possible that a less strained epitaxial relationship existed between these two morphologies during the dynamic coassembly process. However, a simpler interfacial energy argument that one of the A, B, or C dense (110) planes aligned on top of the terminal lamellae could also explain the observed film texture.

5.4.4   1D Integrated SAXS Analysis of Nanocomposites

The radially integrated SAXS patterns of all of the nanocomposites are shown in Figure 5.3 d. These patterns were all collected with ϕ=0°. The allowed peaks for the $I4_132$ space group were indicated with dashed lines for sample ISO1-N1. At high q the peaks become broad and symmetry identification more equivocal; however, the 2-dimensional patterns (Figure 5.3 a) give confidence to the space group assignment. Radially integrated diffraction patterns for ISO-N2 and N3 have too few resolved higher q peaks for a symmetry assignment. This peak broadening perhaps indicates that higher oxide concentrations lead to limited structural equilibration due to oxide cross-linking. However, the first order peak was well resolved and was used to determine the lattice constant, assuming the $I4_132$ space group; this assumption was supported by electron microscopy (see below). The d^*_{100} spacing calculated from the q_{110} peak positions shifted to larger spacings with increased oxide content. The d^*_{100} spacing increased from 49.5 to 57.4 nm in sample order which was consistent with the expected unit cell expansion with increased oxide volume fraction. Comparison of the d^*_{100} spacing from pure ISO to a sample with very low oxide loading, ISO1-N1, enabled the increase in segregation strength to be crudely estimated as $\chi_{\text{eff}} \approx 1.2\chi$ using the $d^*_{100} \propto \chi^{1/6}$ relationship.[48] Epps et

al. hypothesized that the increase in segregation strength is enhanced by having a glassy block (S) at the interface with the hydrophilic O block.[49] An increase in eff should also result in sharper intermaterial dividing surfaces. Two hundred 2D SAXS patterns were gathered at even spacings along a 5 mm by 5 mm piece of ISO1-N1. The relatively uniform 1D integrated data resulting from all of these scans (Figure 5.3 e) indicate that the ordered network mesostructure was uniform over macroscopic distances. The variations in the traces were consistent with large grains.

5.4.5 TEM Analysis of Nanocomposites

TEM images of microtomed sections of different nanocomposites are shown in Figure 5.4. The niobia present in the O + oxide domain (dark) enabled TEM imaging of the microtomed nanocomposites without any staining of the I (light) or S (light) domains. The low oxide fraction ($\sim$5 vol%) of ISO1-N1 was apparent in the sparse connectivity and narrow oxide channels of the shown (111) plane projection (Figure 5.4 a). We suspect that the niobia nanoparticles were preferentially distributed towards the center of the PEO domain to relax the chain stretching necessary to fill space.[40,50] Nanocomposites ISO1-N2 and ISO1-N3 had much higher oxide loadings ($\sim$10 and 16 vol%, respectively) and much clearer oxide connectivity when viewed by TEM. The oxide nanoparticles of ISO1-N3 occupy $\sim$55 vol% of the combined O + oxide domain showing that this approach works into the dense nanoparticle regime.[51] TEM projections consistent with several different G^A planes were observed for each sample. For the sake of brevity we detail only a few of the numerous TEM projections for sample ISO1-N3 (Figure 5.4 b-f). The four-fold (100) and three-fold (111) symmetric planes consistent with a cubic unit cell were viewed by TEM (Figure 5.4 b and c). The cross-section of the O + oxide helices were clearly
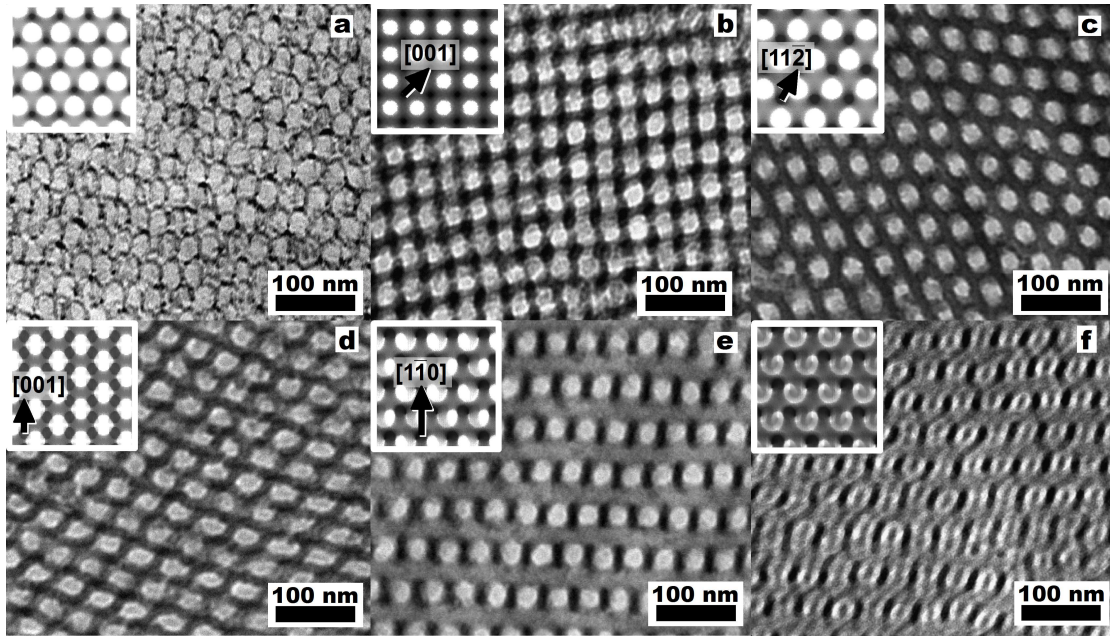
Figure 5.4: Bright field TEM was used to image the (111) plane of sample
ISO1-N1 (a) as well as the (100) (b), (111) (c), (110) (d), and
(113) (e) planes of sample ISO1-N3. The dark regions correspond
to the O + oxide struts and the light regions correspond to either
the I strut or S matrix. Selective I staining with OsO_4 enabled
simultaneous visualization of both the I strut (dark) and the O
+ oxide (darkest) strut within the S (light) matrix on the (113)
plane (f). TEM simulations are shown in insets.

observed in both of these projections, however the handedness of the spirals cannot be determined from individual projections. Additional oblique planes such as the (110) and (113) were also observed frequently by TEM (Figure 5.4 d and e) and were consistent with simulated TEM projections (insets). It should be pointed out that there are several different TEM projections that are very similar to the (113), including the (125), (123), and (431) for example. Due to microtoming induced distortion as well as room temperature flow of the low T_g I block, it is very difficult to distinguish between these projections with quantitative certainty. The nanocomposite texture of ISO1-N3 was investigated by microtoming slices parallel to the film surface. The dominant (110) and (113) projections observed in TEM of these oriented slices were consistent with the preferred [110] zone axis alignment with the film normal determined by SAXS. The I domain was subsequently stained selectively with OsO_4 to enable simultaneous visualization of both the O + oxide domain (darkest) and the I domain (dark) within the S matrix (light). The images of stained nanocomposite ISO1-N3 enabled visualization of both minority strut networks interweaving in the (113) plane (Figure 5.4 f, compare to Figure 5.4 e). Quantitative measurements from the unstained images of ISO1-N1, ISO1-N2, and ISO1-N3 were consistent with G^A morphologies having dimension $d^*_{100} \approx$ 30-43, 37-46, and 48-56 nm which were similar to the 49.5, 57.4, and 57.4 nm values determined by SAXS. The underestimation of lattice dimensions from TEM due to relaxation in thin sections is a well described and understood phenomena in I-containing polymer systems.[16]

5.4.6 Electron Tomography Analysis of Nanocomposites

Electron tomography was performed on nanocomposite ISO1-N3 to directly compare a single enantiomer with a model structure. The reconstructured niobia
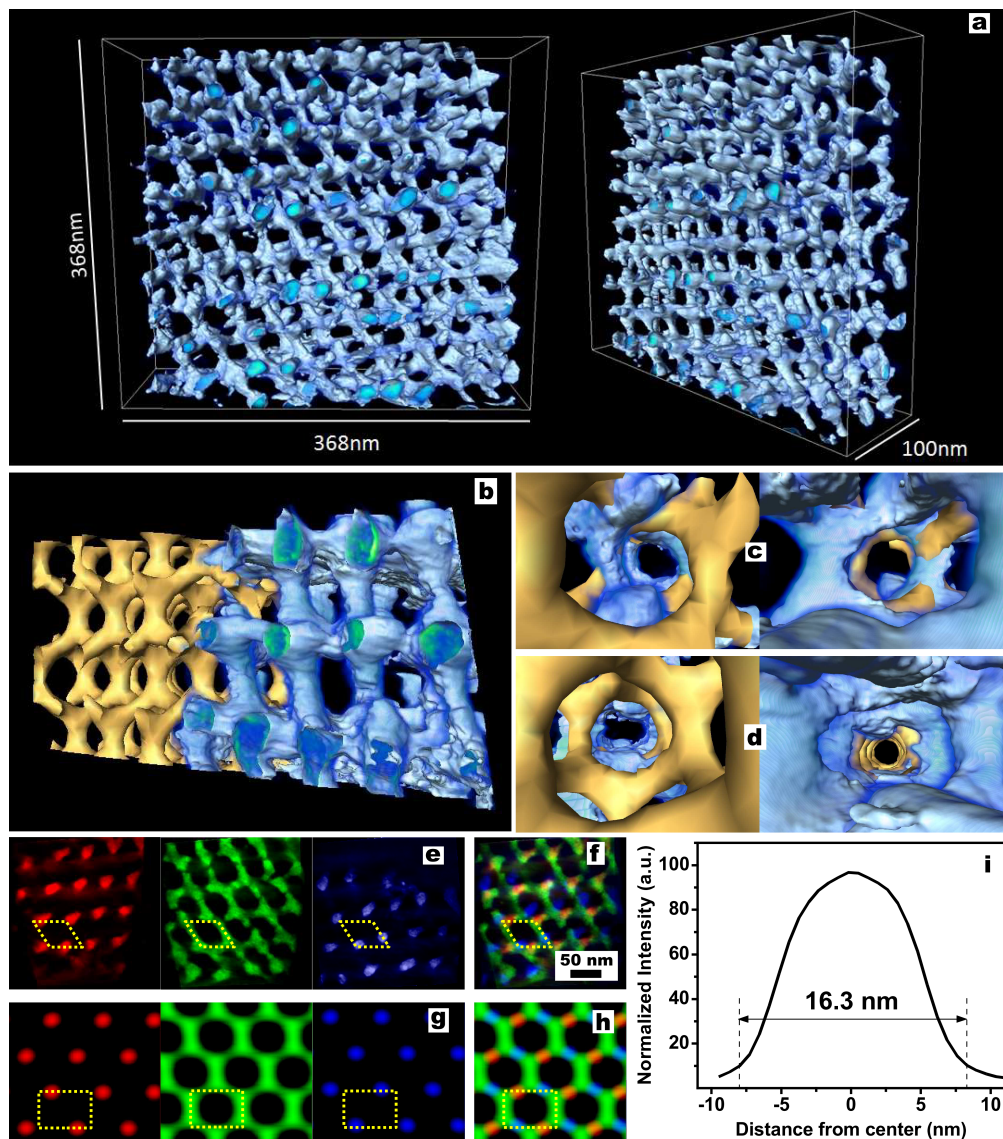
Figure 5.5: The 3D electron tomography reconstruction of nanocomposite ISO1-N3 (a, blue) was consistent with the level set model (gold) of the alternating gyroid (b). Views down the [100] axis exhibited left-handed spirals (c) where as views down the [111] axis exhibited right-handed spirals (d). Measured density distributions for (110) planes at increasing depth along a [110] direction (e) were distorted relative to simulated planes from the level set model (g), perhaps due to the sample preparation. The superposition of these measured planes (f) had similar symmetry (dotted box) to the superposition of the simulated planes (h). The average of fifteen density line profiles across different strut diameters showed that the niobia distribution was highest at the center of the struts (i) which lowered the chain stretching requirements for strut formation.

volume (Figure 5.5 a, blue) was clearly networked and was closely related to the level set model of a single gyroid strut (gold) of the G^A structure (Figure 5.5 b). The differences between the ideal model and the reconstructed volume were likely due to a convolution of casting-induced compression, microtome-induced shearing, and reconstruction-induced elongation (each occurring on different planes/axes). Spirals were directly observed down both the [100] (left-handed) and [111] (right-handed) directions (Figure 5.5 c,d). As expected for the G^A, these two directions contained helices of opposite chirality. Measurements on the reconstructed niobia volume were used to determine the pitch and diameter of the <100> niobia spirals to be ~51 and ~40 nm, respectively, as compared to the p_{100}=57.4 nm dimension expected from the SAXS data. Similarly, the pitch and diameter of the <111> spirals were determined to be ~36 and ~45 nm, respectively, which were similar to the anticipated p_{111}=49.4 nm calculated from the SAXS data. The consistency of this 3D structure with the level set model was further tested by analyzing a series of (110) planes at increasing depth along the [110] direction. The samples planar density distributions in this direction progressed from a rhombic array of circles, to a rhombic network, and then to a shifted rhombic array of circles (Figure 5.5 e). Simulations of these (110) planes based on the level set model undergo a similar series of patterns, although with rectangular symmetry (Figure 5.5 g). The measured planes thus were somewhat sheared relative to the simulated planes which could be due to distortions from both casting and/or microtoming. The superposition of the measured and simulated planes highlight the similar relative positions of the structural elements (Figure 5.5 f and h). In particular, the alternating color of circles along horizontal rows was quite similar to the simulation, albeit with some distortions. Additionally, the niobia nanoparticle distribution within the struts was determined from a slice of the reconstructed volume. Fifteen line

profiles across different strut diameters were normalized and averaged to yield the bell shaped density distribution of niobia nanoparticles (Figure 5.5 i). The niobia nanoparticles were most densely packed at the center of the struts and decreased in density towards the edge of the O+oxide domain. Such a nanoparticle distribution could significantly stabilize networked morphologies by limiting the chain stretching necessary to fill the volume of the struts.[40,50] While the location of nanoparticles within coassemblies containing block copolymers has been predicted before, it has never been directly measured using electron tomography.[52,53] Although a particular G^A enantiomer was observed, we expect these nanocomposites to have a racemic mixture of grains with equal proportions of each enantiomer.[54] However, the large >5 μm grains in these nanocomposites could enable physical isolation of an enantiomer.

5.4.7 Symmetry Determination and Stability of G^A Nanocomposites

The chiral and networked nanocomposites presented here are complex in nature. The convolution of the morphology with the mentioned distortions makes structural assignment a non-trivial task. However, the combination of 1D and 2D SAXS with TEM and STEM tomography provides a compelling case for assignment to the alternating gyroid morphology. In particular, the compositional window ($\sim$20-30 vol% O + oxide) for the G^A nanocomposites was larger than that for pure ISO (14-18 vol% O) along a similar I:S isopleth.[34] This enhanced network morphology composition window is likely due to the nanoparticles lowering the entropy loss for O-chain stretching to fill the O-strut volume. The large composition window for networked nanocomposites derived from ABC triblock terpolymers is a distinct advantage over AB diblock copolymer structure directing agents.[39]

5.4.8 Outlook for Applications

We envision several methods of future fabrication to produce functional networked nanocomposites from the materials described above. Realization of devices from these materials may require that the I and S domains be replaced with materials having different functionality while preserving the networked connectivity. Such a method of fabrication, where a sequence of three or more unique polymer blocks direct the spatial arrangement of multiple materials, thus defining the interfaces and pathways, was termed block sequence directed materials (BSDM).[55] Two iterations of selective etching followed with backfilling could produce such a device. There are numerous accounts of the selective removal of I from block copolymers.[56] The volume previously occupied by the I block could then be backfilled with a functional hard material. The remaining soft materials (primarily S) could then be selectively removed with a process such as plasma cleaning. The free volume would then again be backfilled with a functional material resulting in a nanoscale three-component networked device. The implications of such a fabrication technique could be significant provided that the grain boundaries are coherent and do not result in device failure due to short circuits. An alternative approach to avoid this potential issue is to use a non-selective etch to remove all of the polymer followed by sequential conformal depositions of functional materials. This non-selective method would enable construction of many component nanoscale networked devices and in principal could contain far more than three layers. The first step of this approach was demonstrated with TEM imaging of a mesoporous niobia single gyroid strut network which resulted from plasma etching the nanocomposite ISO1-N3. The increased oxide contrast and increased sensitivity of the sample to the incident electron beam were consistent with complete removal of the ISO polymer.
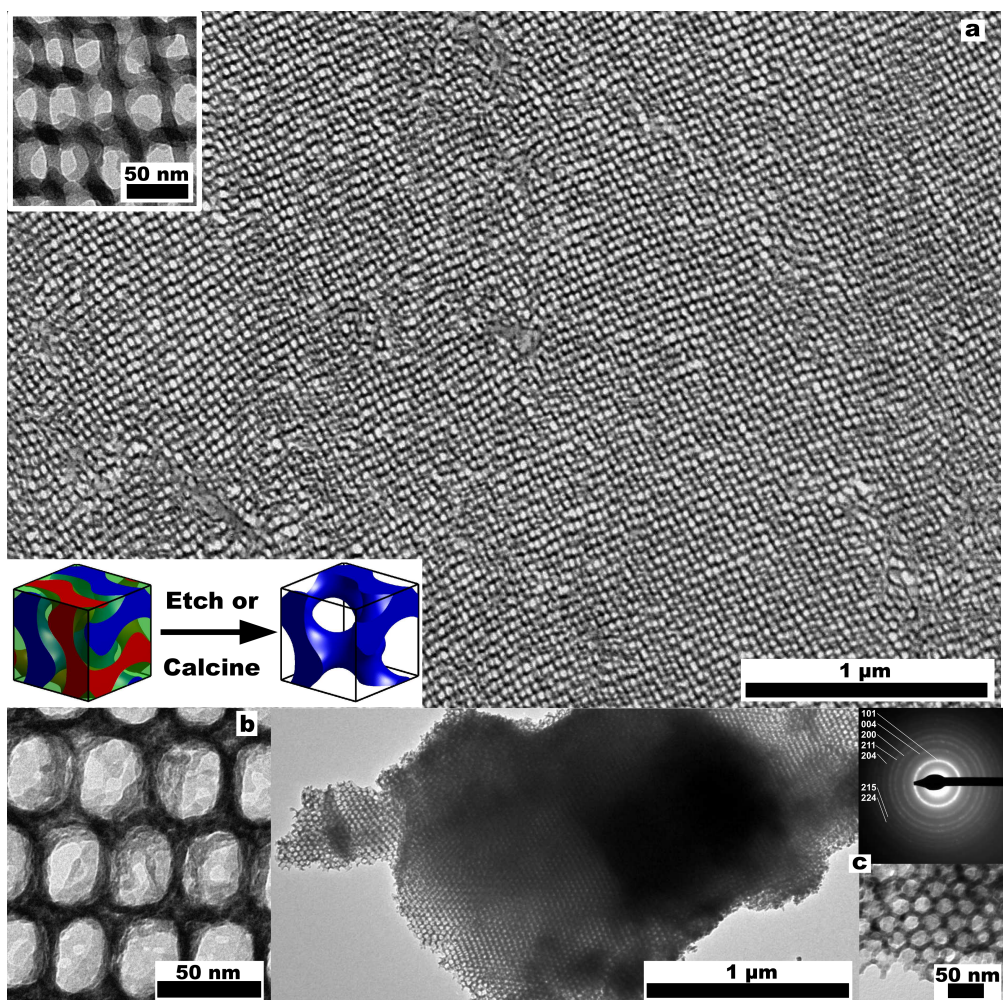
Figure 5.6: Bright field TEM images demonstrated that the ordered oxide single gyroid strut networks (dark) were preserved after removal of the ISO polymer from G^A nanocomposites to produce ordered mesopores (light). A close-up (a inset) and wide view (a, (100) plane) of sample ISO1-N3 after plasma removal of the ISO exhibit the large G^A grain with ordered mesopores. This approach was also demonstrated with titania from sample ISO1-T1. Plasma removal of ISO from ISO1-T1 yielded amorphous titania with ordered mesopores (b, (110) plane). Furthermore, crystalline anatase titania was demonstrated after high temperature calcination of ISO1-T1. A large view of the (111) plane of a mesoporous anatase single gyroid (c left) as well as a magnified section (c bottom right) show that the structure survived the heat treatment. Selected area electron diffraction on the calcined sample was consistent with anatase titania (c top right, PDF #21-1272).

Extension to Different Oxide Systems

This approach was shown to be generalizable by demonstrating two additional mesoporous single gyroid strut networks. The coassembly of amorphous titania nanoparticles with ISO1 using a 0.419 oxide:polymer weight ratio was found to result in a nanocomposite with the G^A morphology, named ISO1-T1 (detailed characterizations to follow in a separate publication). Plasma removal of the ISO polymer resulted in a mesoporous single gyroid strut composed of amorphous titania (Figure 5.6 b). Many applications utilizing transition metal oxides rely on the specific catalytic, optical, and electronic properties of the oxide in a crystalline state. To this end, the titania nanocomposite was subjected to a high temperature heat treatment which crystallized the titania and oxidatively removed the ISO polymer resulting in mesoporous single gyroid strut networks composed of anatase titania (Figure 5.6 c). Selected area electron diffraction patterns collected from these materials were consistent with the anatase (PDF No. 21-1272) crystal structure (Figure 5.6 c, upper right). The structure control for networks of different amorphous and crystalline transition metal oxides as obtained by a direct coassembly approach is encouraging (Figure 5.6).

Such mesoporous transition metal oxide networks could be useful directly or as a hard template. When used directly the network could enable orientation independent percolation for either transport or filtration properties (Figure 6.2 b). A key quality of the mesoporous single gyroid strut is the large $\sim$70 vol% of porosity which should enable easier backfilling or higher filtration fluxes. The mesoporous oxide strut could also be used directly for chiral metamaterials[57,58] or for photonic band gap applications requiring a complete photonic bandgap.[59,60] Furthermore, the mesopores could be infiltrated with another functional material that is perhaps not yet compatible with block copolymer structure directing.[61]

Such a process could result in two-component nanocomposites (Figure 6.2 d) or mesoporous inverse replicas after removal of the template (Figure 6.2 e).[62]

5.5   Acknowledgements

REFERENCES

[1] S. D. Oosterhout, M. M. Wienk, S. S. van Bavel, R. Thiedmann, L. J. A. Koster, J. Gilot, J. Loos, V. Schmidt, and R. A. J. Janssen. The effect of three-dimensional morphology on the efficiency of hybrid polymer solar cells. *Nature Materials*, 8(10):818–824, 2009.

[2] T. Goldacker, V. Abetz, R. Stadler, I. Erukhimovich, and L. Leibler. Non-centrosymmetric superlattices in block copolymer blends. *Nature*, 398(6723):137–139, 1999.

[3] F. S. Bates and G. H. Fredrickson. Block copolymers - designer soft materials. *Physics Today*, 52(2):32–38, 1999.

[4] T. P. Lodge. Block copolymers: Past successes and future challenges. *Macromolecular Chemistry and Physics*, 204(2):265–273, 2003.

[5] T. S. Bailey, C. M. Hardy, T. H. Epps, and F. S. Bates. A noncubic triply periodic network morphology in poly(isoprene-b-styrene-b-ethylene oxide) triblock copolymers. *Macromolecules*, 35(18):7007–7017, 2002.

[6] C. A. Tyler, J. Qin, F. S. Bates, and D. C. Morse. Scft study of nonfrustrated abc triblock copolymer melts. *Macromolecules*, 40(13):4654–4668, 2007.

[7] F. S. Bates, M. F. Schulz, A. K. Khandpur, S. Forster, and J. H. Rosedale. Fluctuations, conformational asymmetry and block copolymer phase behaviour. *Faraday Discussions*, 98:7–18, 1994.

[8] G. Floudas, B. Vazaiou, F. Schipper, R. Ulrich, U. Wiesner, H. Iatrou, and N. Hadjichristidis. Poly(ethylene oxide-b-isoprene) diblock copolymer phase diagram. *Macromolecules*, 34(9):2947–2957, 2001.

[9] Y. Matsushita, J. Suzuki, and M. Seki. Surfaces of tricontinuous structure formed by an abc triblock copolymer in bulk. *Physica B*, 248:238–242, 1998.

[10] J. Dupont, G. J. Liu, K. Niihara, R. Kimoto, and H. Jinnai. Self-assembled abc triblock copolymer double and triple helices. *Angewandte Chemie-International Edition*, 48(33):6144–6147, 2009.

[11] M. Thiel, M. S. Rill, G. v. Freymann, and M. Wegener. 3d bi-chiral photonic crystals: Three-dimensional bi-chiral photonic crystals. *Advanced Materials*, 21(46):NA, 2009.

[12] P. Dobriyal, H. Q. Xiang, M. Kazuyuki, J. T. Chen, H. Jinnai, and T. P. Russell. Cylindrically confined diblock copolymers. *Macromolecules*, 42(22):9082–9088, 2009.

[13] R. M. Ho, C. K. Chen, and Y. W. Chiang. Novel nanostructures from self-assembly of chiral block copolymers. *Macromolecular Rapid Communications*, 30(17):1439–1456, 2009.

[14] J. Wen and G. L. Wilkes. Organic/inorganic hybrid network materials by the sol-gel approach. *Chemistry of Materials*, 8(8):1667–1681, 1996.

[15] P. Innocenzi and B. Lebeau. Organic-inorganic hybrid materials for non-linear optics. *Journal of Materials Chemistry*, 15(35-36):3821–3831, 2005.

[16] M. Templin, A. Franck, A. DuChesne, H. Leist, Y. M. Zhang, R. Ulrich, V. Schadler, and U. Wiesner. Organically modified aluminosilicate mesostructures from block copolymer phases. *Science*, 278(5344):1795–1798, 1997.

[17] D. Y. Zhao, J. L. Feng, Q. S. Huo, N. Melosh, G. H. Fredrickson, B. F. Chmelka, and G. D. Stucky. Triblock copolymer syntheses of mesoporous silica with periodic 50 to 300 angstrom pores. *Science*, 279(5350):548–552, 1998.

[18] P. D. Yang, D. Y. Zhao, D. I. Margolese, B. F. Chmelka, and G. D. Stucky. Generalized syntheses of large-pore mesoporous metal oxides with semicrystalline frameworks. *Nature*, 396(6707):152–155, 1998.

[19] S. C. Warren, L. C. Messina, L. S. Slaughter, M. Kamperman, Q. Zhou, S. M. Gruner, F. J. DiSalvo, and U. Wiesner. Ordered mesoporous materials from metal nanoparticle-block copolymer self-assembly. *Science*, 320(5884):1748–1752, 2008.

[20] Z. H. Li, H. Sai, S. C. Warren, M. Kamperman, H. Arora, S. M. Gruner, and U. Wiesner. Metal nanoparticle-block copolymer composite assembly and disassembly. *Chemistry of Materials*, 21(23):5578–5584, 2009.

[21] G. Soler-Illia and C. Sanchez. Interactions between poly(ethylene oxide)-based surfactants and transition metal alkoxides: Their role in the templated construction of mesostructured hybrid organic-inorganic composites. *New Journal of Chemistry*, 24(7):493–499, 2000.

[22] S. C. Warren, F. J. Disalvo, and U. Wiesner. Nanoparticle-tuned assembly and disassembly of mesostructured silica hybrids (vol 6, pg 156, 2007). *Nature Materials*, 6(3):248–248, 2007.

[23] E. L. Crepaldi, Gjda Soler-Illia, D. Grosso, F. Cagnol, F. Ribot, and C. Sanchez. Controlled formation of highly organized mesoporous titania thin films: From mesostructured hybrids to mesoporous nanoanatase tio2. *Journal of the American Chemical Society*, 125(32):9770–9786, 2003.

[24] G. E. S. Toombes, S. Mahajan, M. Thomas, P. Du, M. W. Tate, S. M. Gruner, and U. Wiesner. Hexagonally patterned lamellar morphology in abc triblock copolymer/aluminosilicate nanocomposites. *Chemistry of Materials*, 20(10):3278–3287, 2008.

[25] G. E. S. Toombes, S. Mahajan, M. Weyland, A. Jain, P. Du, M. Kamperman, S. M. Gruner, D. A. Muller, and U. Wiesner. Self-assembly of four-layer woodpile structure from zigzag abc copolymer/aluminosilicate concertinas. *Macromolecules*, 41(3):852–859, 2008.

[26] M. Stefik, S. Mahajan, H. Sai, T. H. Epps, F. S. Bates, S. M. Gruner, F. J. DiSalvo, and U. Wiesner. Ordered three- and five-ply nanocomposites from abc block terpolymer microphase separation with niobia and aluminosilicate sols. *Chemistry of Materials*, 21(22):5466–5473, 2009.

[27] J. Allgaier, A. Poppe, L. Willner, and D. Richter. Synthesis and characterization of poly[1,4-isoprene-b-(ethylene oxide)] and poly[ethylene-co-propylene-b-(ethylene oxide)] block copolymers. *Macromolecules*, 30(6):1582–1586, 1997.

[28] L. J. Fetters, D. J. Lohse, D. Richter, T. A. Witten, and A. Zirkel. Connection between polymer molecular-weight, density, chain dimensions, and melt viscoelastoc properties. *Macromolecules*, 27(17):4639–4647, 1994.

[29] P. A. Midgley and M. Weyland. 3d electron microscopy in the physical sciences: The development of z-contrast and eftem tomography. *Ultramicroscopy*, 96(3-4):413–431, 2003.

[30] M. W. Tate, E. F. Eikenberry, S. L. Barna, M. E. Wall, J. L. Lowrance, and S. M. Gruner. A large-format high-resolution area x-ray-detector based on a fiberoptically bonded charge-coupled-device (ccd). *Journal of Applied Crystallography*, 28:196–205, 1995.

[31] M. Wohlgemuth, N. Yufa, J. Hoffman, and E. L. Thomas. Triply periodic bicontinuous cubic microdomain morphologies by symmetries. *Macromolecules*, 34(17):6083–6089, 2001.

[32] J. Hoffman. Skeletal graphis approximated by level surfaces, August 2005.

[33] Joe Conti and Oliver Woodford. Vol3d v2, 2009.

[34] T. H. Epps, E. W. Cochran, T. S. Bailey, R. S. Waletzko, C. M. Hardy, and F. S. Bates. Ordered network phases in linear poly(isoprene-b-styrene-b-ethylene oxide) triblock copolymers. *Macromolecules*, 37(22):8325–8341, 2004.

[35] J. Chatterjee, S. Jain, and F. S. Bates. Comprehensive phase behavior of poly(isoprene-b-styrene-b-ethylene oxide) triblock copolymers. *Macromolecules*, 40(8):2882–2896, 2007.

[36] T. S. Bailey. *Morphological behavior spanning the symmetric ab and abc block copolymer states*. PhD thesis, University of Minnesota, 2001.

[37] T. S. Bailey, H. D. Pham, and F. S. Bates. Morphological behavior bridging the symmetric ab and abc states in the poly(styrene-b-isoprene-b-ethylene oxide) triblock copolymer system. *Macromolecules*, 34(20):6994–7008, 2001.

[38] F. S. Bates. Network phases in block copolymer melts. *Mrs Bulletin*, 30(7):525–532, 2005.

[39] B. C. Garcia, M. Kamperman, R. Ulrich, A. Jain, S. M. Gruner, and U. Wiesner. Morphology diagram of a diblock copolymer-aluminosilicate nanoparticle system. *Chemistry of Materials*, 21(22):5397–5405, 2009.

[40] G. E. S. Toombes, A. C. Finnefrock, M. W. Tate, R. Ulrich, U. Wiesner, and S. M. Gruner. A re-evaluation of the morphology of a bicontinuous block copolymer-ceramic material. *Macromolecules*, 40(25):8974–8982, 2007.

[41] T. H. Epps and F. S. Bates. Effect of molecular weight on network formation in linear abc triblock copolymers. *Macromolecules*, 39(7):2676–2682, 2006.

[42] A. C. Finnefrock, R. Ulrich, G. E. S. Toombes, S. M. Gruner, and U. Wiesner. The plumber's nightmare: A new morphology in block copolymer-ceramic nanocomposites and mesoporous aluminosilicates. *Journal of the American Chemical Society*, 125(43):13084–13093, 2003.

[43] T. Hahn. *International tables for crystallography*, volume A Space-Group Symmetry. Kluwer Academic Publishers, Boston, 2002.

[44] J. Suzuki, K. Nakane, A. Takano, and Y. Matsushita. Self-assembly template during morphological transition of a linear abc triblock copolymer from lamellar to gyroid structure. *Polymer*, 45(26):8989–8997, 2004.

[45] M. Klotz, P. A. Albouy, A. Ayral, C. Menager, D. Grosso, A. Van der Lee, V. Cabuil, F. Babonneau, and C. Guizard. The true structure of hexagonal mesophase-templated silica films as revealed by x-ray scattering: Effects of thermal treatments and of nanoparticle seeding. *Chemistry of Materials*, 12(6):1721–1728, 2000.

[46] J. Schuster, R. Kohn, A. Keilbach, M. Doblinger, H. Amenitsch, and T. Bein. Two-dimensional-hexagonal periodic mesoporous polymer resin thin films by soft templating. *Chemistry of Materials*, 21(24):5754–5762, 2009.

[47] T. H. Epps, D. M. DeLongchamp, M. J. Fasolka, D. A. Fischer, and E. L. Jablonski. Substrate surface energy dependent morphology and dewetting in an abc triblock copolymer film. *Langmuir*, 23(6):3355–3362, 2007.

[48] A. N. Semenov. Microphase separation in diblock-copolymer melts: Ordering of micelles. *Macromolecules*, 22(6):2849–2851, 2002.

[49] T. H. Epps, T. S. Bailey, R. Waletzko, and F. S. Bates. Phase behavior and block sequence effects in lithium perchlorate-doped poly(isoprene-b-styrene-b-ethylene oxide) and poly(styrene-b-isoprene-b-ethylene oxide) triblock copolymers. *Macromolecules*, 36(8):2873–2881, 2003.

[50] M. Kamperman, M. A. Fierke, C. B. W. Garcia, and U. Wiesner. Morphology control in block copolymer/polymer derived ceramic precursor nanocomposites. *Macromolecules*, 41(22):8745–8752, 2008.

[51] A. Jain and U. Wiesner. Silica-type mesostructures from block copolymer phases: Formation mechanism and generalization to the dense nanoparticle regime. *Macromolecules*, 37(15):5665–5670, 2004.

[52] R. B. Thompson, V. V. Ginzburg, M. W. Matsen, and A. C. Balazs. Predicting the mesophases of copolymer-nanoparticle composites. *Science*, 292(5526):2469–2472, 2001.

[53] R. Mezzenga and J. Ruokolainen. Nanocomposites: Nanoparticles in the right place. *Nat Mater*, 8(12):926–928, 2009.

[54] J. Chin and P. V. Coveney. Chirality and domain growth in the gyroid mesophase. *Proceedings of the Royal Society a-Mathematical Physical and Engineering Sciences*, 462(2076):3575–3600, 2006.

[55] M. Stefik, H. Sai, K. Sauer, S. M. Gruner, F. J. DiSalvo, and U. Wiesner. Three-component porous-carbon-titania nanocomposites through self-assembly of abcba block terpolymers with titania sols. *Macromolecules*, 42(17):6682–6687, 2009.

[56] D. A. Olson, L. Chen, and M. A. Hillmyer. Templating nanoporous polymers with ordered block copolymers. *Chemistry of Materials*, 20(3):869–890, 2008.

[57] D. R. Smith, Willie J. Padilla, D. C. Vier, S. C. Nemat-Nasser, and S. Schultz. Composite medium with simultaneously negative permeability and permittivity. *Physical Review Letters*, 84(18):4184, 2000.

[58] J. B. Pendry. A chiral route to negative refraction. *Science*, 306(5700):1353–1355, 2004.

[59] V. Babin, P. Garstecki, and R. Holyst. Photonic properties of multicontinuous cubic phases. *Physical Review B*, 66(23), 2002.

[60] M. Maldovan, A. M. Urbas, N. Yufa, W. C. Carter, and E. L. Thomas. Photonic properties of bicontinuous cubic microphases. *Physical Review B*, 65(16), 2002.

[61] S. Lepoutre, B. Julian-Lopez, C. Sanchez, H. Amenitsch, M. Linden, and D. Grosso. Nanocasted mesoporous nanocrystalline zno thin films. *Journal of Materials Chemistry*, 20(3):537–542.

[62] M. Tiemann. Repeated templating. *Chemistry of Materials*, 20(3):961–971, 2008.

CHAPTER 6

OUTLOOK

The previous chapters detailed progress towards the realization of block sequence directed materials (BSDM). It was demonstrated through several examples that the careful tuning of coassembly processes can lead to robust control over both the composition and morphology of multicomponent nanocomposites. While the demonstrations thus far are quite promising, there are still several challenges remaining to create the first operational devices based on BSDMs (Figure 6.1). Realization of ordered BSDM devices would require that either all polymer blocks lead directly to functional materials, or alternatively that non-functional polymer blocks are subsequently replaced by functional materials while preserving the morphology. The future of the former option is dubious as most polymer blocks with interesting e.g. electronic properties are either semi-crystalline or have a high T_g and thus tend to form poorly ordered morphologies.[1] The latter option seems more feasible since the required steps have been demonstrated before for simpler binary systems.

I can envision several methods of fabrication to produce functional nanocomposites from the ISO-oxide nanocomposites described in Chapters 4 and 5. The challenge to building devices out of these nanocomposites is to replace the I and S domains with different functional materials. One route to accomplish this could utilize two iterations of selective etching followed with backfilling (Figure 6.2 a). There are numerous accounts of the selective removal of I from block copolymers.[2] The volume previously occupied by the I block could then be backfilled with a functional material by utilizing methods developed in the nanoscale hard-templating community. The remaining soft materials (primarily S) could then be selectively removed with a process such as plasma cleaning. The free volume would then again
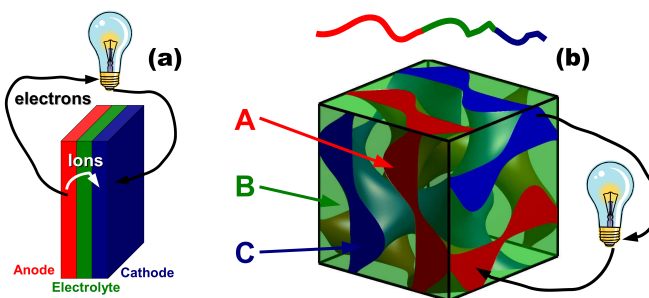
Figure 6.1: The pathways and interfaces for e.g. electrochemical devices (a) could result directly from morphology of a block copolymer (b). The ultimate goal is to have a sequence of three or more chemically unique polymer blocks direct both the spatial arrangement and interface definitions of multiple functional materials.
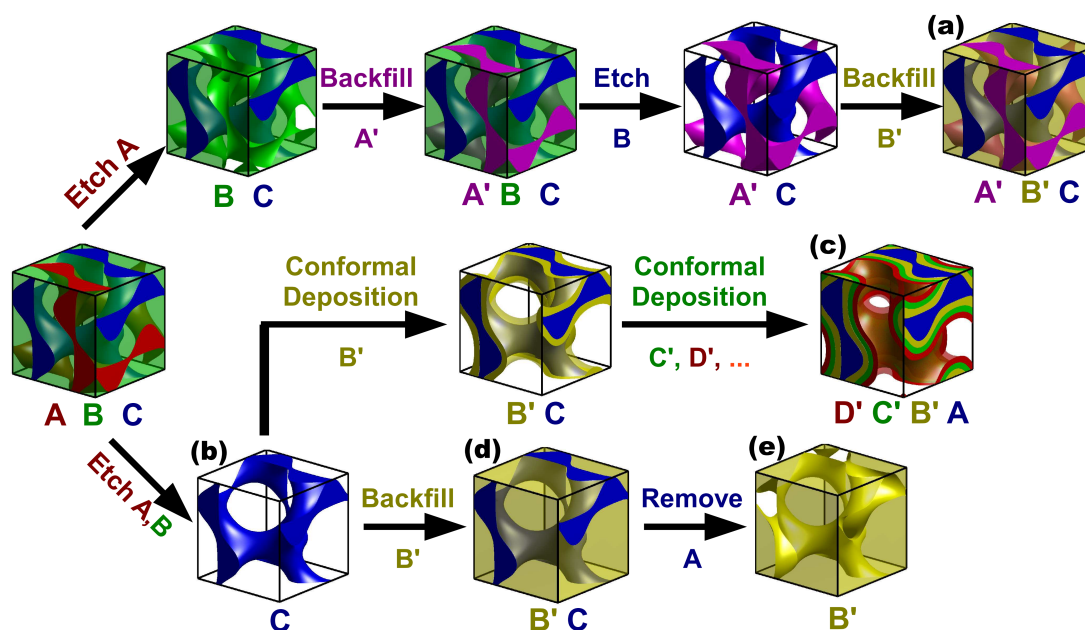

Figure 6.2: There are two potential routes to convert the ISO-oxide nanocomposites into nanoscale networked devices by a series of either selective processes (a) or non-selective processes (c). Furthermore, mesoporous single gyroid oxides could be fabricated (b) for optical devices, devices requiring orientation independent percolation, or for the hard templating of binary nanocomposites (d) or for inverse replicas (e). All strategies proposed here would result in chiral and networked materials.

be backfilled with a functional material resulting in a nanoscale three-component networked device. The implications of such a fabrication technique could be significant provided that the grain boundaries are coherent and do not result in device failure due to short circuits i.e. A-C type contacts between grains. An alternative approach to avoid this potential issue is to use a non-selective etch to remove all of the polymer (Figure 6.2 b) followed by sequential conformal depositions of functional materials (Figure 6.2 c). Thus the electronic integrity of the device would rely upon the quality of the conformal deposition technique rather than on the soft dynamics of macromolecules. Successful conformal deposition could be achieved in such nanostructured cavities with procedures such as atomic layer depostion,[3] electrodeposition,[4] or chemical vapor deposition.[5] This non-selective method would enable construction of many component nanoscale networked devices and in principal could contain far more than three layers. With so many compositional and morphological options becoming available with future developments of BSDMs the future is certainly bright for both evolutionary improvement and revolutionary innovation in nanotechnologies such as advanced energy conversion and storage devices.

REFERENCES

[1] S. D. Oosterhout, M. M. Wienk, S. S. van Bavel, R. Thiedmann, L. J. A. Koster, J. Gilot, J. Loos, V. Schmidt, and R. A. J. Janssen. The effect of three-dimensional morphology on the efficiency of hybrid polymer solar cells. *Nature Materials*, 8(10):818–824, 2009.

[2] D. A. Olson, L. Chen, and M. A. Hillmyer. Templating nanoporous polymers with ordered block copolymers. *Chemistry of Materials*, 20(3):869–890, 2008.

[3] S. M. George. Atomic layer deposition, an overview. *Chemical Review*, 110(1):111–131, 2010.

[4] J. W. Long, B. Dunn, D. R. Rolison, and H. S. White. Three-dimensional battery architectures. *Chemical Reviews*, 104(10):4463–4492, 2004.

[5] S. H. Baxamusa, S. G. Im, and K. K. Gleason. Initiated and oxidative chemical vapor deposition: a scalable method for conformal and functional polymer films on real substrates. *PHYSICAL CHEMISTRY CHEMICAL PHYSICS*, 11(26):5227–5240, 2009.